MASS TRANSFER ASPECTS OF A.C. ELECTROSLAG REMELTING

by

MICHAEL E. FRASER

B.Sc. McMaster University, 1968

M.Sc. McMaster University, 1970

A THESIS SUBMITTED IN PARTIAL FULFILMENT OF

THE REQUIREMENTS FOR THE DEGREE OF

DOCTOR OF PHILOSOPHY

in the Department

of

METALLURGY

We accept this thesis as conforming to the

required standards

THE UNIVERSITY OF BRITISH COLUMBIA

January, 1974

In presenting this thesis in partial fulfilment of the requirements for an advanced degree at the University of British Columbia, I agree that the Library shall make it freely available for reference and study. I further agree that permission for extensive copying of this thesis for scholarly purposes may be granted by the Head of my Department or by his representatives. It is understood that copying or publication of this thesis for financial gain shall not be allowed without my written permission.

Department of Metallurgy.

The University of British Columbia
Vancouver 8, Canada

Date Jan 30 / 74

ABSTRACT

Previous attempts at a quantitative description of alloy losses in electroslag remelting (ESR) operations have not adequately reflected the true nature of this process. In the current work a mass transfer model was developed which takes into account four reaction sites and mass transfer of all species at each site.

An experimental program was subsequently devised to test extensively the provisions of the model. The overall system was simplified by avoiding complex alloys and multicomponent slags and also by excluding air. Care was taken to deal only with species whose thermochemistry was known in both slag and metal phases. The electrode material used was mild steel in which manganese was the only oxidizable species. Slags used throughout the melt program were CaF_2 - 20% CaO, for which system the activity data for FeO, MnO were available.

The melt program provided data on Mn losses in a variety of ESR operating conditions including steady and unsteady state, live and insulated mold configurations. The effects of melting in air and of direct current operation were also investigated. Several melts undertaken with Armco iron were designed to permit direct calculation of certain mass transfer coefficients.

The mass transfer model was applied to each melt and the predictions compared to the experimental data. There was generally good agreement between the two, confirming that the manganese losses were controlled entirely by mass transfer effects. Further study of the model

showed mass transfer of species in the slag phase to be the predominant rate controlling step. The relative roles of the various reaction sites in contributing to the overall mass transfer were also elaborated by this analysis.

In order to assess the full potential of this mass transfer approach, the model was extended to the manganese, sulphur reaction system and to larger, commercial-sized ESR furnaces. Projections of alloy losses based on this scale-up study appeared to be consistent with the sparse information that is currently available.

TABLE OF CONTENTS

Chapter Page

Chapter Page

Chapter Page

Page

LIST OF TABLES

Table | Page

LIST OF FIGURES

Figure | Page

ACKNOWLEDGEMENTS

The author would like to express his gratitude to Dr. A. Mitchell for his help and guidance throughout the course of this work. Much appreciation is also given for the many helpful discussions with fellow graduate students and other faculty members. The author would also like to thank Dr. J.K. Brimacombe for his helpful criticism of the draft manuscript.

The assistance of Mr. A. Thomas in designing and constructing the experimental apparatus is gratefully acknowledged. Special thanks are due also to Mr. R. Palylyk for drawing the figures in the thesis.

The author would like to thank his wife, Deborah, for her constant encouragement over the duration of this work.

The financial assistance of the American Iron and Steel Institute (Grant #190) and of the National Research Council are gratefully acknowledged.

CHAPTER 1

INTRODUCTION

1.1 Introduction

The analysis of rate phenomena in process metallurgy has received increasing attention over the past decade. This interest has evolved chiefly as a result of the demands for increased automation to reduce costs and for increased process efficiency. In turn the necessity of developing the appropriate equipment and controls has placed more emphasis on a precise understanding of the detailed transport processes occurring in metallurgical processes. The application of mathematical modelling techniques is now common in ferrous and nonferrous operations alike, from blast furnace to soaking pit; from roaster to refinery.

1.2 Nature of the Problem

The increasingly widespread use of the electroslag remelting process for the production of high quality alloys, especially forging alloys, has resulted in numerous investigations into the nature of this process. These studies may be classified as follows: (1) the heat flow problem; (2) the chemical refining problem.

To date the preponderance of work has been concerned with the mathematical and experimental analysis of heat flows for the purpose of controlling the structural properties of ESR forging ingots.[2,24,56,86,87]

These research programs have played an important role in the design and construction of larger and larger ESR facilities (>100 tons). However, it has only recently been recognized that substantial degrees of refining involving essential alloying elements may also occur.

On comparing ESR to its major competitor, vacuum arc remelting (VAR), an enhanced potential for chemical refining and composition control in ESR becomes evident. In VAR, the environment, consisting of water cooled copper mold and vacuum, is inert to the metal being remelted. Any refining effect is consequently limited to pressure sensitive reactions and the floating out of inclusions. The situation in ESR is very different. From the schematic diagram of a typical ESR unit (Figure 1) one observes a number of reaction sites involving solid/gas, solid/liquid, liquid/liquid and gas/liquid interfaces. This probability of chemical interaction suggests the desirability of investigation into the possible contributing factors.

That specialty steel makers should be concerned with losses of highly oxidizable alloying elements is not surprising. In some alloys, where only small concentrations of essential alloying elements are present, there may be a critical sensitivity to composition fluctuations. For instance, a maraging steel containing 0.8% titanium is reported to suffer a decrease in yield strength of 10^4 psi on losing 0.1% titanium.[1] Many examples of this type, involving losses of titanium, aluminium, molybdenum, silicon, etc., have been reported in the literature.[2,3,4,5]

Attempts have been made to correct or compensate for such losses by say, using an inert gas cover[3] or descaling the electrode. Others have suggested the use of "balanced" slags[6] with additions of the

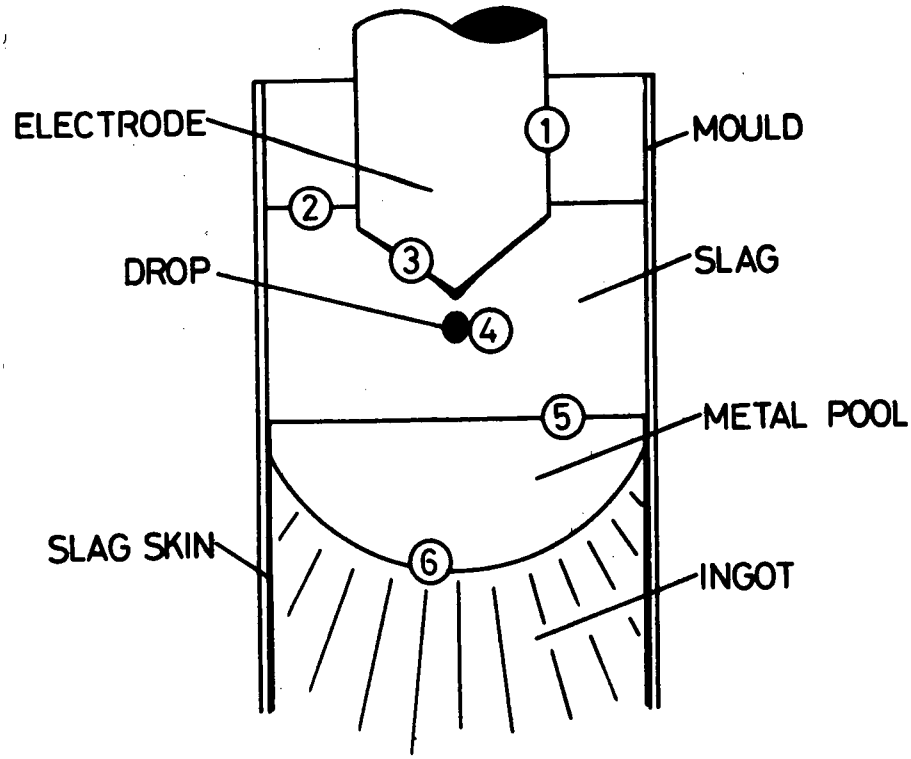

① ELECTRODE/ATMOSPHERE
② SLAG/ATMOSPHERE
③ ELECTRODE TIP/SLAG
④ DROPLET/SLAG
⑤ METAL POOL/SLAG
⑥ METAL POOL/INGOT

Fig. 1—ESR reaction sites.

oxides of the reactive elements. In such a system TiO_2 and Al_2O_3 would be added to slags used for remelting alloys containing Ti and Al. However, there is some doubt as to whether this approach of shifting the chemical equilibrium is really effective. The main cause of oxidation is not the low activity of the oxidizable species in the slag but rather the relatively high oxidation potential of the slag.

It appears, from previous industrial and experimental evidence, that losses of these important, but reactive alloying elements cannot be completely prevented. As a result, if the production of commercially acceptable ingots is to be ensured, ESR producers must be able to anticipate these losses and compensate the electrode feed stock accordingly. At the present time, the corrections are made on a strictly empirical basis by observation of previous melts. This procedure is necessary, due to the impracticality of sampling and analysis of the remelted metal during the process operation. Such a trial and error approach becomes prohibitively expensive for commercial ESR operations producing ingots of high alloy steel in the 60-150 ton range.

It is imperative, therefore, that alternate methods of predicting alloy losses be developed. One approach, which has much potential in this regard, is the mathematical modelling of the composition change. Several attempts have been made to formulate such a model, but these have met with little success. The reasons for this lack of success and the possibilities for improvement are discussed below.

1.3 Previous Work

Many instances of composition changes in ESR processed material have been reported in the literature. References (1) through (22) are representative of these. Attempts to explain the alloy element losses quantitatively are found much less frequently, however. These studies may be classified as follows:

1. Equilibrium models.
2. Single stage reactor models.
3. Descriptive Mass Transfer analysis.

1.3.1 Equilibrium Models

Hoyle[7] has treated the ESR process as a closed system following an equilibrium relationship between the slag and metal such that each element of molten metal was assumed to attain complete equilibrium with the slag. With this approach, he predicted, for example, that the rate of sulphur exchange decreased progressively during the melt. This treatment led to a relationship in which the sulphur content of the metal depended exponentially on time.

$$\ln\left(1 - \frac{[X]}{[X]_0}\right) = -\frac{W_m}{W_s}\,\frac{1}{K} = -\text{const} \times W_m \quad . \qquad (1.1)$$

These calculations were compared to experimental results on steels containing sulphur. However, at the time this work was done (1962-1966) insufficient data were available on thermodynamic activities

in CaF_2-based slags to assess properly the value of K, the reaction equilibrium constant. This fact, in addition to poor experimental precision, prevented an exact comparison of the model and the experimental results.

Hawkins, Davis and co-workers[17,28,29] presented much the same model. In this same paper,[17] however, a fairly comprehensive study of activities and phase equilibria in CaF_2-based slags was given. These data allowed a more precise statement of the equilibrium model but nevertheless agreement with published data was not good showing only that the model predicted the correct desulphurization trend (Figure 2). It is interesting to note Hawkins' suggestion that kinetic effects may be of some importance in the ESR process.

Subsequently, Hawkins et al.[22] introduced the concept of a fictitious "equilibrium" temperature. Calculation of this value was accomplished via the relationship

$$\Delta G = \Delta G^\circ + RT\ln K \qquad (1.2)$$

by substituting the appropriate activity coefficients and experimentally determined concentrations for

$$K = \frac{\Pi\alpha_{PRODUCTS}}{\Pi\alpha_{REACTANTS}} . \qquad (1.3)$$

Thus each reaction occurring in a system will not necessarily have the same "equilibrium" temperature. Essentially, then, this exercise was an attempt at curve fitting and, as shown in Figure 3, there was some improvement in the agreement between experimental and modelled profiles

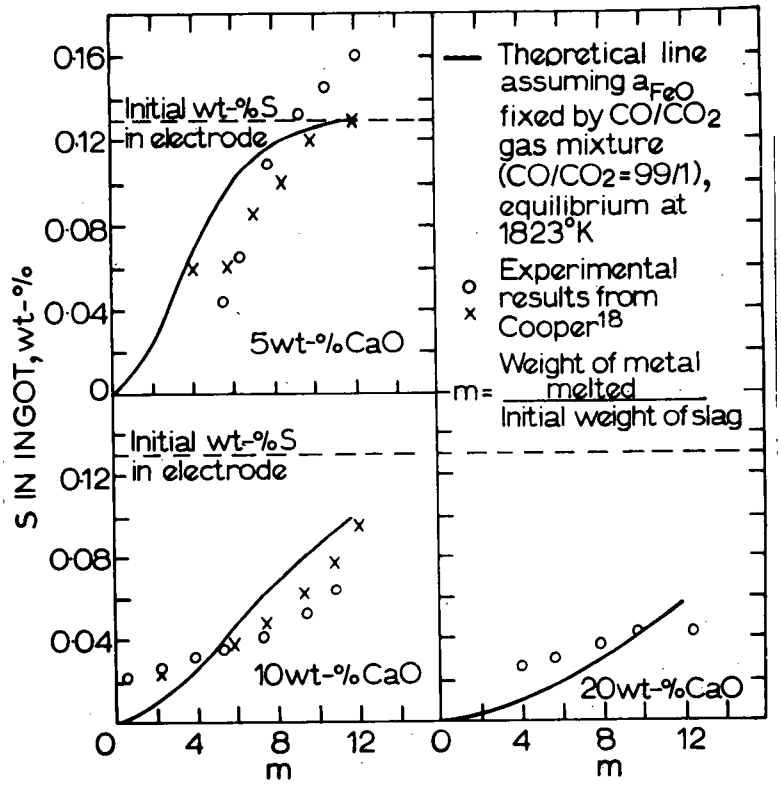

Figure 2 Comparison of Theoretical Equilibrium Model Profiles[17] with Experimental Sulphur Concentration Profiles of Cooper[99]

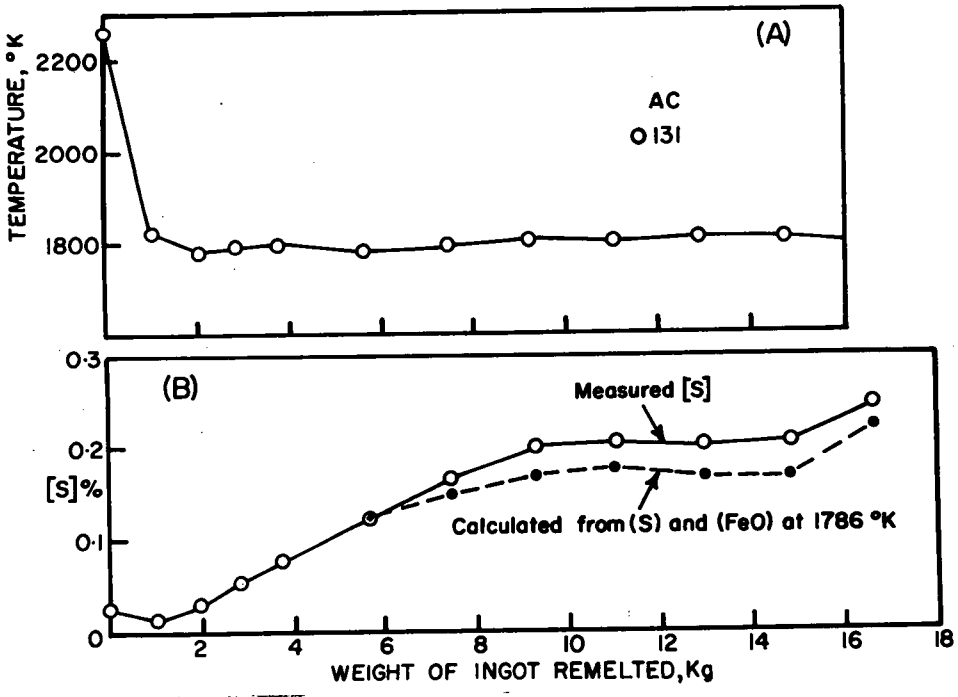

Figure 3 Use of fictitious "equilibrium" Temperature in Predicting Sulphur Concentration Profiles[22]

over the previous effort.

Knights and Perkins[21] have adopted essentially the same approach in treating losses of Ti, Al, Si from an A286 iron base alloy melted through a CaF_2 - 10% CaO - 5% Al_2O_3 - 5% TiO_2 - 1%SiO_2 slag. This attempt at modelling the ESR process as an "isothermal" system necessitated the assumption of unreasonably high temperatures (>1900°C) in order to fit the data. The agreement between model and data was reasonably good as is shown in Figure 4.

One fundamental weakness of these two modelling attempts is that mass transport was assumed to be so fast as to not be rate limiting. Another serious weakness shown clearly in these results is the necessary assumption of a unique temperature throughout the reactive region of the ESR system. One of the most obvious features of ESR is the progressive melting, heating, cooling, and freezing cycle undergone by the metal phase. What is not so obvious is that the metal, once melted, does not heat up instantaneously to the maximum observed temperature. In this process, heat transfer plays a very important role in determining the heating and cooling cycle. This has been the subject of many reports in the literature and has been well summarized by Mitchell, Szekely and Elliott.[23] Of interest here is their conclusion that the liquid metal film on the electrode tip cannot superheat more than 20 - 30°C. This conclusion is undoubtedly a result of the thinness of the metal film ($\simeq$100 μ) and the relatively high melt rate. Any large temperature differences between liquid and solid metal are accommodated instantaneously by a change in melt rate. Such observations are commonplace in ESR operations where a change in the depth of electrode immersion immediately results in a new

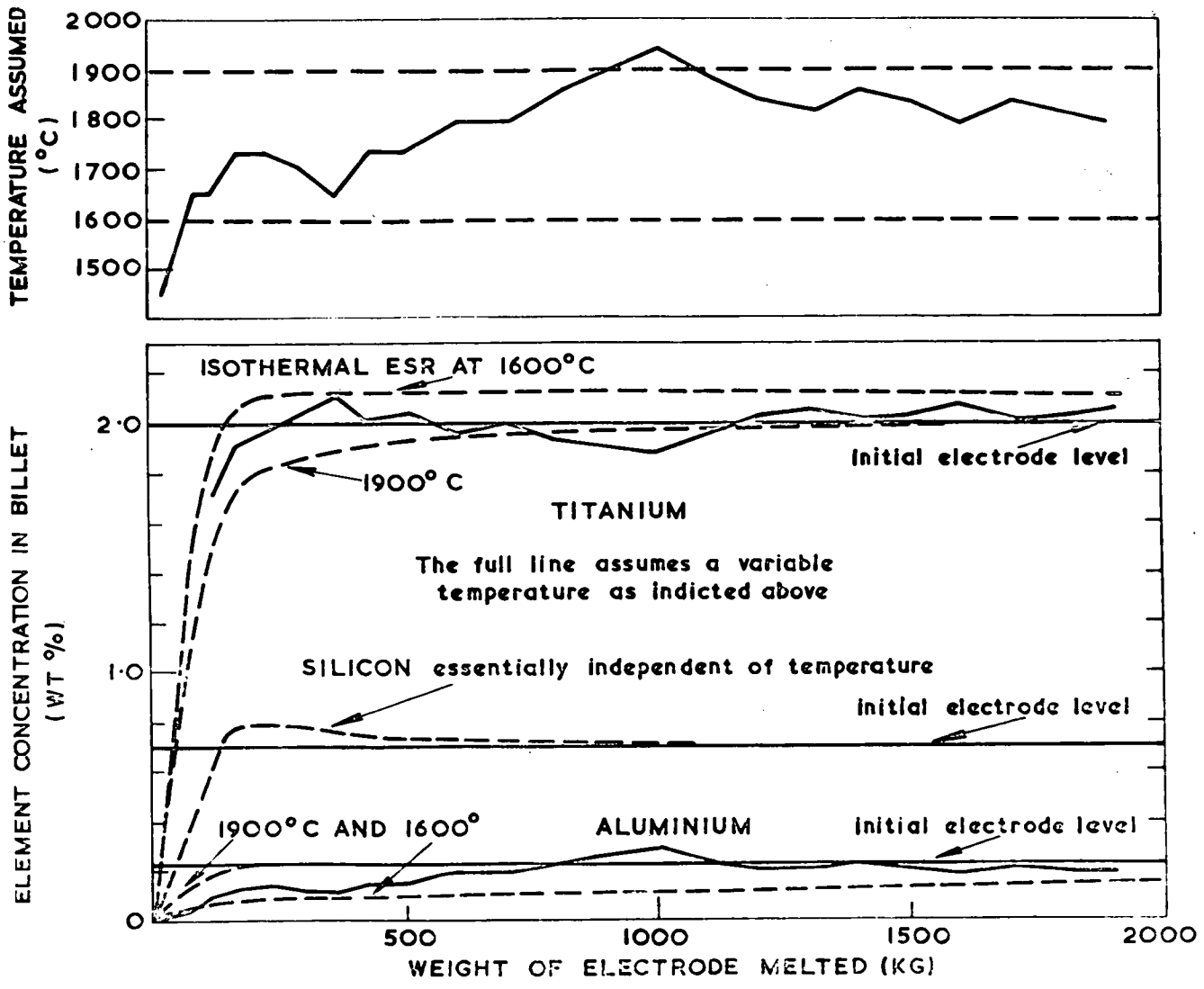

Figure 4 Comparison of Theoretical and Experimental Alloy Losses from an A286 Steel. ESR Operation Treated as an Isothermal System[21]

melt rate. On the other hand, heat transfer to the drop is sufficiently fast that drops entering the metal pool are thermally equilibrated with the slag.[24] Thus there can be a large temperature difference between liquid metal film and the drops.

1.3.2 Single Stage Reactor Models

A somewhat more realistic approach has been adopted by Etienne.[5,11] In this case, while the model assumed the familiar exponential relationship, the condition that equilibrium was not established between bulk slag and metal phases was incorporated. The mathematical formulation of this concept was first set down by Steinmetz[13] and is based on the exchange of material between a mobile and a static phase. Electroslag furnaces were considered by Etienne, in his adaptation of Steinmertz' model, to be classified with processes where the contact between phases is "transitional" (slag stationary, metal flowing), without homogenization of the metal phase subsequent to chemical reaction.

These concepts are embodied in the relationship (1.4)

$$\frac{[X]}{[X]_0} = 1 - \frac{[X]_e}{[X]_0}\,\xi \exp[-\xi Y] \qquad (1.4)$$

where

$$\xi = \rho_s \kappa_L A/\dot{W}_m$$

$$Y = W_m/W_s$$

$[X]_e$ is the X stoichiometric equivalent of the oxidant concentration initially in the slag

$$[X]_e = \frac{n}{m} \frac{MW_X}{MW_{oxid}} (Oxid)_0 \quad .$$

Equation (1.4) described the oxidative loss of element X from the metal component under the following conditions:

(i) the oxidized element was at a concentration in the metal where diffusion in the metal phase did not control mass transfer;

(ii) the oxidant was present in a limited quantity in the slag;

(iii) the system was fully described by the slag and metal components and interactions with the atmosphere were excluded.

The use of the lumped mass transfer coefficient, k_L, in (1.4) means the ESR process has been treated as a single stage reactor. In applying this model it was found that the predictions agreed with the experimental concentration time data obtained on AC melts for what was essentially an irreversible reaction (large equilibrium constant and low activity of oxidized species in the slag).(Figure 5) However, no satisfactory agreement was achieved for the corresponding DC melts using identical materials. The reason for this lack of agreement in the latter cases apparently wasthat, in the DC mode, the reactions occurring at the electrode tip/slag and ingot pool/slag interfaces were governed by electrochemical phenomena arising from concentration polarization effects at each reaction site.[25] The consequences of electrochemical control of these reactions was that different reactions occurred at the

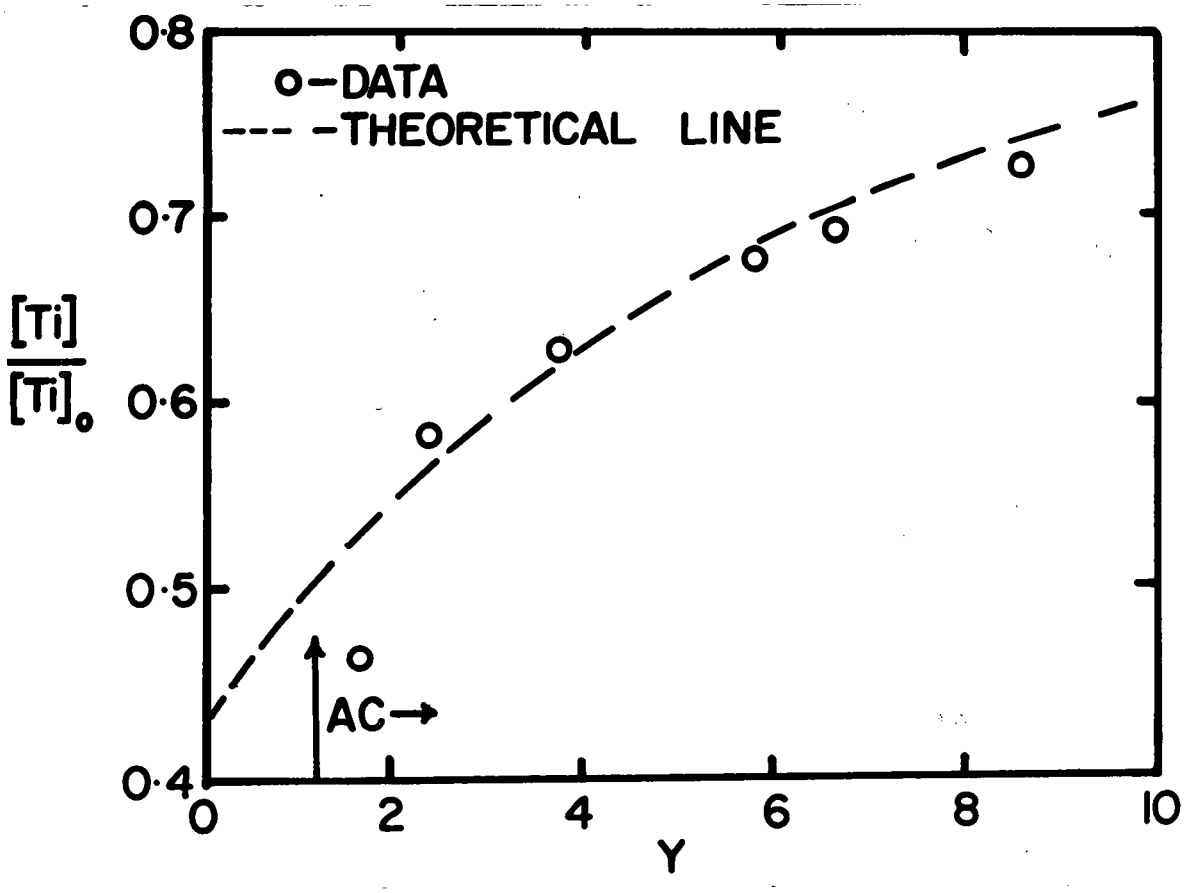

Figure 5 Comparison of Theoretical and Experimental Titanium Losses using Single-Stage Reactor Model[11]

electropositive and electronegative poles (corrosion of iron at the electropositive site and deposition of Ca or Al at the electronegative site).[25] The lumped mass transfer coefficient approach taken by Etienne dealt with only one reaction, i.e., the oxidative loss of an alloy species and thus could not be adapted to the DC case.

These electrochemical effects were far less obvious in the AC mode and there was no reason to assume that the same oxidation reaction did not occur at each reaction site. The lumped mass transfer coefficient could, therefore, be evaluated for AC melting.

This model has provided evidence of mass transfer control in AC ESR, but the real physical processes affecting mass transfer were not made apparent and factors contributing to scale-up problems were not readily identified. There is some improvement in the predictions of the single stage reactor model, but, nevertheless, a fitted parameter, the lumped mass transfer coefficient, is still required.

1.3.3 Descriptive Mass Transfer Analysis

It has been shown that the previous attempts to model the chemical composition changes occurring in ESR have met with limited success. None of them has shed much light on the particular nature of mass transfer processes controlling these changes. Nevertheless, there have been a few descriptive reports, some supported by data, of these mass transfer effects.[9,10,14,16,18] The most important of these is the work of Cooper *et al.*[14] who presented a clear and precise analysis of the ESR reaction sites undergoing desulphurization. Four reaction sites were identified quantitatively:

(i) the electrode film/slag interface;

(ii) the metal drop/slag interface;

(iii) the slag/metal pool interface;

(iv) the slag/atmosphere interface.

The experimental results of this work (Figure 6) showed that the drop/slag site was of little importance and that the greatest composition changes occurred at the film/slag interface. Possibly, the most interesting feature of their experimental results however, was that the reaction occurring at the metal pool/slag interface could be a reversion reaction. This observation has important consequences, especially in the area of inclusion formation. From the results of the analysis of the temperature regimes of the metal phase,[24] it is possible now to speculate on the reasons for this behaviour.

At the electrode film, the temperature is of the order of 150 - 200°C lower than at the metal pool. In general terms, since $\Delta G^\circ = A + BT = -RT\ln K$ we have

$$\ln K = \frac{A'}{T} + B' \qquad (1.5)$$

An increase in T will cause a decrease in K, ($A, B < 0$; for desulph, $K = 4.07$) which shifts the equilibrium from right to left. Therefore the thermodynamic driving force is reduced. This, coupled with the fact that the reactant has been somewhat depleted at the film, leads us to anticipate a reduced tendency to chemical change.

In spite of these results, there is still no real information to be learned on the mass transfer processes from this work. Crimes[18]

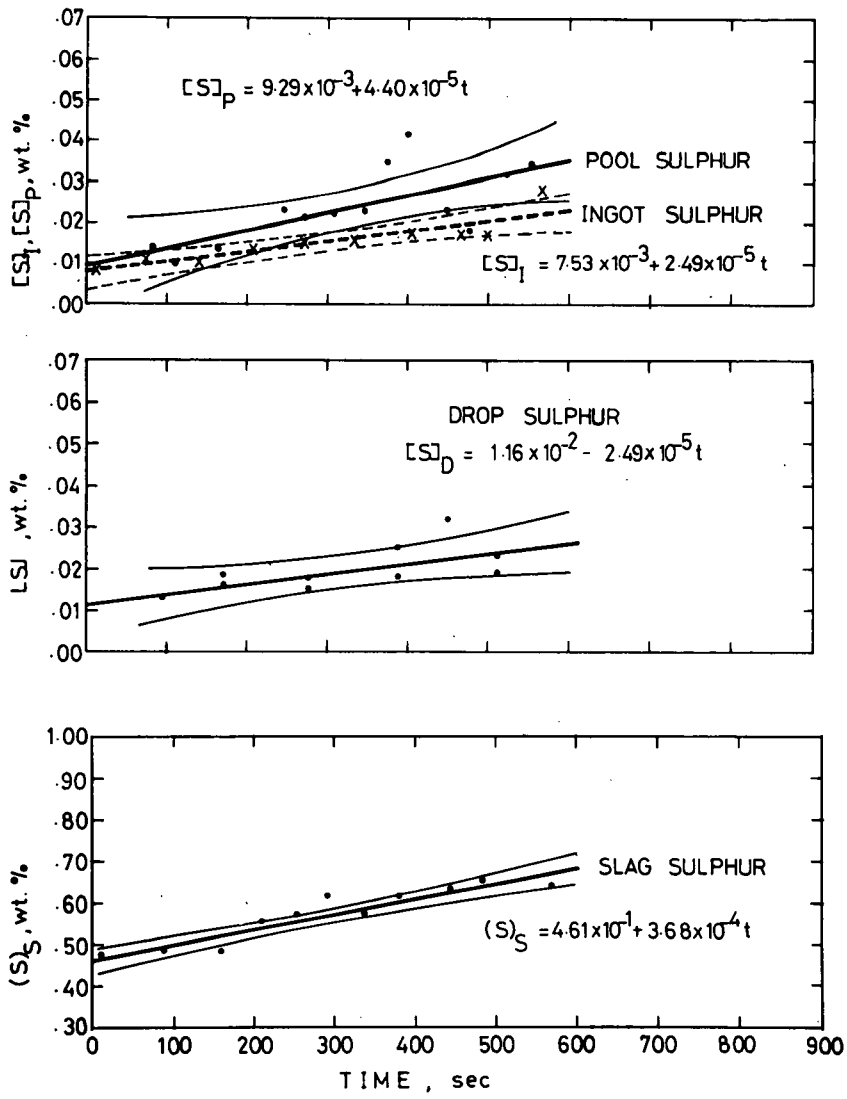

Fig. 6—$[S]_D$, $[S]_I$, $[S]_P$, and $(S)_S$ as a function of time. CaF_2–20% CaO. 30 v, 2750 A. Melt rate 13.7 g/s. Slag cap 3784 g. Pool volumes 890 and 699 ml.

has used information obtained from aqueous mass transfer to liquid metal drops to speculate on the mass transfer behaviour of drops in ESR desulphurization. His results showed that a large degree of desulphurization in ESR could be attributed to losses from the falling droplet. This result is in direct opposition to the experimental findings of Cooper.[14] The reason for this is probably that Crimes has ignored the film reaction site which removes a large amount of S leaving little available during drop fall. He has, nonetheless, showed that the drop reaction is subject to very high rates of mass transfer. The reasons why the drop site is not of particular importance in ESR are connected with the short residence time of the drop in the slag and the low area/volume ratio. These effects will be discussed in detail later.

Probably the most lucid account of mass transfer effects in electroslag processing, has been given by Patchett and Milner.[9] This work has covered a wide variety of experimental conditions during ES welding and has provided some interesting conclusions. In their initial discussion, it was noted that several different elements appear to approach equilibria at different temperatures, thus providing indirect evidence that mass transport effects control the overall extent of chemical change. In turn, experimental evidence was presented to show that, while metal melted from the electrode stock appeared to approximate equilibrium behaviour with the bulk slag, metal melted from the sides of the weld plate did not. This observation suggested that mass transfer to the droplets from the electrode was very rapid as one might expect from the relatively high slag velocities ($\simeq$100 cm sec^{-1})[9] and the intense circulation observed on the melting electrode tip. The metal

pool, containing material melted from the weld plate, had, on the other hand, a relatively low reaction area/volume ratio and was much less turbulent, both these factors greatly affecting the overall mass transfer efficiency.

It is this evidence, then, which has prompted this study of electroslag refining kinetics. The previous attempts to account for alloy element loss in ESR have indicated that *both* thermodynamic and mass transfer effects are important. However, knowledge of the specific mass transfer processes governing the overall rate is conspicuously lacking.

The progressive manner in which metal melts and is subsequently refrozen and the definitive reaction sites would appear to make the ESR process an ideal one for modelling purposes. While these features have been exploited in the heat flow analysis, very little has been done to develop any rigorous mathematical model dealing with kinetic aspects of composition control.

The objective of the present work is therefore to outline the necessary procedure for developing such a model. The proposed quantitative mass transfer model will be tested using experimental data and conclusions drawn as to the applicability of the model to commercial ESR processing.

CHAPTER 2

THE MASS TRANSFER MODEL

2.1 Introduction

The preliminary requirement in any description of mass transfer is to identify the species involved. It is evident from some of the previous work[16,21] that systems of excessive complexity were chosen for experimental purposes. For example, Knights and Perkins[21] studied the oxidative losses from A286 alloy containing 2% Ti, 0.23% Al and 0.7% Si melted through a CaF_2 - 10% CaO - 5% Al_2O_3 - 5% TiO_2 - 1% SiO_2 slag. Part of the lack of agreement between their "equilibrium" model and the experimental results may certainly be ascribed to the complexity of this system and the subsequent uncertainty of the appropriate activities.

For this study, a much simpler system was chosen. Following a preliminary investigation, it was found that, for the melting of AISI 1018 through CaF_2 - CaO slags, manganese was the only element to be oxidized from the metal at the levels of FeO commonly found in ESR processing. It was apparent that this was the sole reaction occurring and hence this was a suitably simple system on which to test a mass transfer model. In addition, the thermochemistry of the CaF_2 - CaO - MnO and CaF_2 - CaO - FeO systems were sufficiently understood to provide reasonable estimates of the necessary activity coefficients. The reaction to be modelled then is the oxidation of Mn in steel by FeO in CaF_2 - CaO slags.

It is generally agreed that CaF_2-based fused salts are completely ionic in nature.[7,17,27,30] Therefore, we can consider FeO and MnO in terms of the ionic species involved, namely, Fe^{2+}, Mn^{2+}, O^{2-}. Oxidation may then be treated as a simple exchange reaction:

$$[Mn] + (Fe^{2+}) \underset{\leftarrow}{\overset{\rightarrow}{}} Fe(\ell) + (Mn^{2+}) \qquad (2.1)$$

As pointed out in 1.3.1 the ESR process is, of necessity, a heat exchanger. A question one might ask in consideration of the mass transport phenomena is "To what extent does the heat transfer regime interact with the mass transfer processes?" It has been shown, for example, that the temperatures of the phase boundaries are not all equal (1.3.1). One must decide whether or not these temperatures remain relatively unchanged throughout the entire course of ingot production. There is no evidence, at present, to suggest that the phase boundary temperatures do change during a melt on the small 3" ϕ furnace used here.[23,56] The major effect of increasing ingot length is to increase the depth of the liquid metal pool,[56] but this is attributed to the displacement of the axial heat sink (baseplate cooling) with respect to the ingot top and not to an increase in slag temperature. We may, therefore, consider the temperatures of these interfaces to be referred to a quasi-steady state, i.e., constant for our purposes.

The above arguments highlight an important aspect of mass transfer modelling in the ESR system, which is the coupling of the heat and mass transfer processes. The coupled behaviour of these two phenomena will be made more apparent as we proceed with the development of the mass transfer model in which it will be shown that heat transfer

analysis provides information which is essential to a successful mass transfer model.

2.2 Mathematical Formulation

An exchange reaction involves a sequence of steps including transport processes to and from the phase boundaries and chemical reaction at the boundary.[26] The situation is presented schematically in Figure 7.

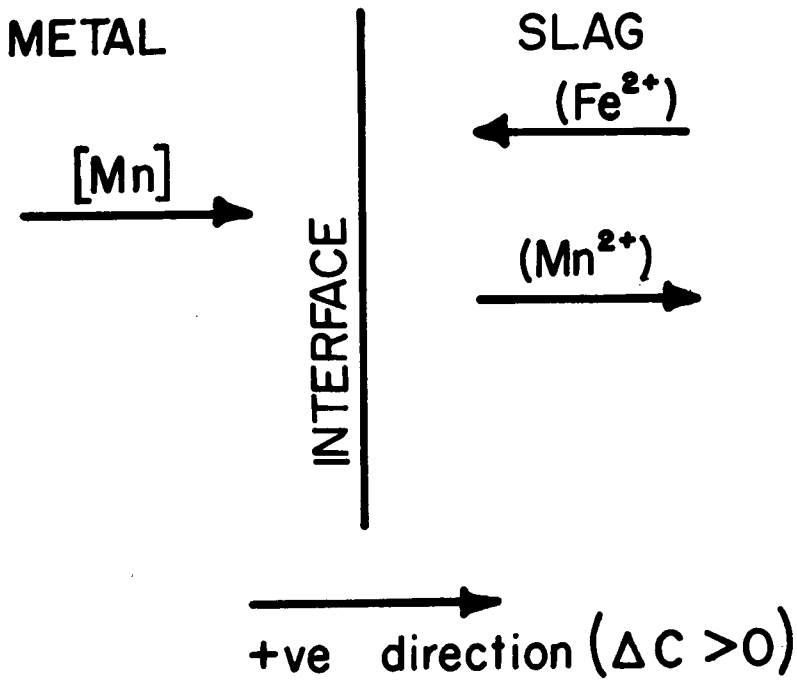

Figure 7 Schematic Representation of Fluxes

It is assumed here that equilibrium between the species [Mn], (Mn^{2+}) and (Fe^{2+}) exists at the phase boundary since the reaction of (6) and any adsorption or desorption steps are very fast compared to the rate of transport to the interface.[31] In this analysis, no single transport process is considered as a possible rate controlling step. Essentially, it is this assumption that permits a description of the entire mass transfer process by using phenomenological flux equations. Since liquid iron is the metal solvent in the system, the transport of iron in the metal can be discounted. The remaining three flux equations may be written, such that the concentration driving forces are always greater than zero and transfer from metal to slag is defined as positive.

For the transport of [Mn] to the slag/metal interface:

$$\frac{\dot{n}_{Mn}}{A} = k_{Mn}([Mn]_b - [Mn]_i) \qquad (2.2)$$

for transport of (Mn^{2+}) away from the interface:

$$\frac{\dot{n}_{Mn^{2+}}}{A} = k_{Mn^{2+}}((Mn^{2+})_i - (Mn^{2+})_b) \qquad (2.3)$$

and for transport of (Fe^{2+}) to the interface:

$$\frac{-\dot{n}_{Fe^{2+}}}{A} = k_{Fe^{2+}}((Fe^{2+})_b - (Fe^{2+})_i) \qquad (2.4)$$

The symbols are described at the end of the thesis.

In addition, we have the equilibrium relationship for fast interfacial reaction:

$$\Omega = \frac{(Mn^{2+})_i}{[Mn]_i (Fe^{2+})_i} \quad (mol\ cm^{-3})^{-1} \tag{2.5}$$

If we consider, now, that the process as a whole occurs at steady state then,

$$\dot{n}_{Mn} = \dot{n}_{Mn^{2+}} = -\dot{n}_{Fe^{2+}} = \dot{n} \tag{2.6}$$

It is apparent from a simple schematic representation of the concentration profiles of [Mn], (Mn^{2+}), (Fe^{2+}), (Figure 8) that the interfacial

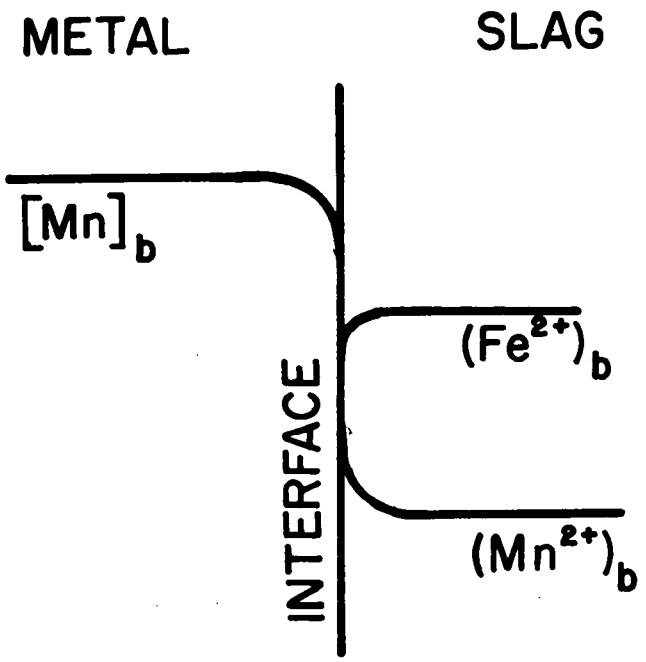

Figure 8 Schematic Concentration Gradients at Slag/Metal Phase Boundary

concentrations of these three species are unknown. They must therefore be solved for, like $\dot{n}$, using the four equations (2.2 - 2.5) in four unknowns.

Etienne[5] assumed that metal phase transport was not rate controlling in evaluating his lumped mass transfer coefficient but there is no basis for this assumption evident at this stage of the analysis and so we must attempt to solve for all of these interfacial quantities.[26]

Rearranging (2.5) and substituting into (2.4) we obtain:

$$-\frac{\dot{n}_{Fe^{2+}}}{A} = k_{Fe^{2+}}\left[(Fe^{2+})_b - \frac{(Mn^{2+})_i}{\Omega[Mn]_i}\right]$$

multiplying by $\frac{\Omega[Mn]_i}{k_{Fe^{2+}}}$

$$-\frac{\dot{n}_{Fe^{2+}}}{A}\frac{\Omega[Mn]_i}{k_{Fe^{2+}}} = \Omega[Mn]_i(Fe^{2+})_b - (Mn^{2+})_i \qquad (2.7)$$

From (2.3):

$$\frac{\dot{n}_{Mn^{2+}}}{A}\frac{1}{k_{Mn^{2+}}} = (Mn^{2+})_i - (Mn^{2+})_b \qquad (2.8)$$

Upon adding (2.7), (2.8) and using relation (2.6):

$$\frac{\dot{n}}{A}\left\{\frac{\Omega[Mn]_i}{k_{Fe^{2+}}} + \frac{1}{k_{Mn^{2+}}}\right\} = \Omega[Mn]_i(Fe^{2+})_b - (Mn^{2+})_b$$

Therefore:

$$\frac{\dot{n}}{A} = \frac{\Omega[Mn]_i(Fe^{2+})_b - (Mn^{2+})_b}{\frac{\Omega[Mn]_i}{k_{Fe^{2+}}} + \frac{1}{k_{Mn^{2+}}}} \qquad (2.9)$$

Equating (2.2) and (2.9):

$$k_{Mn}[Mn]_b - k_{Mn}[Mn]_i = \frac{\Omega[Mn]_i(Fe^{2+})_b - (Mn^{2+})_b}{\frac{\Omega[Mn]_i}{k_{Fe^{2+}}} + \frac{1}{k_{Mn^{2+}}}}$$

Multiplying by $\left\{ \frac{\Omega[Mn]_i}{k_{Fe^{2+}}} + \frac{1}{k_{Mn^{2+}}} \right\}$:

$$\frac{\Omega k_{Mn}[Mn]_b[Mn]_i}{k_{Fe^{2+}}} - \frac{\Omega k_{Mn}[Mn]_i^2}{k_{Fe^{2+}}} + \frac{k_{Mn}[Mn]_b}{k_{Mn^{2+}}} - \frac{k_{Mn}[Mn]_i}{k_{Mn^{2+}}}$$

$$= \Omega[Mn]_i(Fe^{2+})_b - (Mn^{2+})_b$$

Collecting terms in $[Mn]_i$:

$$- \frac{\Omega k_{Mn}}{k_{Fe^{2+}}} [Mn]_i^2 + \{ \frac{\Omega k_{Mn}}{k_{Fe^{2+}}} [Mn]_b - \frac{k_{Mn}}{k_{Mn^{2+}}} - \Omega(Fe^{2+})_b \} [Mn]_i$$

$$+ \frac{k_{Mn}}{k_{Mn^{2+}}} [Mn]_b + (Mn^{2+})_b = 0$$

Finally, multiplying by $\frac{-k_{Fe^{2+}}}{\Omega k_{Mn}}$ we obtain:

$$[Mn]_i^2 + \{ \frac{k_{Fe^{2+}}}{\Omega k_{Mn^{2+}}} + \frac{k_{Fe^{2+}}}{k_{Mn}} (Fe^{2+})_b - [Mn]_b \} [Mn]_i$$

$$- \frac{k_{Fe^{2+}}}{\Omega} \{ \frac{[Mn]_b}{k_{Mn^{2+}}} + \frac{(Mn^{2+})_b}{k_{Mn}} \} = 0 \qquad (2.10)$$

This is a quadratic equation of the form

$$a[Mn]_i^2 + b[Mn]_i - c = 0$$

where $a = 1$

$$b = \frac{k_{Fe^{2+}}}{\Omega k_{Mn^{2+}}} + \frac{k_{Fe^{2+}}}{k_{Mn}} (Fe^{2+})_b - [Mn]_b \qquad (2.11\text{-}b)$$

$$c = \frac{k_{Fe^{2+}}}{\Omega} \left\{ \frac{[Mn]_b}{k_{Mn^{2+}}} + \frac{(Mn^{2+})_b}{k_{Mn}} \right\} \qquad (2.11c)$$

Therefore,

$$[Mn]_i = \frac{-b \pm (b^2 + 4c)^{1/2}}{2} \qquad (2.11a)$$

Equation (2.11a) is a relationship giving the value of $[Mn]_i$ in terms of measurable parameters: bulk concentrations, mass transfer coefficients and equilibrium constants. Equation (2.11a) can be substituted into (2.2) to yield (2.12)

$$\frac{\dot{n}_{Mn}}{A} = k_{Mn} \left\{ [Mn]_b - \frac{-b \pm (b^2 + 4c)^{1/2}}{2} \right\} \qquad (2.12)$$

The rate of change of $[Mn]_b$, etc. with time finally can be obtained from a mole balance on the respective species as follows

	Rate in	− Rate out	= Accumulation	
for $[Mn]_b$:		$-\dot{n}_{Mn}$	$= V_m d[Mn]/dt$	
for $(Fe^{2+})_b$		$-(-\dot{n}_{Fe^{2+}})$	$= V_s d(Fe^{2+})d/t$	(2.13)
for $(Mn^{2+})_b$	$\dot{n}_{Mn^{2+}}$		$= V_s d(Mn^{2+})/dt$	

The resulting differential equation written for Mn is:

$$\frac{d[Mn]}{dt} = \frac{-A}{V_m} k_{Mn} \{ [Mn]_b - [\frac{-b \pm (b^2 + 4c)^{1/2}}{2}] \} \qquad (2.14)$$

This expression is valid for any liquid metal/slag interface. The concentrations $(Mn^{2+})_b$ and $(Fe^{2+})_b$ may also be found by relation (2.15).

$$d(Mn^{2+})_b = -d(Fe^{2+})_b = -d[Mn]_b \frac{V_m}{V_s} \qquad (2.15)$$

2.3 Evaluation of Mass Transfer Model Parameters

2.3.1 Bulk Concentrations

Bulk concentrations are not, strictly speaking, parameters of the model. Nevertheless, one must have some knowledge of these variables for the arguments to follow. Any values of [Mn], (Mn^{2+}), (Fe^{2+}) used below represent typical levels found during the experimental melt program (Chapters 3, 4).

2.3.2 Molar Equilibrium Constant

The molar equilibrium constant, Ω, for the reaction (2.1) has been defined in terms of molar concentrations:

$$\Omega = \frac{(Mn^{2+})_i}{[Mn]_i (Fe^{2+})_i} \qquad (2.5)$$

Ω can be expressed as a function of the normal equilibrium constant, K, for the reaction (2.1) where

$$K = \frac{(a_{MnO})_i}{[a_{Mn}]_i (a_{FeO})_i}$$

$$= \frac{\gamma_{MnO}(X_{MnO})_i}{\gamma_{Mn}[X_{Mn}]_i \gamma_{FeO}(X_{FeO})_i} \qquad (2.16)$$

By taking into account activity coefficients and factors to convert units of concentration, we have:

for dilute solutions of species i:

$$X_i = \frac{\text{wt \% i}}{MW_i \left\{ \frac{\text{wt \% j}}{MW_j} \right\}} \qquad (2.17)$$

Also, $\text{wt \% i} = [c_i] \frac{100 \times MW_i}{\rho_{bulk}}$

After substitution in (2.16) and cancellation

$$K = \frac{\gamma_{MnO}}{\gamma_{Mn}\gamma_{FeO}} \quad \frac{\rho_{Fe}(Mn^{2+})_i}{55.85\ [Mn]_i (Fe^{2+})_i} \qquad (2.18)$$

Solving for the Ω group (Equation 2.5):

$$\Omega = \frac{55.85\ K\ \gamma_{Mn}\gamma_{FeO}}{\rho_{Fe}\gamma_{MnO}} \tag{2.19}$$

Values for K may be found from the literature. Bodsworth[32] (p. 397) quotes a number of expressions for K in the form,

$$K' = \frac{a_{MnO}}{a_{FeO}\ \%\ Mn} = \frac{A}{T} - B \tag{2.20}$$

The most commonly used values for A, B[34] are those of Chipman et al.,[33] where

$$K' = 6440/T - 2.95 \tag{2.21}$$

It is assumed in 2.21 that Mn, in dilute solutions of Fe, behaves ideally[32] ($\gamma_{Mn} = 1$). From a comparison of (2.20) to (2.16)

$$K = K' \frac{\%\ Mn}{X_{Mn}}$$

and from (2.17)

$$\frac{\%\ Mn}{X_{Mn}} = \frac{MW_{Mn}}{.5585}$$

$$\therefore \quad K = K' \frac{MW_{Mn}}{.5585\ \gamma_{Mn}}$$

On substitution into (2.19)

$$\Omega = \frac{K'\ \gamma_{FeO}(100 \times MW_{Mn})}{\rho_{Fe}\ \gamma_{MnO}} \qquad (2.22)$$

Ω is now a function of the variables K', γ_{FeO} and γ_{MnO}. In assessing the value of K', one must specify the temperature of the interface involved. In this instance, we are concerned with three different reaction sites. In Section 1.3.1, it has been shown that the electrode film does not superheat more than 20 - 30°C. The interface temperature was, therefore, taken to be 1525°C, following the arguments of Appendix V.2. The temperature at the metal pool/slag interface has been measured in the U.B.C. ESR unit,[35] under similar experimental conditions and found to be ≃1675°C. Hence, this value was used to calculate K' at this site. This temperature was assumed constant over the whole interface, although radial variations of ±50°C may exist.[56] The falling droplets were assumed to equilibrate quickly with the slag (cf. Appendix V.3) and an average drop/slag interface temperature is used, equal to the metal pool/slag temperature.

Thermodynamic studies have been carried out on the systems CaF_2 - CaO - FeO[36,27] and CaF_2 - CaO - MnO.[37] In both cases a strong positive deviation from ideal-solution laws have been found, with MnO

showing a larger deviation. With increasing lime content, this tendency to immiscibility is found to decrease substantially, reflecting a greater affinity of FeO and MnO for CaO than for CaF_2. The measured activities also appear to be only slightly affected by temperature, especially at higher lime levels.[36]

The value of γ_{FeO} used in this work is taken from the work of Hawkins and Davies.[27] Although there is some slight deviation from Henry's Law behaviour in CaF_2 - high lime melts apparent from Figure 9, the solutions of FeO in CaF_2 - 20% CaO can be considered to obey Henry's Law.[36] The value used for γ_{FeO} is, therefore, 3.0, midway between the 20 mole % and 30 mole % CaO lines of Figure 9.

A consideration of Figure 10, however, shows that this behaviour may not, in fact, be true for solutions of MnO in CaF_2 - CaO. Although no data is available for 20% CaO in CaF_2, it is evident that γ_{MnO} may not approach Henry's Law (γ_{MnO} = const = γ°_{MnO}) even in dilute solution. The values to be used will be somewhat lower than those reported for 15% CaO. Because of this uncertainty, values of γ_{MnO} used in the model have been fitted from experimental data.

The values of γ_{MnO} used in the model must be based on the interfacial concentration, $(Mn^{2+})_i$ (Equation 2.16). In model runs on the computer, some arbitrary initial value of γ_{MnO} was read in with the data. The value of Ω was calculated by Equation 2.22 using the initial value of γ_{MnO}. An additional calculation of Ω using Equation 2.5 was then performed using the expressions derived for the interfacial quantities, $[Mn]_i$ (Equation 2.11a), $(Mn^{2+})_i$ and $(Fe^{2+})_i$ (Appendix III.3, Equations A3.36 and A3.38 respectively). A new value of γ_{MnO}, γ_{MnO}' was obtained by

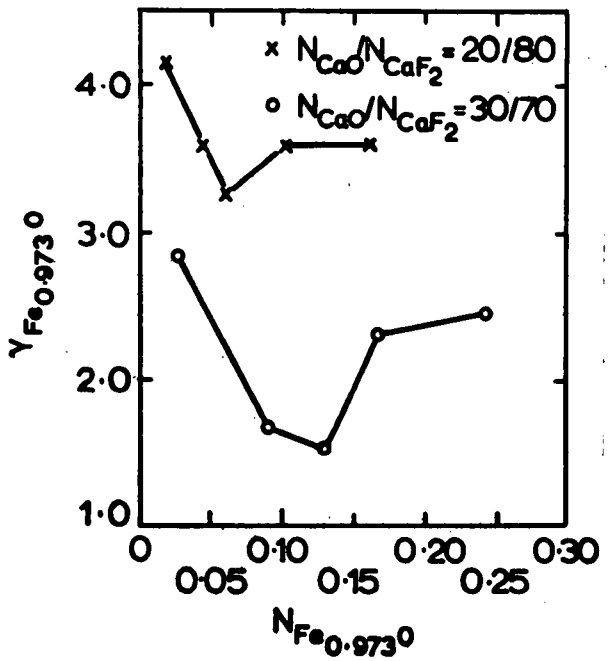

Figure 9 γ_{FeO} versus N_{FeO} for Constant Mole Ratio at 1450°C[27]

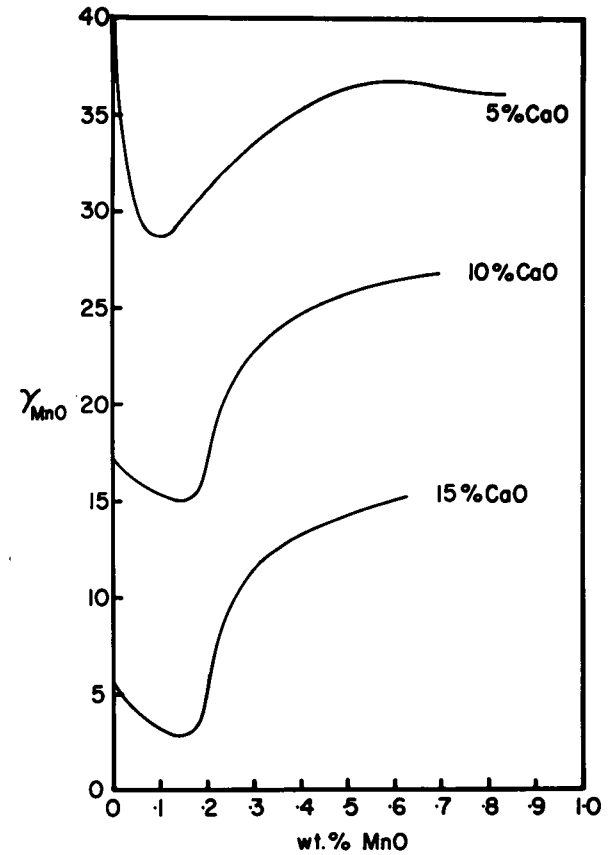

Figure 10 γ_{MnO} versus wt % MnO in Various CaF_2-CaO Slags at 1500°C. (Replotted from Ref.37)

dividing the first value of Ω calculated, by the latter and multiplying this quotient by the original value of γ_{MnO}, such that

$$\gamma'_{MnO} = \frac{\dfrac{K'\gamma_{FeO}(100 \times MW_{Mn})}{\rho_{Fe}\,\gamma_{MnO}}}{\dfrac{(Mn^{2+})_i}{[Mn]_i\,(Fe^{2+})_i}} \times \gamma_{MnO}$$

This procedure (subroutine OMT, Appendix IV) was carried out iteratively until γ'_{MnO} differed from γ_{MnO} by a prescribed tolerance ($\pm.1$). Generally, only one or two iterations were needed for convergence after the first iterative sequence.

In this way, the data for Figure 18 (Chapter 4) was obtained. The values obtained for γ_{MnO} as a function wt % MnO appear to show a high degree of internal consistency (i.e. a small degree of scatter over a large number of data points. They also are consistent with the expected values of γ_{MnO} at CaO levels in excess of 15% CaO.

2.3.3 Reaction Sites Considered in Modelling

The mass transfer Equation (2.14) has been derived for any liquid metal/slag phase boundary. In order to evaluate the phenomenological mass transfer coefficients k_{Mn}, $k_{Mn^{2+}}$, $k_{Fe^{2+}}$,consideration must be made of the particular reaction interfaces which are operative in the ESR system used in the experimental program.

The work of Cooper *et al.*[14] has shown (1.3.3) that there are four major reaction sites, namely:

1. electrode metal film/slag interface
2. drop/slag interface
3. metal pool/slag interface
4. slag/atmosphere interface.

However, throughout the experimental program (Chapter 3) an inert gas atmosphere was used, and thus eliminated the necessity of considering (4) above, as contributing to the overall rate of mass transfer.

It is necessary, now, to consider the nature of the mass transfer processes involved at each of the remaining sites. This is complicated by the dependence of mass transfer coefficients on flow conditions adjacent to the interfaces.

2.3.4 Mass Transfer at the Electrode Tip/Slag Interface

The nature of flow on the electrode tip has been considered by Etienne.[5] He has derived an expression for the thickness of the metal film, δ, on conical electrode tips, where flow is controlled by gravitational forces. The interaction effects of the slag (momentum, surface tension) are not known with sufficient precision to be expressed mathematically and thus are not included in the analysis. We have, then

$$\delta(\text{cm}) = \left[\frac{3\mu_m \dot{W}'_m}{2\pi(\rho_m - \rho_s)g \; x \sin\theta\cos\theta} \left(1 - \frac{x^2\cos^2\theta}{R^2}\right) \right]^{1/3} \qquad (2.23)$$

where

$\dot{W}'_m$ is the volumetric melt rate $cm^3 sec^{-1}$

θ is the cone angle

x is the length of cone edge in contact with the slag.

Film profiles calculated from this equation have been plotted in Figure 11. Typical constants used are:

$\theta = 5° - 50°$

$\mu_m = 0.05$ poise

$\rho_m = 7.2$ gm cm^{-3}

$\rho_s = 2.6^{38}$ gm cm^{-3}

$R = 1.91$ cm

$\dot{W}'_m = 0.36\ cm^3 sec^{-1}$

The film thickness is seen to vary from 50 - 200 μ over most of the surface of the cone if the cone angle is approximately 45° (as is usually observed on 1 1/2" ϕ electrodes). This magnitude of film thickness is consistent with numerous observations.[40,41]

We may draw some conclusion as to the type of flow that might be expected with such film thickness using the Reynolds Number for a falling film on a vertical wall[39] and the physical constants above:

$$Re = \frac{4}{3} \frac{\delta^3 g}{\nu^2} \qquad (2.24)$$

for $\delta = 200\ \mu$ $\quad Re = 205$

$\delta = 50\ \mu$ $\quad Re = 3.2$

This indicates the likelihood of rippling on the electrode film during laminar flow.[39] Since the nature of this rippled surface is

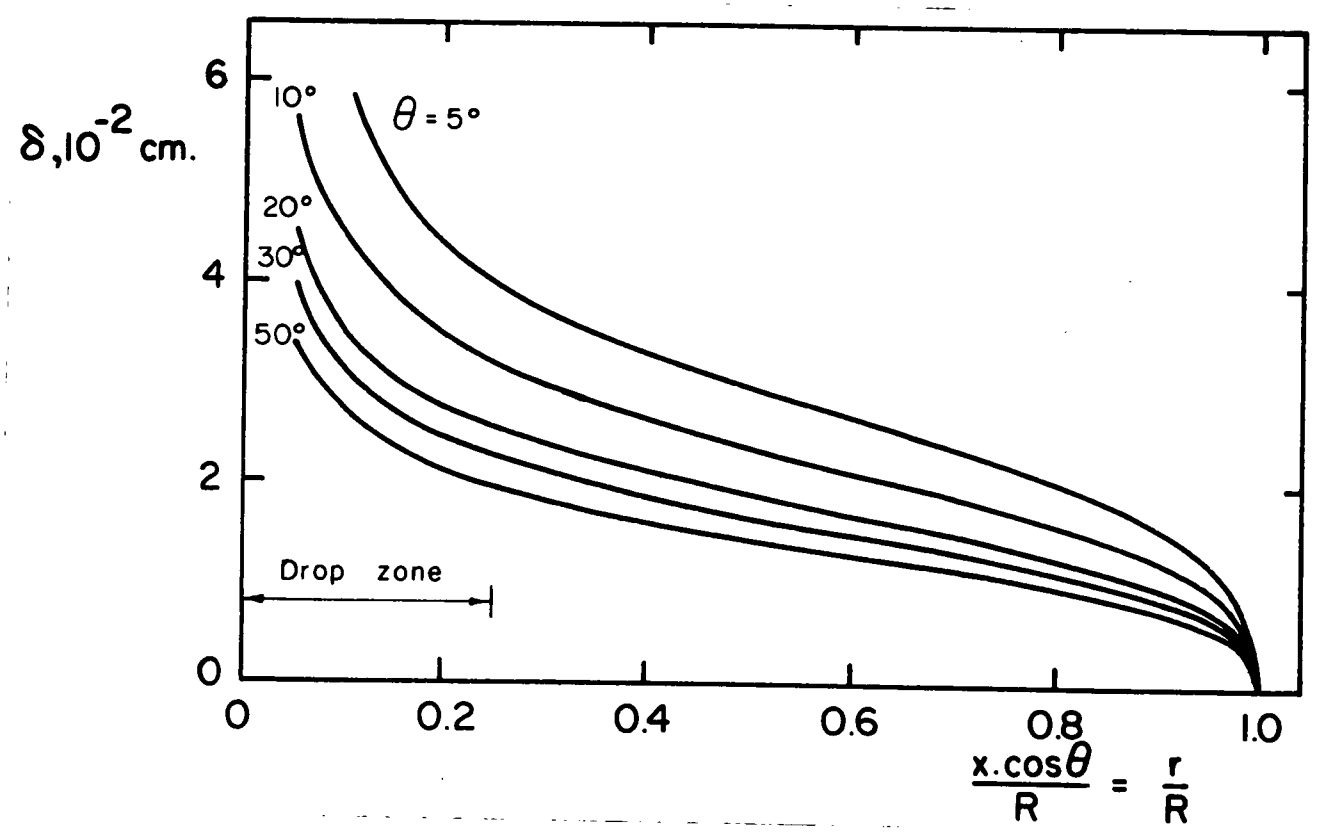

Figure 11 Thickness of Liquid Metal Film on Conical Electrode Tip[5]

not known, a smooth interface will be assumed.

In order to describe the mass transfer across this interface we must adopt some model in order to evaluate the mass transfer coefficients. The two classical models for the mechanism of mass transfer between two phases are the film theory[42] and the penetration theory.[43-46] The film theory assumes that there is a region in which steady state transfer is controlling; the pentetration theory assumes that the interface is continuously renewed by eddies of fresh material from the bulk liquid and that unsteady state transfer into or from these eddies is controlling in this region. In the absence of any other resistances the film theory predicts a first order dependence of the transfer rate on diffusivity while the penetration theory predicts a square root dependence. The average mass transfer coefficients for these models are;

$$\text{Film Theory:} \quad k_F = \frac{D}{L} \quad (\text{cm sec}^{-1}) \tag{2.25}$$

where L is the thickness of the region in which molecular transfer is controlling.

$$\text{Penetration Theory:} \quad k_p = 2(D/\pi t_e)^{1/2} \quad (\text{cm sec}^{-1}) \tag{2.26}$$

where t_e is the time that an eddy is in contact with the interface.

Which of these models is most applicable to describe mass transfer at the electrode tip/slag interface can be established using the criterion obtained by Toor and Marchello,[47] in which the penetration theory holds for short contact times and vice versa for the film theory.

A short contact time is said to exist[47] when the group

$$t_e \; D/L^2 \quad \text{is small}$$

In other words the penetration theory holds when

$$t_e \ll L^2/D \tag{2.27}$$

and the film theory holds when.

$$t_e \gg L^2/D \tag{2.28}$$

An expression for t_e on the electrode film has been derived by Etienne[5] with the following result for the free film flow discussed above.

$$t_e = 3.35 \left(\frac{2\pi \cos\theta}{3\,W'_m}\right)^{2/3} \left(\frac{\mu_m}{g\rho \sin\theta}\right)^{1/3} \left(\frac{R}{\cos\theta}\right)^{5/3} \tag{2.29}$$

For the typical conditions described in the evaluation of δ, the film thickness (Equation 2.23) we find that

$$t_e \simeq .95 \text{ secs}$$

Since the metal film was assumed to be in laminar flow, and is very thin, the mass transfer boundary layer cannot be expected to be much less than the actual metal film thickness. The diffusion

coefficient of Mn in iron has been estimated to be $1.(10^{-4})$[48,49] $cm^2 sec^{-1}$. Taking L to be $2(10^{-2})$ cm, we have, from Equation 2.27

$$t_e << 2(10^{-2})^2/(10^{-4})$$
$$<< 4$$

Since the estimated t_e for this case was found to be .95 sec the mass transfer coefficient on the metal side of the electrode tip/slag interface (i.e. k_{Mn}) can be calculated, assuming the penetration theory to hold, by Equation 2.26. For a film thickness of only 50 μ, this inequality does not hold since L^2/D is equal to .25 sec. But, as can be seen from Figure 11, the proportion of electrode covered by this thickness of film is small. Therefore,

$$k_{Mn,FILM} = 2(D/\pi t_e)^{1/2}$$
$$= 2(2(10^{-4})/\pi \times .95)^{1/2}$$
$$\therefore \quad k_{Mn,FILM} = 0.012 \text{ cm sec}^{-1}$$

For the slag side of the interface, for which the coefficients $k_{Fe^{2+}}$, $k_{Mn^{2+}}$ must be evaluated, we must determine the nature of the flow in the slag. It has been observed that the slag velocity varies from 5 - 10 cm sec^{-1} in ESR units ranging from 76 mm ϕ[5] to 300 mm ϕ.[50] The major driving force for slag motion is not thermal convection, but rather forced convection due to the constriction of the current path as the current passes through the electrode tip and then broadens out to

take the path of least resistance.[9] It was shown by Maecker[51] that, where such a current path exists, there occurs a Lorentz - force induced, high velocity motion away from the constriction. The maximum velocity of the fluid is expressed by

$$V_{max} = \left(\frac{2I^2}{\rho_s \pi R^2} \right)^{1/2} \quad (cm\ sec^{-1}) \tag{2.30}$$

where

I = absolute current

R = radius of the electrode

In the U.B.C. ESR unit, currents in the order of 1000 amps for the 76 mm ϕ furnace and a 38 mm ϕ electrode:

$$V_{max} \simeq \left(\frac{2(100)^2}{2.6\pi \times (2)^2} \right)^{1/2} \simeq 25\ cm\ sec^{-1}$$

The approximate pattern produced by this force is shown schematically in Figure 12.[66] Although slag flow rates of this magnitude have not been observed in ESR, velocities close to the maximum are seen in ES welding. In ESR, the imposed circulation pattern of the slag would be opposed by the thermal gradients found in the system[38] which partially accounts for the lower observed flow rates. It is reasonable to use a value of 10 cm sec^{-1} for the mass transfer calculations.

The contact time, t_e, of an element of slag with the metal film will be the time taken for that element to traverse the face of the electrode tip. For this system that time is about .2 sec.

It is possible to estimate the mass transfer boundary layer

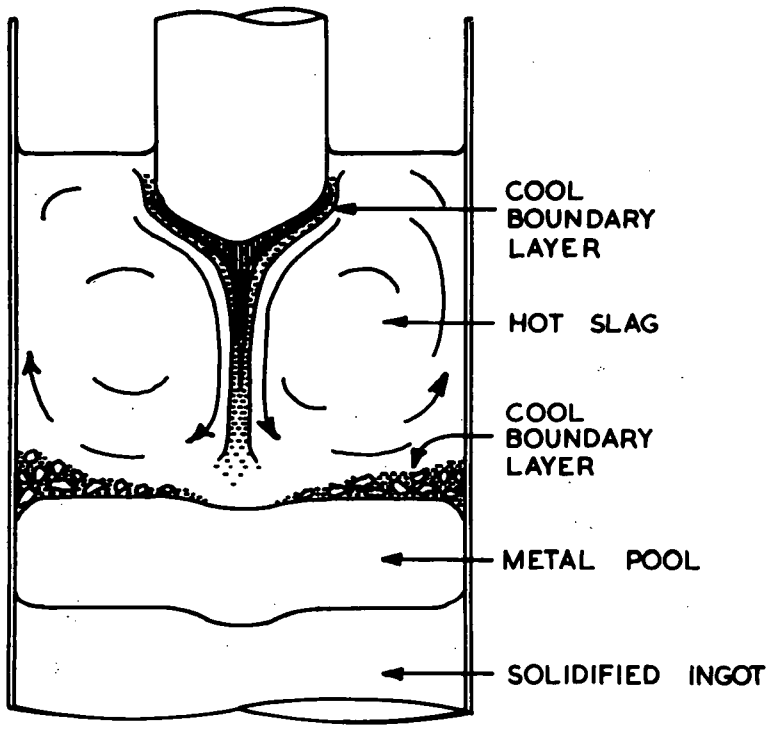

Figure 12 Schematic Flow Pattern for Typical ESR Furnace

thickness, L, by considering the electrode tip to be a flat plate. Assuming that flow is laminar and that diffusion controls the rate of transport, the hydrodynamic boundary layer can be shown to have the thickness[52]

$$\Delta(x) = 3.46 \left(\frac{\nu_s x}{v_\infty} \right)^{1/2} \qquad (2.31)$$

where x is the distance from the leading edge of the flat plate and v_∞ is the bulk velocity. Since $\nu_s = \mu_s/\rho_s$ where $\mu_s \simeq 75$ centipoise[38]

and $\rho_s \simeq 2.6$ gm cm^{-3} [38], $v_\infty = 10$ cm sec^{-1}.

$$\Delta(x) = \left(\frac{12 \times .75}{2.6 \times 10}\right)^{1/2} x^{1/2} = .59\, x^{1/2} \text{ (cm)} \qquad (2.32)$$

The relationship between the hydrodynamic boundary layer thickness and the mass transfer boundary layer thickness for diffusion controlled transport processes is given by[52]

$$\frac{L}{\Delta} = Sc^{-1/3} \qquad (2.33)$$

where L is the mass transfer boundary layer thickness in cm and

$$Sc = \frac{\mu}{\rho D} = \text{Schmidt \#}$$

Since the diffusion coefficients of Mn^{2+} and Fe^{2+} in CaF_2 - CaO are not known, a value of $5.(10^{-5})$ cm^2 sec^{-1} will be used for both, this being the value used for $D_{Fe^{2+}}$ in basic open hearth slags.[34] The consequences of this are that $k_{Fe^{2+}}$ will be equal to $k_{Mn^{2+}}$.

Evaluating the Schmidt Number and substituting (2.33) into (2.32) we obtain

$$L = 3.4(10^{-2})\, x^{1/2} \text{ (cm)} \qquad (2.34)$$

If x is approximately equal to 2, then the mass transfer boundary thickness, $L = 4.8(10^{-2})$ cm. Recalling the inequality, 2.27,

$$t_e \ll L^2/D$$

we have

$$t_e \ll (4.8(10^{-2}))^2/5(10^{-5})$$

or

$$t_e \ll 45.9 \text{ sec} \qquad (2.35)$$

It was shown above that $t_e \simeq .2$ sec which satisfies (2.35) and again the penetration theory may be used to evaluate the mass transfer coefficients, k_{Mn}^{2+}, k_{Fe}^{2+}

$$k_{Mn}^{2+} = 2(D/\pi t_e)^{1/2} = 2(5(10^{-5})/\pi \times .2)^{1/2}$$

$$\therefore \quad k_{Mn^{2+},FILM} = k_{Fe^{2+},FILM} = .018 \text{ cm sec}^{-1}$$

2.3.5 Mass Transfer at the Metal Pool/Slag Interface

The treatment of the mass transfer at this reaction site follows that of 2.3.4. Assuming again the slag circulation pattern of Figure 12, it is evident that flow may be considered to be a toroidal roll cell. The contact time of an element of slag with the metal pool is, therefore, the time taken to traverse a distance equal to the radius, i.e. 37 mm. At a velocity of 10 cm sec^{-1}, we have:

$$t_e = \frac{3.7}{10} = .37 \text{ sec} .$$

Since the hydrodynamic regime at the slag/metal pool interface is similar to that of the slag/electrode tip interface the mass transfer

film thickness is given by 2.34

$$\text{Hence,} \qquad L = 3.4(10^{-2})\, x^{1/2}$$

$$\text{If } x = 37 \text{ mm,} \qquad L = 6.6(10^{-2}) \text{ cm}$$

Recalling, again 2.27

$$t_e \ll L^2/D$$

$$\text{or} \quad t_e \ll (6.6(10^{-2})^2/5(10^{-5})$$

$$\ll 87.1 \text{ sec}$$

Since $t_e = .37$ sec, the inequality holds and we may once again use the penetration theory to calculate k_{Mn}^{2+}, k_{Fe}^{2+}.

$$k_{Mn}^{2+} = 2\left(\frac{D}{\pi\, t_e}\right) = 2\left(\frac{5\,(10^{-5})}{\pi\,(.37)}\right)^{1/2}$$

$$\therefore \quad k_{Mn^{2+},POOL} = k_{Fe^{2+},POOL} = .013 \text{ cm sec}^{-1}$$

The liquid metal pool of the ESR unit has been shown to be well stirred.[35] Etienne[5] has estimated that t_e for the metal side is about .5 secs. Flow velocities in the liquid metal pool are unknown but the condition of good mixing would suggest that the boundary layer is sufficiently thin to permit the use of the penetration theory for estimating k_{Mn}. Thus,

$$k_{Mn} = 2\left(\frac{D}{\pi\, t_e}\right)^{1/2}$$

$$= 2\left(\frac{10^{-4}}{\pi \times .5}\right)^{1/2}$$

$$\therefore \quad k_{Mn,POOL} = .016 \text{ cm sec}^{-1}$$

2.3.6 Mass Transfer at the Falling Drop/Slag Interface

There has been more speculation about the importance of droplet transfer related mass transfer than either of the other two interfaces [10,14,18,20,53,54]. It is generally agreed that the drop plays a very minor role in the overall mass transfer mechanism, but from a heat transfer point of view, it is undoubtedly of some significance.[55,56] There is some need, therefore, for critical examination of transport phenomena occurring during drop fall.

As a first approximation, the end effects of drop formation and subsequent coalescence will be ignored. This is not to say that these effects are not important but at present, there is insufficient information about drop formation and coalescence in ESR permit adequate analysis.

A number of comprehensive surveys of heat and mass transfer to drops have appeared in the literature.[57,58,59,60] There are a large number of correlations that have been used in a wide variety of liquid-liquid systems involving drops. The major theoretical basis for any correlation revolves around the hydrodynamic behaviour of the falling drop

and of the surrounding fluid. For the dispersed phase (drop) mass transfer these correlations may be subdivided into two categories; those based on the assumption of a rigid sphere and those assuming internal circulation within the falling drop. The rigid drop model may be discounted in the ESR case since it has been found to hold only in the case of very small drops.[57] Also it is quite likely that drops falling through the slag in the ESR process have a high degree of internal circulation caused by electromagnetic stirring.[9] In addition, one might expect the droplets to oscillate while falling. When a drop is forming and begins to neck it is subjected to a pinching effect[67] with the result that, when the droplet detaches, it is still elongated. The forces of surface tension acting on the drop will attempt to return it to its spherical equilibrium shape and hence set up an oscillation.[67] The magnitude of the oscillation is a function of drop size and interphase surface tension.

There have been relatively few accounts of dispersed drop phase mass transfer coefficients in the metallurgical literature.[18,62,68,74] For example, in spite of the abundance of work done on droplet/gas mass transfer by levitation melting[68,69,70,71] and in freefall situations[75] most of the experiments were set up so that condition of gaseous phase mass transfer prevailed. More of interest for present purposes, however, is the work concerning mass transport phenomena found in liquid metal drop-fused salt systems. This technology has received some attention of late due to its potential in recovering spent fuel from fast breeder nuclear reactors.[76,77] The result of this effort has led to some successful correlations for both internal (drop phase)[18,62,74,77] and

external (salt phase) mass transfer coefficients.[18,61,62,74,77]

Considering again the internal or dispersed phase coefficients, it has been found that the circulating drop model of Handlos and Baron[72] has satisfied the upper limit of internal mass transfer coefficient in each study.[18,62,74] However, these experiments were all conducted with relatively controlled drop formation and release characteristics compared to the situation prevailing in the ESR system. Drops observed in the above experiments rarely oscillate and the degree of internal turbulence is not great. Crimes[18] has, however, worked on systems in which the drops were observed to oscillate and in this case, a model proposed by Angelo et al.,[73] incorporating aspects of drop oscillation into the penetration theory, has proved to be satisfactory. In view of the expected similarity in behaviour of droplets in the electroslag process to the conditions described by the oscillating drop case, we shall use this model here.

It is suggested, therefore, that the value of $k_{Mn,DROP}$ may be predicted by the following relations.[73]

$$k_{Mn,DROP} = \left\{ \frac{4D\omega(1 + \varepsilon_0)}{\pi} \right\}^{1/2} \qquad (2.36)$$

where ω is the oscillation frequency (sec^{-1}) and ε_0 is an amplitude correction factor. Both ω and ε_0 are dependent on the amplitude of oscillation and can be related to the maximum and minimum drop diameter compared to a sphere of equivalent volume.[18]

Also,

$$\omega = \left(\frac{\sigma b}{d^3} \frac{192}{2\rho_m + 2\rho_s} \right) \qquad (2.37)$$

where

$$b = 1 - \frac{d_{max} - d_{min}}{2d_{SPHERE}} \tag{2.38}$$

d = diameter in cm.

and

$$\varepsilon_0 = \varepsilon + .375\ \varepsilon^2 \tag{2.40}$$

where

$$\varepsilon = \frac{A_{max} - A_{SPHERE}}{A_{SPHERE}}$$

A = area in cm^2

From Appendix I, it is seen that a typical drop weight calculated from the melt rate is about 2.5 gms. Taking a steel density of 7.2 gm cm^{-3}, the corresponding volume is 0.35 cm^3 and the drop diameter 8.8 mm.

Crimes[18] has developed an empirical technique for determining d_{max} and d_{min}. The ratio of these quantities is plotted versus b and ε in Figure 13[18] where this ratio is given empirically by

$$\frac{d_{max}}{d_{min}} = 2(d_{SPHERE}/.294)^{1/2} \tag{2.41}$$

If $d_{SPHERE} = .88$

$$d_{max}/d_{min} = 2\left(\frac{.88}{.294}\right)^{1/2} = 3.46$$

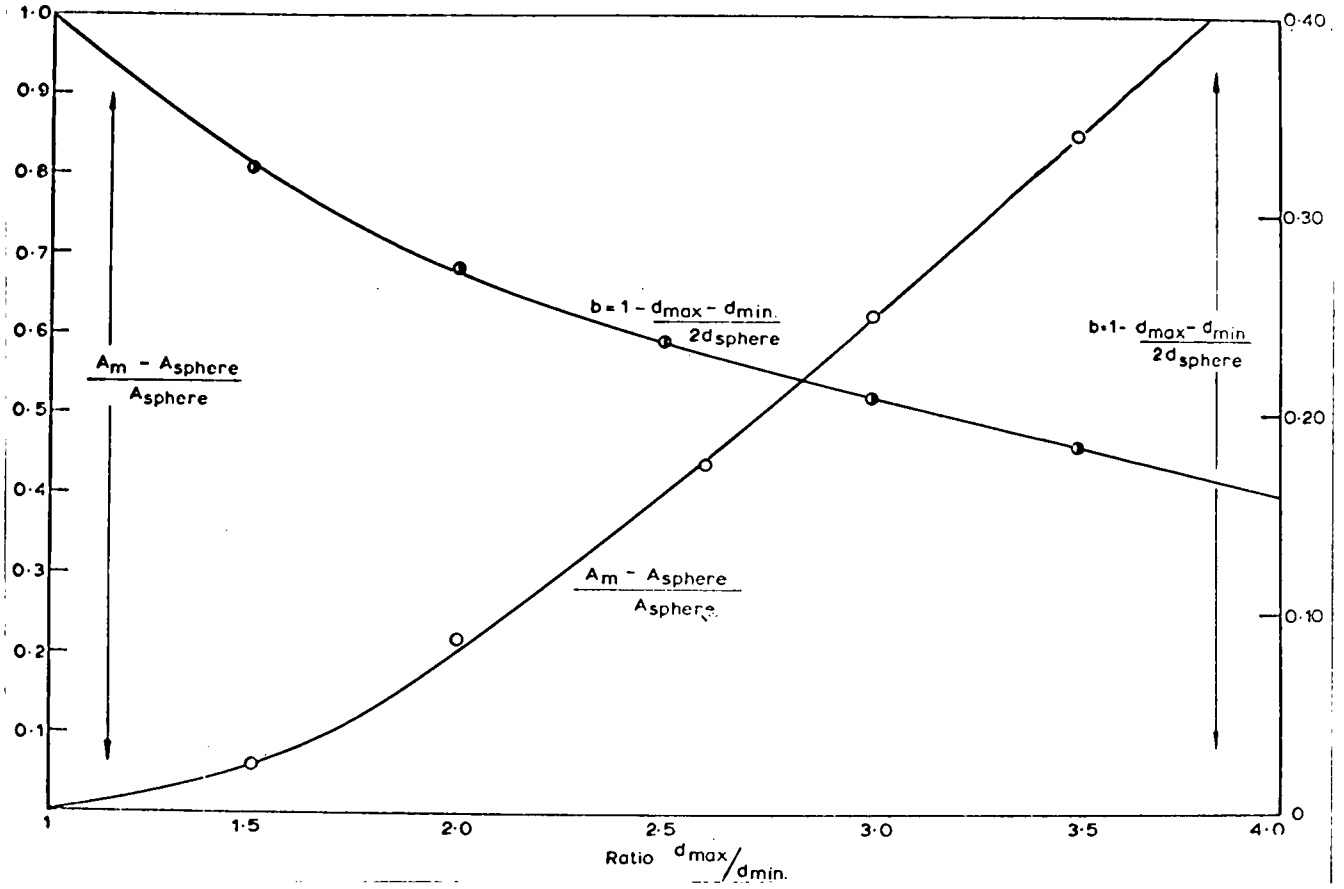

Figure 13 Surface Area and Amplitude Coefficient of Ellipsoid vs Ratio d_{max}/d_{min}

From Figure 13, $b \simeq .18$; $\varepsilon \simeq .82$

$$\therefore \quad \varepsilon_0 = .82 + .375(.82)^2 = 1.07$$

If the value of σ is set at 800 dyn cm^{-1}[18] and ρ_s and ρ_m have their usual values, then:

$$\omega = \left(\frac{800 \times .18 \times 192}{.88^3(3 \times 7.2 + 2 \times 2.6)} \right)^{1/2} = 40 \text{ sec}^{-1}$$

This value of 40 sec^{-1} is very reasonable and agrees with previously reported data on the oscillation frequencies of iron drops.[67] We are now able to evaluate, k_{Mn}; where $D_{Mn} = 10^{-4}$ cm^2 sec^{-1}.

$$k_{Mn} = \left(\frac{4(10^{-4}) \times 40 \times (1 + 1.07)}{\pi} \right)^{1/2}$$

$$k_{Mn,DROP} = .112 \text{ cm sec}^{-1}$$

There is, fortuitously, not the same lack of information about the continuous phase or external mass transfer coefficient. In almost every treatment of salt phase mass transfer resistance, a penetration theory-based model has been used with success.[61-64,76,77] The major change in the relationship, 2.26, where.

$$k_{Mn^{2+}} = 2 \times \pi^{-1/2} \left(\frac{D}{t_e}\right)^{1/2} \qquad (2.26)$$

has been to modify the const $2 \times \pi^{-1/2}$ to account for the effect of the wake behind the falling drop. In the wake region a lower rate of mass transfer will be observed since the surface concentration is not being renewed in the same fashion as in the forward section. The new coefficient, replacing $2 \times \pi^{-1/2}$ is given as .69[78] and thus

$$k_{Mn^{2+}} = .69 \left(\frac{D}{t_e} \right)^{1/2} \tag{2.42}$$

The time, t_e, is taken as the time for a drop to fall through a distance equal to its diameter. Equation 2.42 becomes

$$k_{Mn^{2+}} = .69 \left(\frac{uD}{\pi d} \right)^{1/2} \tag{2.43}$$

where u is the drop velocity.

Crimes[18] and Warren[74] have both found this relation to fit continuous phase mass transfer data.

We must use some method to estimate the velocity of the drop in order to use Equation 2.43. Hu and Kintner[79] have developed a generalized and widely used[18,74,59] correlation for the velocity of falling drops. The generality of this correlation stems from the fact that it is based exclusively on the physical properties of the system. Using dimensional analysis arguments, they were able to establish that the essential dimensionless groups for the correlation were the Reynolds number, Re, the Weber number, We, and a physical properties group, P, (inverse Morton number) defined as

$$P = \frac{\rho_c^2 \ \sigma^3}{g(\rho_d - \rho_c) \ \mu_c^4} \tag{2.44}$$

where the subscript c defines a continuous phase property and the subscript, d, a dispersed phase property. It was found that the plotting of

$$X = .75 + \frac{Re_c}{P^{0.15}} \tag{2.45}$$

$$\text{vs.} \quad Y = \frac{4d^2 g(\rho_d - \rho_c) \ P^{0.15}}{3 \ \sigma} \tag{2.46}$$

on logarithmic coordinates correlated the drop velocity rate for a great quantity of data taken from a number of systems. From curve fitting, Hu and Kintner present the following equations:

$$\begin{aligned} Y &= \frac{4}{3} \ X^{1.275} \qquad 2 < Y \leq 70 \\ Y &= 0.045 \ X^{2.37} \qquad Y \geq 70 \end{aligned} \tag{2.47}$$

Evaluating P, using the appropriate data (2.34)

$$P = \frac{(2.6)^2 \ (800)^3}{980 \times 4.6 \times (.75)^4}$$

$$= 2.43 \ (10^6)$$

From this characteristic value of P, we can calculate Y, from 2.46;

$$\text{i.e.} \quad Y = \frac{4\,(.88)^2\ 980\ (4.6)\ (2.43\ (10^6))^{.15}}{3 \times 800}$$

$$= 52.79$$

From the first of the relations, 2.47;

$$Y = \frac{4}{3}\ X^{1.275}$$

$$\therefore \quad X^{1.275} = \frac{52.79 \times 3}{4} = 39.59$$

$$X = 17.91$$

But from (2.45), $X = .75 + Re\ P^{-.15}$

$$17.16 = \frac{du\rho_c}{\mu_c}\ \frac{1}{(2.43(10^6))^{.15}}$$

$$u = 17.16 \times .75 \times (2.43(10^6))^{.15} / (.88 \times 2.6) = 51 \text{ cm sec}^{-1}$$

This value of u is the terminal velocity of the drop. A drop falling in the ESR slag bath starts, obviously, from a rest position accelerating until it reaches its maximum speed. For the purposes of calculating the mass transfer coefficient, it will be assumed the $u = u_{max}$.

This velocity will result in an overestimate of $k_{Mn^{2+}}$, but the consequences are small as will be discussed later. If we include also the velocity added to the drop by bulk motion of the slag ($\simeq$10 cm sec^{-1}) in the direction of fall, u becomes 61 cm sec^{-1}

$$k_{Mn^{2+},DROP} = .69 \left(\frac{61(5 \times 10^{-5})}{\pi \times .88} \right)^{1/2}$$

$$\therefore \quad k_{Mn^{2+},DROP} = k_{Fe^{2+},DROP} = .023 \text{ cm sec}^{-1}$$

Although we have used the terminal velocity in this calculation, the actual drop fall contact time was determined considering the acceleration of the drop. (2.5.1).

We have now estimated all nine mass transfer coefficients needed for the model calculations and these are summarized in Table I. Before the model can be used, we must also estimate the area to volume ratios at the three mass transfer interfaces.

2.4 Area/Volume Ratio Estimates

During the experimental program, as much care as possible was taken to run each melt under the same conditions. As a consequence of this, the area/volume ratios of the film, drop and pool remained approximately constant, allowing us to calculate an average value for each site.

2.4.1 Area/Volume Ratio of Drop

In 2.3.6, the average drop volume was found to be .35 cm^3. To estimate the area of an oscillating drop we must use the formula[18]

$$A_{max} = \frac{\pi d_{max}^2}{2} + \frac{\pi d_{max} d_{min} \ln(\varepsilon_0 + (\varepsilon_0 - 1)^{1/2})}{2(\varepsilon_0^2 - 1)^{1/2}} \qquad (2.48)$$

In 2.3.6, ε was found to be 1.07 but we must calculate d_{max}, d_{min} from 2.38. Recalling 2.48

$$b = 1 - \frac{d_{max} - d_{min}}{2d_{SPHERE}}$$

$$2d(1-1) = -d_{max} + d_{min}$$

but from 2.41

$$\frac{d_{max}}{d_{min}} = 3.46$$

if $d = .88$ and $b = .18$, then

$$1.76 \times (-.82) = -3.46\, d_{min} + d_{min}$$

$$d_{min} = \frac{-1.44}{-2.46} = .59 \text{ cm} .$$

$$d_{max} = 2.04 \text{ cm} .$$

Now, from 2.48

$$A_{DROP} = \frac{\pi(2.04)^2}{2} + \frac{\pi(2.04)(.59)\ln(1.07 + \sqrt{(1.07)^2-1}}{2\sqrt{(1.07)^2 - 1}}$$

$$= 8.38 \text{ cm}^2$$

$\therefore$ Area/volume ratio of drop = 8.38/.35 = 24.0 cm^{-1}

2.4.2 Area/Volume Ratio of Film

Since the electrode tip can be considered to be a cone (2.3.4), the area and volume calculations are greatly simplified. If the average film thickness is taken as 100μ and the cone angle as 45°, the surface area for a 38 mm ϕ electrode tip is given by

$$A_{FILM} = \frac{\pi r^2}{\cos\theta} = \frac{\pi(1.924)^2}{.707} = 16.45 \qquad (2.49)$$

where

r = R + radial component of film

= R + (.01/cos 45) = 1.924

The volume of a cone is

$$V_{CONE} = \frac{1}{3}\pi r^2 h \qquad (2.50)$$

The film volume is taken to be the difference between a cone of 1.91 cm radius and that of 1.92 cm radius. Since θ = 45° h = r. Therefore,

$$V_{FILM} = \frac{\pi}{3}(1.924^3 - 1.91^3)$$

$$= .16 \text{ cm}^3$$

$\therefore$ the area/volume ratio of the film $= \frac{16.45}{.16} = 102.8 \text{ cm}^{-1}$

2.4.3 Area/Volume Ratio of Pool

In the ingots produced during the melt program, the ingot pool was generally observed to be virtually cylindrical, i.e. with a flat top and bottom. The area/volume ratio is given, then, as.

$$\left(\frac{A}{V}\right)_{POOL} = \frac{\pi r^2}{\pi r^2 h} = \frac{1}{h} \qquad (2.51)$$

The approximate average depth of the pool was 15 mm and thus

$$\left(\frac{A}{V}\right)_{POOL} = 1/1.5 = .67 \text{ cm}^{-1}$$

If the average slag skin thickness is equal to 1 mm. then,

$$\text{the pool volume} = \pi \times (3.81 - .1)^2 \times 1.5$$

$$= 65 \text{ cm}^3$$

The above information is included in the summary of Table I.

TABLE 1

Summary of Theoretical Mass Transfer Coefficients, Average Area/Volume Ratios and Approximate Residence Times for 76 mm ϕ ESR Furnace

Location / Parameter	Film Reaction Site	DROP Reaction Site	Pool Reaction Site
k_{Mn} $(cm.sec.^{-1})$	0.012	0.112	0.016
$k_{Mn^{2+}}$ $(cm.sec.^{-1})$	0.018	0.023	0.013
$k_{Fe^{2+}}$ $(cm.sec.^{-1})$	0.018	0.023	0.013
A/V (cm^{-1})	103.	24.	.67
Residence Time (Sec)	.95	.12	80*

*Residence time in pool $\simeq$ (rate of rise of ingot x pool depth)$^{-1}$
From Appendix I - rate of rise of ingot = $\dot{W}_m / \pi r^2$. For a pool depth of 1.5 cm and a volumetric melt rate of 0.36 cm^3 sec^{-1}
t_e in pool $= \left(\frac{0.36 \times 1.5}{\pi(3.81)^2}\right)^{-1} = 80$ sec

2.5 Numerical Solution of Differential Equations for Mass Transfer

The differential Equation 2.14, may now be evaluated subject to boundary conditions which must be determined experimentally. The equation,

$$\frac{d[Mn]}{dt} = -\frac{A}{V} k_{Mn} \{ [Mn]_b - [\frac{b \pm (b^2 + 4c)^{1/2}}{2}] \} \qquad (2.14)$$

is applied to each reaction site in the following manner. Numerical solution of this non linear, first-order differential equation was accomplished using a 3^{rd} order Runge-Kutta technique. The details of this numerical method are found in numerical analysis texts, (for example, Lapidus, "Digital Computation for Chemical Engineers"[80]) and will not be discussed here. The programming details are presented in Appendix IV, and the general method is outlined as follows.

Calculations were carried out simultaneously at the film and pool sites for the period of drop formation, and then for the duration of the drop fall. The experimentally obtained frequency of drop production determined the interval of drop formation, this time being divided into 10 smaller increments for the purposes of accuracy. The step frequency for the Runge-Kutta routine was of the order of .1 sec for a drop frequency of 1 sec. This was adjusted for each run according to the measured frequency. The interval size of .1 sec was found to be sufficiently low to produce an accurate result, without excessive expense. Since the drop fall time (see 2.5.1) is only slightly greater than .1 sec, the step size was, of necessity, much shorter during this period; $\simeq$ .01 sec.

In addition to the numerical solution of 2.14 at the 3 sites it was necessary to keep strict account of the number of moles transferred to and from the various interfaces. This was accomplished through the use of 2.15 at the end of each subinterval:

$$\Delta(Mn^{2+})_b = -\Delta(Fe^{2+})_b = -\Delta[Mn]_b \left(\frac{V_m}{V_s}\right) \qquad (2.15)$$

Hence, a continuous composition vs time profile of slag and ingot concentrations was obtained. The results of these modelled profiles were compared to the appropriate experimental profiles (Chapter 4).

2.5.1 Estimation of Drop Fall Time

So far, we have not discussed how the drop fall time was estimated. The procedure is taken from Lamb's book on Hydrodynamics[81] and is based on a consideration of a spherical droplet falling under the influence of gravity at steady state, such that the gravitational force is exactly balanced by the drag resistance of the surrounding fluid. The solution is given as:

$$S = \alpha \ln \cosh \left(\frac{U_0 t}{\alpha}\right) \qquad (2.52)$$

$$U = U_0 \tanh \left(\frac{U_0 t}{\alpha}\right) \qquad (2.53)$$

where S is the distance fallen during acceleration period, t, to reach terminal velocity, U_0; u is the velocity during acceleration and

$$\alpha = \frac{2}{3}\frac{d}{C_D}\left(\frac{2\rho_d + \rho_c}{\rho_c}\right) \tag{2.53}$$

where C_D is the drag coefficient such that

$$C_D = \frac{4}{3}\frac{\Delta\rho}{\rho}\frac{dg}{U_0^2} \tag{2.54}$$

if $\rho_c = 2.6$, $\rho_d = 7.2$, then α reduces to

$$\alpha = \frac{2\rho_d + \rho_c}{2g\ \Delta\rho}\ U_0^2$$

$$= \frac{2(7.2) + 2.6}{2 \times 980 \times 4.6}\ U_0^2$$

$$= 1.97\ (10^{-3})\ U_0^2$$

The slag bath in the 76 mm ϕ ESR furnace is approximately 4.5 cm deep. From 2.52, setting U_0 = 51 cm/sec (2.3.6)

$$4.5 = 1.97\ (10^{-3})(51)^2\ \ln\ \cosh\ \left(\frac{51\ t}{1.97(10^{-3})(51)^2}\right.$$

$$\therefore\quad \cosh\ \left(\frac{t}{1.97(10^{-3})(51)}\right) = \exp\ \left(\frac{4.5}{1.97(10^{-3})(51)^2}\right)$$

$$t = .10\ \cosh^{-1}\ \{\exp\ [8.78(10^{-1})]\ \}$$

$$= .1 \times 1.52 \text{ sec}$$

$\therefore$ Time to fall 4.5 cm during acceleration period = .15 sec.

The velocity at this time is, from 2.53

$$u = U_0 \tanh \left(\frac{U_0 t}{\alpha} \right)$$

$$= 51 \tanh \left(\frac{.15}{.1} \right)$$

$$= 46.3 \text{ sec}^{-1}$$

The drop would appear to be accelerating throughout its fall through the slag. The bulk slag motion would add another 10 cm/sec to the initial velocity and reduce the overall contact time by about 20%. Therefore the drop fall time is of the order of .2 sec. This time has been estimated by others working in ESR[18,54] to be approximately 0.1 sec so this value is not unreasonable.

2.6 Summary

A mathematical mass transfer model has been developed to describe the kinetics of manganese oxidation by FeO under controlled conditions in electroslag remelting. The essential parameters have been identified and evaluated by various means, ranging from experimental observations to established theories for mass transfer coefficients. However, in order to validate the model, it is necessary to compare the results to actual experimental conditions. The experimental program designed for this purpose is developed in Chapter 3 and the resultant data compared to the mass transfer model in Chapter 4.

CHAPTER 3

EXPERIMENTAL PROGRAM

3.1 The U.B.C. Electroslag Furnace

The experimental program designed to test the mass transfer model developed in Chapter 2 was carried out on the U.B.C electroslag unit. The design of this unit is specifically adapted to the requirements of a range of research projects and has been described in detail by Etienne.[5] The particular configuration used throughout this work employed a short 3" ϕ mold capable of making ingots 9" long over a period of approximately 1300 seconds.

3.2 Slag Sampling Device

In order to follow the progress of mass transfer as accurately as possible, it was necessary to take a number of slag samples during the course of a run. The majority of experiments were conducted under an inert atmosphere and the more common techniques of slag sampling (such as dipping a copper rod into the slag bath) proved to be impractical. Investigations were then carried out on a novel method for collecting slag samples with the following result.

It was discovered, in a series of trials, that a quantity of slag suitable for chemical analysis could be obtained by dipping a helical coil of Mo wire into a CaF_2-based fused salt. Samples weighing from 100 - 600 mg were collected in 1" long coils wound from .020" ϕ

Mo wire on a .125" ϕ rod using 22 turns to the inch. This technique was then incorporated into a device for use on the ESR furnace. The resulting piece of equipment is shown in Figure 14.

Besides being used for sampling, this unit also provided an integral part of the inert gas closure. Basically, it consisted of a stainless steel tube 2 3/8" OD and 17" high. On top and bottom were flanges of stainless steel and colorlith, respectively. 1" colorlith was used to electrically insulate the gas cap from the mold. In this bottom flange, 18 stainless steel guide tubes were press fit into holes drilled as closely as possible to the inner edge. Steel wires of $\simeq$.1" ϕ, and stiffened by swaging, were inserted into these guide tubes and the Mo sampling coils were then attached to the bottom ends. To ensure gas tightness, small rubber stoppers with small holes in the centres were placed on top of the guide tubes. Since the gas cap as a whole became very hot during a melt, it was necessary to place a few turns of 1/8" ϕ copper tubing for water cooling purposes at the level of these stoppers.

Once the Mo samplers had been attached to this unit, it was placed on top of the mold, clamped into place and a 6" ϕ neoprene rubber bellows clamped onto the top flange (Figure 15). The top of the bellows was subsequently secured to the water cooled electrode holder. Inert gas was flushed through the system, entering the gas inlet pipe in the gas cap and leaving through an outlet at the top of the bellows.

The gas cap sampling unit was also fitted with explosion windows covered with aluminium foil and silicone rubber sealant. Included also was a port which was sealed with a rubber stopper and

Figure 14 Gas Cap and Sampling Unit Used in Experimental Program

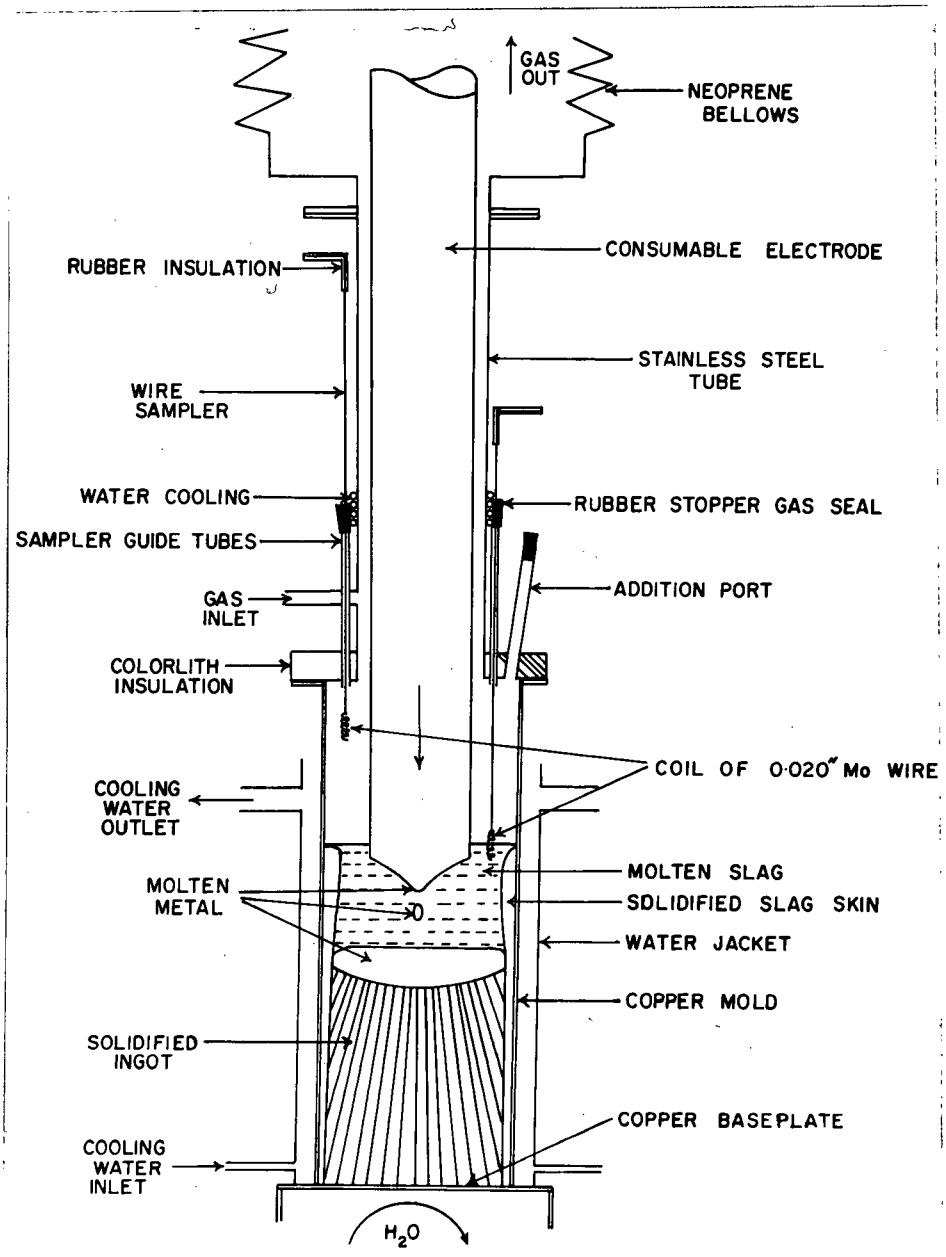

Figure 15 Schematic Diagram Depicting ESR Configuration Designed for Slag Sampling under Inert Atmosphere

through which various materials could be dropped into the slag.

In order to facilitate sample taking an AC voltmeter was hooked up so that when the Mo wire touched the surface of the slag, a voltage reading appeared on the instrument dial. The sampler was then pushed deeper into the slag and removed at once. To enable a precise timing of these samples, the voltage was recorded on a chart recorder with a chart speed of 1" per min and hence an accurate record of the time of each sample was obtained.

Once all the samples had been obtained and the melt concluded, the unit was removed and the Mo wires cut off. The slag contained in each of these coils was collected, separately labelled and stored for chemical analysis.

It is worth noting that although this technique has been successfully used to sample the liquid metal in the ingot pool, the failure rate is high. Also, simultaneous slag and metal sampling operations are not compatible unless very long coils are used.

3.3 Materials

3.3.1 Electrode Material

In mass transfer experiments it is desirable to control as many variables as possible. With this in mind, the system that was chosen for this study was the oxidative loss of Mn from mild steel, namely C1018 in 1 1/2" ϕ bar form. The nominal analysis of 1018 is:

C	Mn	P	S
.15 - .2	.6 - .9	.04	.05

In order, however, to ensure that Mn was the only reacting species given the anticipated slag FeO level of ≃.5%, the exact concentrations of manganese and silicon must be known. These varied from .61% to .79% for Mn and averaged .1% for Si without much deviation in the latter case. This relatively low concentration of Si as well as the small value of γ°_{Si} (where log γ°_{Si} = 1.21 - 6100/T (°K))[32] results in an extremely low activity of Si in the metal relative to Mn. Although the activity of SiO_2 in the slag was also very low[83] and that of MnO very high,[37] one can show (Appendix V.1) that even with the lowest observed levels of Mn, it will be the manganese that is preferentially oxidized. This would indicate that 1018 is a suitable steel for study of manganese mass transfer.

3.3.2 Armco Iron Electrodes

1 1/4" ϕ Armco iron was used as a relatively pure iron in experiments to determine mass transfer coefficients at the molten slag/ingot pool interface. Of particular note are the low Mn and low S concentrations. The overall assay in the as-received condition was:

C	Mn	P	S	Si	O	Fe
.012	.017	.005	.025	trace	.070	bal.

3.3.3 Slag Materials

The majority of melts were performed using CaF_2-20% CaO slags. This slag was chosen for several important reasons. Firstly, the CaF_2-20% CaO slags permitted stable and reasonably reproducible melting

conditions from run to run -- a necessary prerequisite for adequate control over the experimental conditions. Also, these slags dissolve readily in hot HCl after suitable crushing, in contrast to CaF_2-based slags with an equivalent percentage of Al_2O_3. These latter slags require prefusing in platinum crucibles with sodium borate and subsequent dissolution in aqua-regia. This procedure is very time consuming and extremely hard on the platinum crucibles.

The final, but most important reason concerns the appropriate thermochemical information. Of interest here are the ternary systems CaF_2 - CaO - FeO,[27,30,36] CaF_2 - CaO - MnO[30,37] and CaF_2 - CaO - CaS.[17,30,84] Fortunately, the thermochemistry of these systems has been investigated sufficiently to be of use in determining the necessary activity values required by the mass transfer model. Very little work has been published on any other CaF_2-based systems.

The calcium fluoride used in these experiments was obtained from Eldorado Nuclear and is a high purity by-product of the production of zirconium. The majority impurity is therefore zirconium as zirconium fluoride which is quickly removed from the slag in the start-up operations in the ESR unit. Very trivial amounts (up to 10 ppm) of Fe, Mn were found to be present in this material.

Recrystallized calcium oxide of 99.5% purity was used to make the balance of the starting slag. This was supplied by Dynamit-Nobel, Germany.

3.4 Atmosphere Control

As described in 3.2, a system of neoprene rubber bellows and a gas cap provided the inert gas enclosure. The inert gas used in these experiments was helium of normal commercial quality. At a flow rate of 4 ℓ min^{-1}, the system could be flushed out in approximately 30 minutes. Checks were made on the outlet gas using a gas chromatograph and only traces of O_2 were detected on the highest sensitivity after one half hour.

3.5 Melting Conditions

For the most part, ingots produced in the melt program were made under stable melting conditions which were approximately reproducible from run to run. Each melt was begun using the DC power supply with electrode negative and then switched to AC when stable melting conditions had been achieved.

In several cases, ingots were made using a "live" mold. This was done by connecting a separate lead directly to the bottom of the mold, thereby making it a parallel electrical path to the normal ingot and base plate route. This configuration permitted measurement to be made of the proportion of current flowing through the mold relative to that passing through the ingot.

A few runs were made in which the mold was completely insulated from electrical flow. This was accomplished by painting the interior surface of the mold with 2 coats of boron nitride paint. The type of BN used was Type A, supplied by Carborundum. Since BN is an excellent thermal conductor (approximately equivalent to Fe) as well as an excellent insulator, it proved to be the ideal material for this application.

3.6 Melt Records

During the melting of an ingot, detailed accounts were kept of all the important operating parameters. A Sargent Model SR Millivolt recorder was used to keep a continuous record of operating current. Once the electrode was melting in a stable fashion (i.e. when the slag was completely molten), the following data were recorded at suitable intervals:

Volts	=	process voltage
Amps	=	process current
t	=	time in seconds from some fixed starting point
P	=	total electrode travel in mm from beginning of melt
MS	=	speed of electrode travel drive motor
ΔT	=	temperature difference in °C between inlet and outlet mold cooling water.

In addition, the time and electrode position were recorded whenever a slag sample was taken. Certain other data were collected after the melt had been made and the ingot stripped from the mold. These were slag cap height and weight and the average slag skin thickness.

From these parameters, all of which are not useful for any given run, such information as average melt rate, drop size and rate of slag loss may be routinely calculated (cf. Appendix I).

3.7 Slag and Metal Analysis

Once the slag samples had been removed from the Mo sampler coils, they were separately crushed to a fine powder with mortar and

pestle, weighed and dissolved in hot 50% HCl solution. These solutions were subsequently made up to a standard volume of 100 ml with distilled water. Aliquots of these solutions were then taken and analyzed for manganese and iron according to the procedures outlined in Appendix II. In cases where sulphur analyses of the slag samples were required, a small portion of the powdered slag was analyzed immediately after crushing, using a semiautomatic "Leco" sulphur analyzer.

Wet chemical analysis techniques were used throughout for slag analysis in preference, say, to x-ray fluorescence or atomic absorption methods since it was desired to measure small differences in the low levels of Mn and Fe (occasionally as low as several parts per million in the sample solution). It was felt that the techniques used, namely, the permanganate method for Mn and the orthophenanthroline method for Fe, were best suited for these analyses in terms of accuracy, reproducibility and freedom from interference by other ions.

The maximum relative uncertainty of individual analyses may be estimated as ± 5%. In many cases this is an overestimate of the error, but, due to the nonlinear nature of the Beckman "B" spectrophotometer absorbance scale, the error associated with reading low absorbance levels is assumed. Other sources of error are primarily due to inaccuracies in measuring solution quantities during analysis but these tend to be systematic errors (i.e. consistently high or low) of small importance and are hence ignored.

In order to draw error bars about the data points a value of 5% of .5 wt % or ± .025 wt % has been used. This will roughly accommodate the probability of larger relative error at lower concentrations of the measured quantities.

All ingot metal analysis was done by spark spectrographic equipment (Baird-Atomic Spectromet Model HA3). In addition, only the ingot centreline was analyzed, usually at intervals of 1/4". This spacing was then converted to a time interval through knowledge of the average melt rate. Manganese and silicon levels could be measured to within ± .01 wt % using this equipment. It should be noted that all ingot analysis was done as close to the centre as possible.

3.8 Melt Program

3.8.1 General Comments

The major purpose of the experimental program was to provide detailed information for the testing of the mass transfer model. Part of the experimental data, such as melt rates, slag cap data, etc., were used directly as input parameters for the computer program. Other input to the model involved establishing the initial conditions with respect to iron and manganese levels at some arbitrary time, t = 0. It often happened that several samples were taken during a run before a particular set of experimental conditions were achieved. Since these samples represented no useful data and bore no relevance to the work at hand, they will not be shown here.

The melt program and resultant data are given below.

3.8.2 Experimental Determination of Mass Transfer Coefficients

In Chapter 2, a number of mass transfer coefficients were evaluated by largely theoretical means. Due to the number of parameters

involved in the mass transfer model of Chapter 2, it is necessary to verify, independently, as many of these values as possible. We have already used measured quantities to calculate the various area/volume ratios, but experimental assessment of the mass transfer coefficients would allow us to place more or less faith in the modelled estimates of Chapter 2.

Initially, we can ignore the possibility of measuring mass transfer coefficients involving the drop reaction site since it is virtually impossible to sample the drops or to observe their behaviour. In addition, the modelling attempts of Etienne[5] have resulted in a reasonable degree of confidence in the film mass transfer coefficients and so we are left with the determination of the pool coefficients.

There are several techniques possible here. Initially, the use of radioactive tracers was considered. This would involve adding radioactive Mn (Mn^{55}) to the metal pool and then analyzing the slag samples on a scintillation counter. There are a number of difficulties with this idea, not the least of which is that Mn^{55} has a halflife of only 2.57 hrs. In any case, what proved to be a most satisfactory and unambiguous technique was developed as an alternative.

The basic idea of this alternate method was to melt relatively pure iron (Armco iron) through the CaF_2 - CaO slag in the ESR furnace and then to dope the metal pool with a certain amount of manganese metal. The samples taken within a short period of time after the doping would contain MnO that came from the pool alone and hence might provide some information about mass transfer coefficients involving transport to and/or from the interface. In fact, the quantity of Mn (Granular +325

mesh 99.99+, supplied by Research Organic/Inorganic Chemical Corporation) added was sufficient to eliminate most resistance to metal phase transport control (see Chapter 4) and allow calculation to be made of $k_{Mn^{2+},POOL}$, $k_{Fe^{2+},POOL}$.

This experiment was repeated twice with 4 and 12 gms of Mn being dropped into the pool in a small copper foil pouch (to prevent contamination of the slag). The foil pouch also contained a small amount of tungsten powder to mark the pool profile in the ingot. Samples were taken as quickly as possible after the addition of Mn. The data from these two experiments (60, 61 respectively) are given in Table II.

Also of interest was the determination of the sulphur mass transfer coefficient at the metal pool/slag interface. An identical experiment to those of 60, 61 was performed but the Mn in the foil pouch was replaced by 4 gm of FeS (technical grade). The results of the slag sample analyses from Run #62 are given in Table II.

3.8.3 Steady State

Runs 27 and 53 were done in order to establish the extent to which chemical changes might occur during normal ESR processing of 1018 using a CaF_2 - 20% CaO slag. The system was allowed to establish its steady state behaviours over as long a period as possible. The operating parameters and the results of slag and ingot analysis are given in Table III.

Run #	Average Volts	Average Runs Amps	ΔT(°C)	Slag Skin Thickness (mm)	Average Melt Rate (g sec^{-1})	Final Slag Weight (g)
60 (Armco)	23.5	1200	16.5	.9	2.5	600
61 (Armco)	23.5	1250	17	.6	2.5	590
62 (Armco)	23.2	1250	16	.8	2.8	520

TABLE II-a OPERATING PARAMETERS

Run #	Time of Sampling (sec)	Wt % Fe^{2+}	Wt % Mn^{2+}
60	304	.32	.08
(4 gm Mn added	333	.39	.12
to pool at	341	.35	.14
~ 300 sec)	349	.34	.15
61	157	.52	.18
(12 gm Mn added	166	.53	.20
to pool at	174	.54	.21
~ 150 sec)	182	.55	.23
	193	.54	.24
			Wt % S
62	120	-	.08
(FES added	146	.40	.25
to pool at	152	.43	.28
~ 130 sec)	159	.45	.30
	166	.46	.33
	174	.48	.34
	300	-	.35

TABLE II-b SLAG ANALYSES - RUNS # 60, 61, 62

Run #	Average Volts	Average Rms Amps	ΔT(°C)	Slag Skin Thickness (mm)	Average Melt Rate (gm sec^{-1})	Final Slag Weight (g)
27 (1018)	22.5	1175	15	-	2.6	-
53 (1018)	23.2	1225	17.5	.8	2.7	540

TABLE III - a OPERATING PARAMETERS

Time of Sampling (sec)	Wt % Fe^{2+}	Wt % Mn^{2+}
165	.34	.20
214	.35	.26
291	.35	.27
400	.38	.26
468	.41	.27
559	.41	.30
648	.41	.31
706	.43	.29
774	.43	.32
844	.45	.31
904	.46	.32
980	.46	.33
1024	.48	.36
1083	.48	.33
1146	.48	.34
1230	.49	.38
1273	.50	.33

III - b SLAG ANALYSIS - RUN # 27
(1018 Electrode - .75 % Mn)

Time of Sampling (sec)	Wt % Fe^{2+}	Wt % Mn^{2+}
191	.34	.28
304	.35	.33
388	.37	.32
432	.43	.31
497	.40	.32
568	.40	.35
723	.42	.34
798	.44	.36
881	.46	.39
943	.48	.39
1034	.51	.40
1096	.50	.43

III - c SLAG ANALYSIS - RUN # 53
(1018 Electrode - .61% Mn)

Time After Deoxidizing (sec)	Wt % Mn
118	.601
216	.592
334	.598
492	.572
531	.563
590	.570
755	.559
807	.569
866	.580
1004	.574

TABLE III - d

INGOT ANALYSIS - RUN # 53

3.8.4 Unsteady State Recovery

It is evident, from an examination of the slag and ingot concentration histories during a normal melt, that the composition changes are small. In order to try and produce larger changes in composition, it was decided to deoxidize the slag at some point after stable conditions had been achieved when melting in the AC mode. The result of such an operation would be expected to produce a perturbation in slag composition followed by a period of transient behaviour as the system returned to steady state.

The procedure for deoxidizing the slag was very simple. First, a small quantity of tungsten powder (3-5 g) was added to indicate the position of the freezing interface at a precise time. This was immediately followed by the addition of calcium metal shot (< 1/4" ϕ). After a short period of time sampling was started and continued at various time intervals until the conclusion of the melt.

A number of melts (30, 31, 34, 37, 42) were carried out in this fashion and the results are presented in Table IV.

3.8.5 Live Mold

It has previously been reported that the mold may form part of the current path during AC electroslag remelting.[2,85] This observation is probably the result of mold-ingot contact at regions where the slag skin is imperfect, particularly when cold slag starts are used, as in small ESR units. However, it is virtually impossible to measure current flow through the mold during normal AC remelting due to the

Run #	Average Volts	Average Rms Amps	ΔT(°C)	Slag Skin Thickness (mm)	Average Melt Rate (gm sec^{-1})	Final Slag Weight (g)
30 (1018)	23	1100	14.5	2.	2.6	480
31 (1018)	22.5	1200	14.5	2.	2.7	530
34 (1018)	23	1175	17.	-	2.7	510
37 (1018)	22	1175	16.5	1.	2.5	470
42 (1018)	22.5	1350	19.	1.7	3.0	500

TABLE IV - a OPERATING PARAMETERS

Run #	Time of Sampling (sec)	Wt % Fe^{2+}	Wt % Mn^{2+}
30 Deoxidized at 250 sec	280	.11	.07
	320	.18	.08
	348	.28	.10
	368	.36	.11
	400	.40	.09
	469	.37	.14
	498	.37	.17
	537	.41	.19
	617	.39	.20
31 Deoxidized at 320 sec	350	.11	.06
	375	.15	.08
	413	.24	.06
	454	.37	.12
	495	.42	.11

TABLE IV - b SLAG ANALYSIS - RUNS # 30, 31
(1018 Electrodes - .75% Mn)

Time of Sampling (sec)	Wt % Fe^{2+}	Wt % Mn^{2+}
326	.24	.13
359	.44	.16
384	.63	.12
448	.68	.18
477	.62	.16
515	.53	.20
559	.55	.20
625	.47	.16
669	.43	.21
772	.37	.17
829	.35	.21
891	.34	.25
954	.35	.29
1025	.38	.27
1102	.38	.30
1201	.41	.31
1286	.43	.29

TABLE IV - c SLAG ANALYSIS

RUN # 34

(1018 Electrode - .68% Mn; Deoxidized at 300 sec)

Time of Sampling (sec)	Wt % Fe^{2+}	Wt % Mn^{2+}
55	.17	.09
96	.29	.06
115	.32	.09
141	.38	.11
172	.48	.12
208	.57	.14
259	.73	.18
304	.92	.16
356	.87	.19
441	.78	.20
508	.75	.23
611	.69	.22
698	.60	.27
792	.60	.27
908	.47	.30
1003	.40	.32
1103	.38	.33
1244	.36	.29

TABLE IV - d SLAG ANALYSIS

RUN # 37

(1018 Electrode - .79% Mn; Deoxidized at 0. sec)

Time of Sampling (sec)	Wt % Fe^{2+}	Wt % Mn^{2+}
319	.18	0.04
405	.21	.05
455	.24	.07
522	.31	.10
570	.33	.10
632	.41	.14
705	.52	.18
817	.42	.24
942	.39	.29
992	.35	.30

TABLE IV - e SLAG ANALYSIS

RUN # 42

(1018 Electrode - .70% Mn)

Time After Deoxidizing (sec)	Wt % Mn
0	.669
62	.673
275	.626
330	.610
378	.594
446	.593
590	.574
673	.599
741	.595

TABLE IV - f INGOT ANALYSIS

RUN # 42

small potential drop along the copper mold. Nevertheless, it is quite feasible to deliberately pass current through the mold as described in 3.5. Once this electrical circuit has been set up, current may be measured in the usual fashion by means of a calibrated shunt. In this way then, the passage of current through the mold during normal AC melting is simulated.

In Run #47, the same procedure was used as described in 3.8.4, the only change being the use of the live mold circuitry. The results are tabulated in Table V. In addition, the mold current and voltage were monitored on a Tektronic Type 564 storage oscilloscope.

In order to determine the consequences on slag composition of using live mold on AC when no chemical reactions were involved, melt #59 was undertaken using Armco iron in place of 1018. The data obtained are presented in Table V.

In addition, several slag samples from the live mold runs were examined for Fe^{3+}. The analytical procedure is given in Appendix II. Essentially, the approach taken was to analyse for Fe^{3+} and then to compare this analysis to the total iron obtained by the alternate method.

3.8.6 Insulated Mold

In conjunction with the tests on live mold behaviour, the effects of completely insulating the mold were also investigated. The mold insulation was accomplished by the boron nitride coating procedure outlined in 3.5. It is worth noting that this BN paint, when properly

Run #	Average Volts	Average Rms Amps	$\Delta T(^{\circ}C)$	Slag Skin Thickness (mm)	Average Melt Rate (g sec^{-1})	Final Slag Weight (g)
47 (1018)	-	1500	21	1.2	2.6	510
59 (Armco)	23.5	1200	18	.9	2.7	530

TABLE V - a OPERATING PARAMETERS

Time of Sampling (sec)	Wt % Fe^{2+}	Wt % Mn^{2+}
347	.14	.05
360	.13	.06
387	.18	.05
402	.20	.04
423	.22	.07
462	.28	.07
521	.33	.10
552	.35	.12
599	.43	.13
654	.49	.17
722	.54	.17
782	.55	.22
964	.47	.28
1006	.44	.31
1063	.40	.33
1138	.38	.38

TABLE V - b SLAG ANALYSIS - RUN # 47

(1018 Electrode - .70% Mn; deoxidized at 320 sec)

Time of Sampling (sec)	Wt % Fe^{2+}
92	.06
323	.36
393	.45
457	.55
494	.58
572	.67
678	.79
773	.93
851	1.01
919	1.09

TABLE V - c SLAG ANALYSIS - RUN # 59

applied, is so durable that a wire brush must be used to remove it on the completion of a run.

Run #40 was carried out exactly as those in section 3.8.4; i.e. with W powder markers and calcium deoxidition, followed by sampling. The results, as shown in Table VI, are very different, however, from those recorded previously.

As a direct consequence of the result obtained in Run #40, two additional experiments were done using the insulated mold. In Run #46, a quantity of barium ferrite (Alpha Products, Beverly, Mass.) was added to the deoxidized slag and slag samples taken. Barium ferrite was used in place of FeO as it appeared to dissolve in the slag much more readily. Levels of FeO > 2% in CaF_2 - CaO slags result in two immiscible liquids[36] and this impairs the rate of dissolution of FeO.

A similar procedure was followed in Run #58, except this time with the replacement of barium ferrite by MnO. This MnO was made from MnO_2 by passing cracked ammonia over the MnO_2 at approximately 600°C for ≃ 24 hours. The resultant product was a characteristic light green colour and was further checked by taking an X-ray powder diffraction pattern. Although MnO does have the same tendency to immiscibility[37] as FeO in CaF_2-lime slags, it nevertheless appeared to dissolve more readily. The operating data and chemical analysis for these two experiments are found in Table VII.

3.8.7 Steady State Melts in Air and With DC Power

In order to test the mathematical mass transfer model further, three additional runs were carried out.

Run #	Average Volts	Average Rms Amps	ΔT(°C)	Slag Skin Thickness (mm)	Average Melt Rate (g sec^{-1})	Final Slag Weight (g)
40 (1018)	22.5	1225	18	1.	3.0	570

TABLE VI - a OPERATING PARAMETERS

Time of Sampling (sec)	Wt % Fe^{2+}	Wt % Mn^{2+}
252	.08	.03
282	.08	.06
353	.08	.06
417	.09	.05
514	.09	.04
612	.09	.05
710	.11	.08
841	.12	.08
945	.12	.08
984	.12	.09

TABLE VI - b SLAG ANALYSIS - RUN # 40

(1018 Electrode - .78%Mn; deoxidized at 200 sec)

Time after Deoxidizing (sec)	Wt % Mn
93	.777
302	.773
418	.760
534	.764
650	.770
720	.759
859	.767

TABLE VI - c INGOT ANALYSIS

RUN # 40

Run #	Average Volts	Average Rms Amps	ΔT(°C)	Slag Skin Thickness (mm)	Average Melt Rate (g sec^{-1})	Final Slag Weight (g)
46 (1018)	23	1275	18	1.5	2.6	570
58 (1018)	23.4	1150	16.5	1.	2.6	600

TABLE VII - a OPERATING PARAMETERS

Time of Sampling (sec)	Wt % Fe^{2+}	Wt % Mn^{2+}
406	.52	.12
454	.47	.20
509	.37	.26
555	.34	.32
609	.30	.32

TABLE VII - b SLAG ANALYSIS

RUN # 46

(1018 Electrode - .74% Mn;
$BaFe_{12}O_{19}$ added 350 sec)

Time of Sampling (sec)	Wt % Fe^{2+}	Wt % Mn^{2+}
328	.31	.65
395	.38	.55
419	.39	.55
468	.43	.53
529	.53	.47

TABLE VII - c SLAG ANALYSIS

RUN # 58

(1018 Electrode - .68% Mn;
MnO added at 280 sec)

Run #50 was essentially a duplicate of #27, 53 (3.8.3) but the inert gas enclosure was removed, leaving the slag surface and electrode open to the atmosphere. The anticipated result would be a higher level of FeO in the slag, chiefly as a result of electrode oxidation. The results of the slag analysis and operating data are given in Table VIII.

All the above melts have been performed using AC power. One expects to find a greatly altered pattern of behaviour in DC operation where the major effect is held to be electrochemical interaction between metal and slag[25] and not the chemical phenomena we have considered to this point. One run was done for each of the DC power modes; Run #52 on electrode -ve and Run #55 on electrode +ve. Both were carried out under helium atmosphere using the CaF_2 - 20% CaO slag as in all the previous cases. The data obtained are to be found in Table IX.

Run #	Average Volts	Average Rms Amps	ΔT(°C)	Slag Skin Thickness (mm)	Average Melt Rate (g sec^{-1})	Final Slag Weight (g)
50 (1018)	23.5	1200	17.5	1.	3.0	540

TABLE VIII - a OPERATING PARAMETERS

Time of Sampling (sec)	Wt % Fe^{2+}	Wt % Mn^{2+}
222	.22	.11
272	.35	.16
398	.41	.20
493	.42	.28
608	.50	.28
703	.59	.34
808	.69	.42
879	.77	.47
938	.79	.51
994	.83	.56
1041	.88	.60

TABLE VIII - b SLAG ANALYSIS - RUN # 50
(1018 Electrode - .75% Mn; AC - air atmosphere)

Run #	Average Volts	Average Rms Amps	ΔT(°C)	Slag Skin Thickness (mm)	Average Melt Rate (g sec^{-1})	Final Slag Weight (g)
52 (1018)	20.5	1400	16	1.	2.1	532
55 (1018)	23.5	1250	16	.7	2.0	578

TABLE IX - a OPERATING PARAMETERS

Time of Sampling (sec)	Wt % Fe^{2+}	Wt % Mn^{2+}
740	.41	.36
800	.42	.37
900	.36	.36
1000	.39	.37
1100	.33	.31
1200	.32	.36
1300	.26	.30
1410	.25	.30
1500	.26	.31
1690	.27	.26
1795	.23	.24
1980	.17	.21

TABLE IX - b SLAG ANALYSIS

RUN # 52

(1918 Electrode - .72% Mn; DC-ve)

Time of Sampling (sec)	Wt % Fe^{2+}	Wt % Mn^{2+}
186	.60	.19
224	.67	.21
263	.68	.20
334	.71	.23
417	.74	.23
502	.79	.25
577	.82	.26
621	.81	.31
653	.83	.29
725	.83	.31
815	.86	.32
903	.87	.31
973	.91	.34

TABLE IX - c SLAG ANALYSIS - RUN # 55

(1018 Electrode - .72% Mn; DC+ve)

CHAPTER 4

RESULTS

4.1 Analysis of Rate Controlling Steps

Prior to modelling the data obtained in the previous chapter, it is worthwhile to investigate the possibility that one or more of the three transport steps ([Mn] in the metal phase, (Fe^{2+}), (Mn^{2+}) in the slag phase) may be rate determining. Should this be the case, our equations would be greatly simplified.

Consider the case where mass transfer is accompanied by a reaction whose equilibrium constant is very large.

$$K = \frac{a_{M^{2+}} a_N}{a_M a_{N^{2+}}} \rightarrow \infty \qquad (4.1)$$

By inspection, it would seem that either or both of the terms a_M, $a_{N^{2+}}$ will tend to zero for a finite numerator in 4.1. Thus, for finite values of activity coefficient, the concentration of reactant in either phase may go to zero. The question of which reactant concentration tends to zero is dependent entirely on the rate of supply to the reaction interface (assumed to be in equilibrium and with instantaneous reaction rate). But, for the oxidation of manganese dissolved in the metal by Fe^{2+} in the slag, the equilibrium constant is approximately equal to only 4. This value prevents us from making any assumptions about reactants tending to zero. In fact, what we must attempt to show

is the reverse possibility; i.e., which, if any, interfacial reactant concentration does not deviate significantly from the bulk value. The procedure is as follows.

Recalling Equation 2.11, we have

$$[Mn]_i = \frac{-b \pm (b^2 + 4c)^{1/2}}{2} \tag{2.11}$$

where

$$b = \frac{k_{Fe^{2+}}}{\Omega k_{Mn^{2+}}} + \frac{k_{Fe^{2+}}}{k_{Mn}} (Fe^{2+})_b - [Mn]_b$$

and

$$c = \frac{k_{Fe^{2+}}}{\Omega} \{ \frac{[Mn]_b}{k_{Mn^{2+}}} + \frac{(Mn^{2+})_b}{k_{Mn}} \}$$

If we consider in b, that

either $$[Mn]_b >> \frac{k_{Fe^{2+}}}{\Omega k_{Mn^{2+}}} \tag{4.2}$$

or $$[Mn]_b >> \frac{k_{Fe^{2+}}}{k_{Mn}} (Fe^{2+})_b \tag{4.3}$$

and in c, that

$$[Mn]_b >> \frac{k_{Mn^{2+}} (Mn^{2+})_b}{k_{Mn}} \tag{4.4}$$

Taking (4.3) and (4.4) to be true for the moment and solving 2.11 we have

$$2[Mn]_i = \frac{-k_{Fe^{2+}}}{\Omega k_{Mn^{2+}}} + [Mn]_b \pm \left(\left(\frac{k_{Fe^{2+}}}{\Omega k_{Mn^{2+}}} \right)^2 - 2 \frac{k_{Fe^{2+}}[Mn]_b}{\Omega k_{Mn^{2+}}} + [Mn]_b^2 + \frac{4k_{Fe^{2+}}[Mn]_b}{\Omega k_{Mn^{2+}}} \right)^{1/2}$$

$$2[Mn]_i = \frac{-k_{Fe^{2+}}}{\Omega k_{Mn^{2+}}} + [Mn]_b \pm \left(\left(\frac{k_{Fe^{2+}}}{\Omega k_{Mn^{2+}}} \right)^2 + \frac{2k_{Fe^{2+}}[Mn]_b}{\Omega k_{Mn^{2+}}} + [Mn]_b^2 \right)^{1/2}$$

taking the positive root

$$2[Mn]_i = - \frac{k_{Fe^{2+}}}{\Omega k_{Mn^{2+}}} + [Mn]_b + \frac{k_{Fe^{2+}}}{\Omega k_{Mn^{2+}}} + [Mn]_b$$

Thus,

$$[Mn]_i = [Mn]_b \qquad (4.5)$$

If the interfacial concentration of the metal phase reactant is approximately equal to the bulk value, this implies that the rate of supply of [Mn] in the metal is sufficiently fast to prevent interfacial depletion. We therefore conclude that, should the inequalities (4.2),

(4.3), (4.4) be shown true for our system, then mass transfer will be controlled by slag phase transport. Table X shows the results of evaluating these inequalities at each of the reaction sites using typical concentration levels, and mass transfer coefficients from Table I.

TABLE X

Evaluation of Terms in Rate Controlling Step Analysis.

$(Fe^{2+})_b \simeq 2.3(10^{-4})$ mole cm^{-3} (.5 wt %)

$(Mn^{2+})_b \simeq 1.9(10^{-4})$ mole cm^{-3} (.4 wt %)

Ω calculated from (2.22) ($\gamma_{MnO} \simeq 3.5$)

Reaction Site	$[Mn]_b$ ① (.76 wt %)	$\frac{k_{Fe^{2+}}(Fe^{2+})_b}{k_{Mn}}$ ②	$\frac{k_{Fe^{2+}}}{\Omega k_{Mn^{2+}}}$ ③	$\frac{k_{Mn^{2+}}(Mn^{2+})_b}{k_{Mn}}$ ④
Electrode Film (Ω=3371)	$1(10^{-3})$	$3.5(10^{-4})$	$3.0(10^{-4})$	$2.9(10^{-4})$
DROP (Ω=1785)	$1(10^{-3})$	$4.3(10^{-5})$	$5.6(10^{-4})$	$3.6(10^{-5})$
Ingot POOL (Ω=1785	$1(10^{-3})$	$1.9(10^{-4})$	$5.6(10^{-4})$	$1.5(10^{-4})$

On comparing the tabulated values in column ① with those in ②, ③ and that in ④ as required by the inequalities (4.2-4.4), it is seen that the values in ① are higher than either ② , or ③ and higher than ④. This is a clear indication of the predominance of the slag transport processes in determining the overall rate of mass transfer, but also it shows that we cannot ignore the contribution of

the metal phase resistance. We must, therefore, use the mass transfer differential Equation (2.12) as derived in the modelling of the data of Chapter 3.

4.2 Results of Experiments to Determine Pool Mass Transfer Coefficients

4.2.1 Experimental Determination of Mass Transfer Coefficients $k_{Mn^{2+}}$, $k_{Fe^{2+}}$

In light of the above phase transport control analysis, it is evident from examination of the results of this analysis at the ingot pool/slag interface that by increasing the concentration of Mn in the metal phase that one might effectively lower the metal phase mass transfer resistance to such an extent that it could be ignored. Experiments 60, 61 were carried out with this in mind (3.8.2). The effective $[Mn]_b$ levels were estimated at 0.8 wt % for Run #60 (ingot pool $\simeq$ 500 g) and 2.3 wt % for Run #61 (ingot pool 2520 gm). Consideration of these levels of [Mn] and the initial levels of $(Fe^{2+})_b$ and $(Mn^{2+})_b$ of Table IIb for the respective runs, with respect to the inequalities 4.2, 4.4 gives the results of Table XI (for the pool only, since Armco iron was used and no reaction is assumed at the electrode tip and at the drop sites).

TABLE XI

Transport Control Data at Ingot Pool for Melts # 60, 61

Run #	$[Mn]_b$ 1	$\frac{k_{Fe^{2+}}(Fe^{2+})_b}{k_{Mn}}$ 2	$\frac{k_{Mn^{2+}}(Mn^{2+})_b}{k_{Mn}}$ 3
60	$1.05(10^{-3})$	$2.3(10^{-4})$	$3.1(10^{-5})$
61	$3.01(10^{-3})$	$2.0(10^{-4})$	$6.9(10^{-5})$

It is apparent from the results of Table XI that while the term 3 is much smaller than 1 , the other is not. Nevertheless, in our subsequent calculation we shall assume $[Mn]_i \simeq [Mn]_b$ (from the result (4.5)) and examine the consequences of this assumption later. From relation 2.9 we have the equation

$$\frac{\dot{n}_{Mn^{2+}}}{A} = \frac{\Omega[Mn]_i(Fe^{2+})_b - (Mn^{2+})_b}{\frac{\Omega[Mn]_i}{k_{Fe^{2+}}} + \frac{1}{k_{Mn^{2+}}}} \qquad (2.9)$$

We have assumed above that $[Mn]_i \simeq [Mn]_b$ and also (in 2.3.4) that $k_{Fe^{2+}} = k_{Mn^{2+}}$. Since

$$\dot{n}_{Mn^{2+}} = V_s \frac{d(Mn^{2+})}{dt} \qquad (2.13)$$

we have

$$\frac{d(Mn^{2+})}{dt} = \frac{A}{V_s}\left\{\frac{k_{Mn^{2+}}}{\Omega[Mn]_b + 1}\right\}\left\{\Omega[Mn]_b(Fe^{2+})_b - (Mn^{2+})_b\right\} \qquad (4.6(a))$$

From the data of Table IIb we obtain the plots given in Figure 16 showing the rate of rise of (Mn^{2+}) in the slag (i.e. $\frac{d(Mn^{2+})}{dt}$) immediately after manganese was added to the metal pool. The slopes were obtained by linear regression analysis of the available points. The only remaining unknown, now, in Equation 4.6(a) is $k_{Mn^{2+}}$. Rearranging 4.6(a)

$$k_{Mn^{2+}} = \frac{(d(Mn^{2+})/dt)V_s(\Omega[Mn]_b+1)}{A(\Omega[Mn]_b(Fe^{2+})_b-(Mn^{2+})_b)} \qquad (4.6)$$

The values of $d(Mn^{2+})/dt$ determined from Figure 16 and the remaining parameters of (4.6) evaluated at t = 0 from data in Table IIb and Table I are summarized in Table XII below. We use the initial time,

TABLE XII

Summary of Data for Experimental Evaluation of $k_{Mn^{2+}}$

(all concentrations in moles cm^{-3})

Parameter	Run #60	Run #61
Ω	2500	2575
A/V_s	.624	.624
$[Mn]_b$	3.03 (10^{-3})	1.05(10^{-3})
$[Mn^{2+})_b$	8.77 (10^{-5})	3.79(10^{-5})
$(Fe^{2+})_b$	1.49 (10^{-4})	2.04(10^{-4})
$d(Mn^{2+})/dt$	8.06 (10^{-7})	7.58(10^{-7})

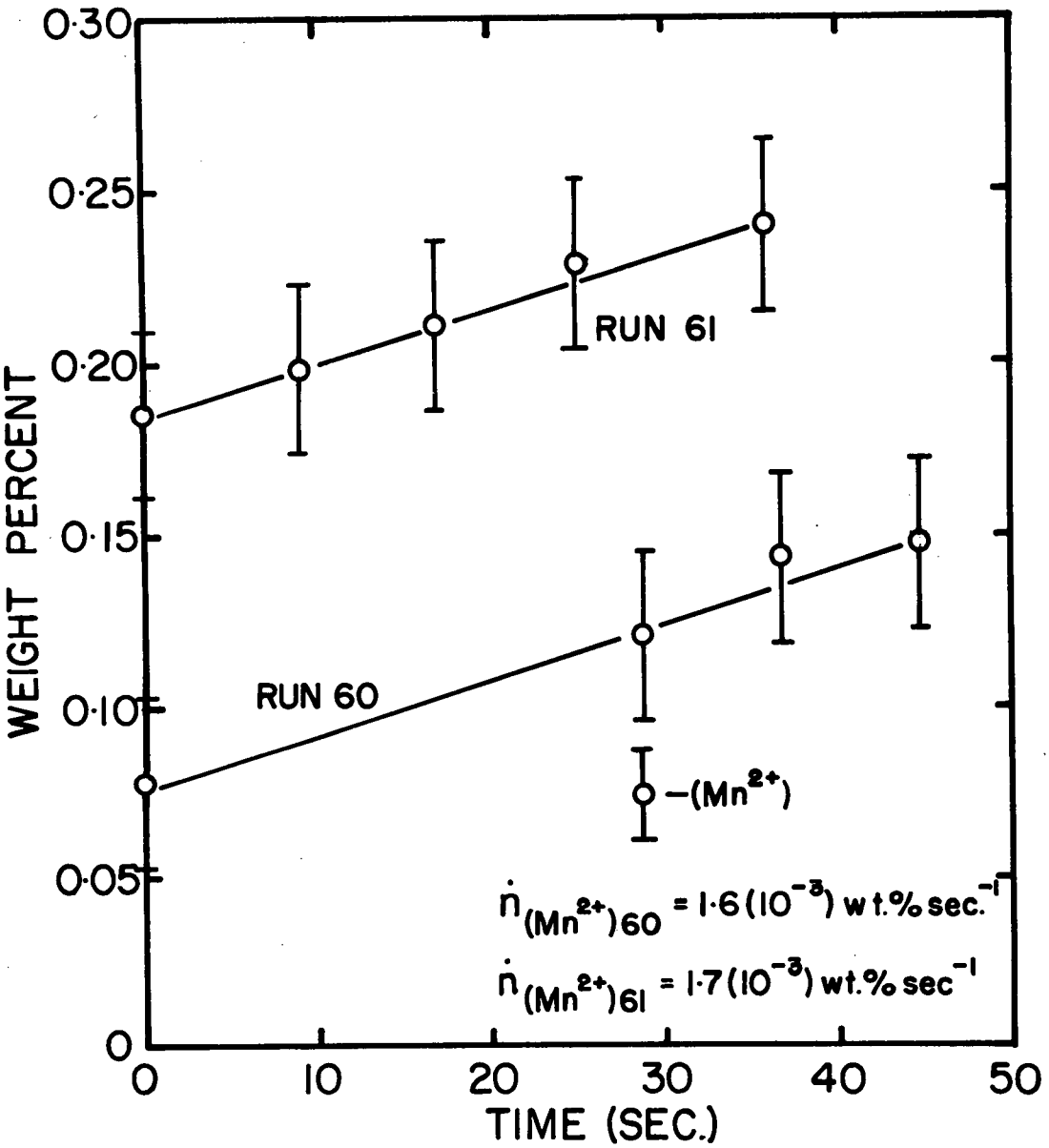

Figure 16 Experimental Determination of Rate of Rise of Mn^{2+} in Slag During Oxidation of Mn in Ingot Pool Only (Melts #60,61)

t = 0, since this is the only time that $[Mn]_b$ is known (assuming complete mixing in the liquid metal pool)[35,56] without prior knowledge of k_{Mn}^{2+}. Ω is evaluated at 1675°C, γ_{MnO} being taken from Figure 20.

The values of k_{Mn}^{2+} (and hence k_{Fe}^{2+}) obtained were 0.011 cm sec^{-1} for Run #60 and 0.009 cm sec^{-1} for Run #61. The theoretically modelled value of $k_{Mn}^{2+}(k_{Fe}^{2+})$ was 0.013 cm sec^{-1}. The agreement is good in view of the assumptions made with respect to metal phase mass transfer resistance. Also some manganese is undoubtedly being reduced at the electrode tip and to a lesser extent at the falling drops, thereby lowering the slag Mn level. Thus we might anticipate obtaining a low value from the procedure used in this instance.

4.2.2 Experimental Determination of the Mass Transfer Coefficient k_S^{2-}

Although we have not discussed the mass transfer model for desulphurization to date, a comprehensive mathematical treatment is given in Appendix III. The major purpose of the experiment to determine k_S^{2-}(#62), was to demonstrate further that the mass transfer coefficients as calculated from the penetration theory etc. are realistic. By using the desulphurization reaction

$$[S] + Fe_{(\ell)} \rightarrow (Fe^{2+}) + (S^{2-}) \qquad \text{(A3.3)}$$

as described in Appendix III, we have altered several aspects of the mass transfer phenomena. Firstly, the equilibrium constant is greatly reduced (in fact, by almost 2 orders of magnitude (cf. Appendix III). Also the diffusion coefficient of (S^{2-}) in the slag is somewhat higher

than that used for (Mn^{2+}), (Fe^{2+}) and hence the anticipated mass transfer coefficient will be correspondingly higher.

From Appendix III, we have the following relationship, similar to that used in the previous section (cf. Equation 4.6).

$$k_{s^{2-}} = \frac{(V_S/A(d(S^{2-})/dt}{\frac{\Omega_S[S]_i}{\frac{V_S}{A}\left(\frac{d(S^{2-})}{dt}\right)\frac{1}{k_{Fe^{2+}}} + (Fe^{2+})_b} - (S^{2-})_b} \qquad (A.3.12)$$

$$\text{where } \Omega_S = \frac{1.22\ \text{Exp}(2330/T - 4.07)\ \rho_S}{\gamma_{CaS}\ \gamma_{FeO}\ \rho_M} \qquad (A.3.15)$$

It will be assumed again that the effect of adding a quantity of FeS to the metal pool was sufficient to reduce metal phase mass transfer resistance. Hence $[S]_i$ becomes $[S]_b$ in (A.3.12).

In Figure 17, the results of Run #62 are plotted using the data from Table IIb. It was apparent in this run that a large quantity of FeS transferred instantly to the slag without dissolving in the metal pool. Taking a mass balance on the slag we find that since the initial level of slag sulphur was approximately .08 wt % and final was .35 wt %, the change in sulphur level of .27 wt % times the final slag volume of 520 gms gives us 1.40 gms of sulphur. A total of 1.38 gms of S was added (4 gms FeS at 34.5 % S) and thus we have a reasonably sound overall mass balance. However, when the first sample was taken, 10 secs after introduction of the FeS, the slag sulphur level had risen to .25 wt %. This would appear to have been caused by incomplete solution of the FeS in the metal and thus we must calculate an ingot

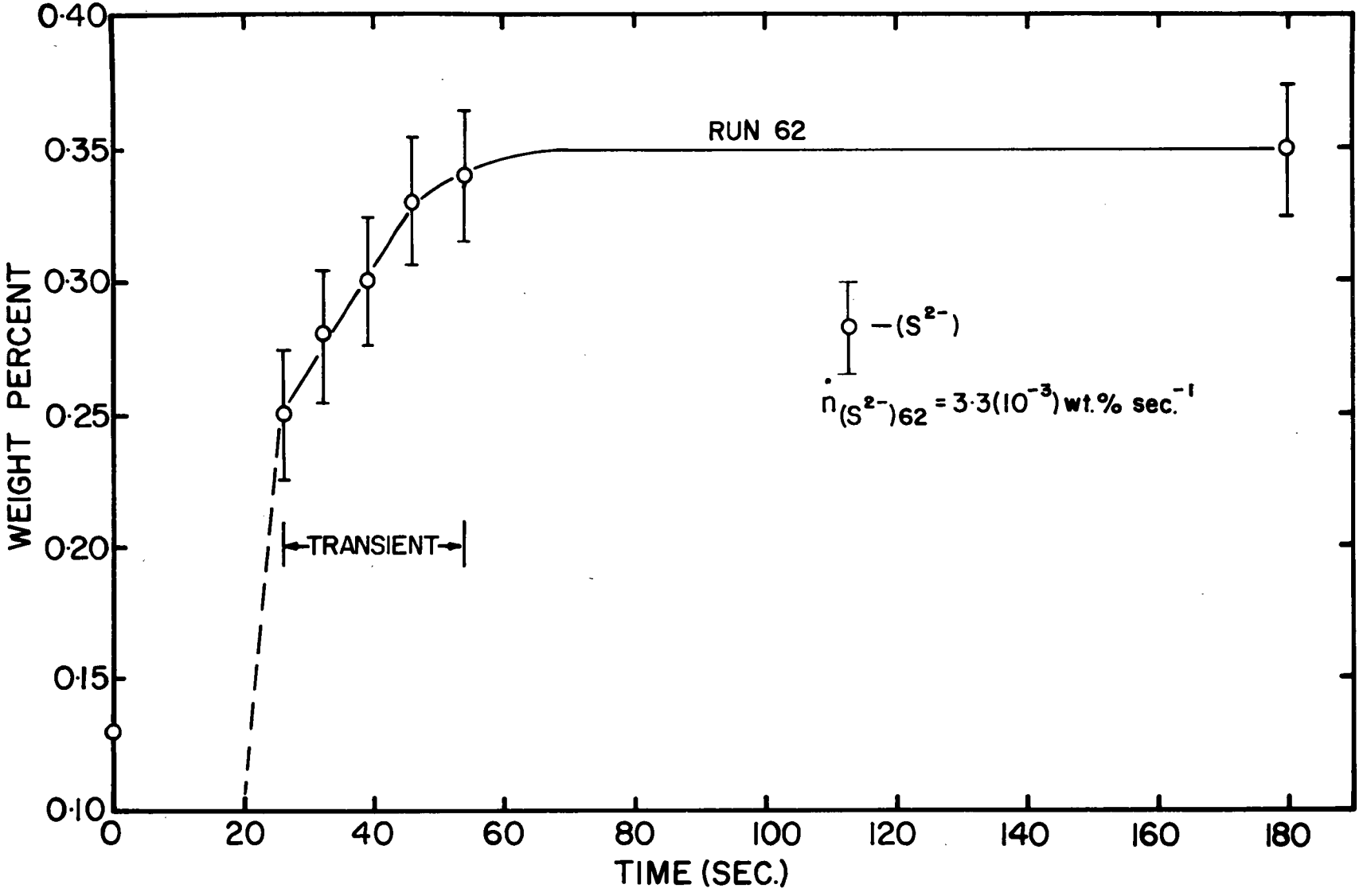

Figure 17 Experimental Determination of Rate of Rise of S^{2-} in Slag after FeS Addition to Ingot Pool

sulphur level at the time of the first sample.

The initial increase was from .08% to .25%, a total of .17 wt % or in terms of the total change of .27 wt %, 68%. Thus only 32% remained in the ingot pool. The pool weight was estimated to be ≃ 500 gms, yielding a S level of

$$\frac{.32 \times 1.38}{500} \quad \text{or} \quad .088 \text{ wt \%}$$

The time of first sample marks the beginning of a short period of linear rate of rise of (S^{2-}). The measured $d(S^{2-})/dt$ from the graph of Figure 17 is $4.23(10^{-6})$ mol cm^{-3} sec^{-1}. The values of the remaining parameters needed to estimate k_S2- are given in Table XIII. The concentrations $(Fe^{2+})_b$, $(S^{2-})_b$ were taken from Table IIb. The value of γ_{FeO} was the usual one of 3.0 and that of γ_{CaS} is estimated to 2.4[17]. A temperature of 1675°C is used for calculating Ω_S.

TABLE XIII

Data for Experimental Evaluation of k_S-2

Parameter	Value Used
V_S/A	1.602
Ω_S	$2.28(10^{-3})$
$d(S^{2-})/dt$	$4.23(10^{-6})$
$(Fe^{2+})_b$	$1.86(10^{-4})$mol cm^{-3}
$(S^{2-})_b$	$2.03(10^{-4})$ "
$[S]_b$	$2.02(10^{-4})$ "

The experimentally determined value of k_S2- is found to be 0.016 cm sec^{-1}. Using the penetration theory as applied in Chapter 2 and the diffusion coefficient[90] for S^{2-} (in fused salts) where

$$D_S2- = 3.8(10^{-4}) \text{ cm}^2 \text{ sec}^{-1}$$

we have

$$k_S2- = 2 \left(\frac{3.8(10^{-4})}{\pi \times .37} \right)^{1/2} = .036 \text{ cm sec}^{-1}$$

The experimentally determined value is about one half of the modelled value. There are several possible explanations for this. One is that the diffusion coefficient of S^{2-} had been overestimated. Using a value of $D_S2- = 10^{-4}$, k_S2- becomes .019, i.e. much nearer the value calculated from the data. Another rational might be that our assumption of $[S]_i = [S]_b$ is not true. It is obvious from the expression for k_S2-, that decreasing [S] in the equation will raise the value of k_S2-. However, it is unlikely that the interfacial value of [S] is much less than $[S]_b$ because of the high diffusion coefficient of S in the metal.

These two experiments to calculate mass transfer coefficients from experimental data show that our modelled values are indeed quite reasonable. Hence, having established some confidence in our modelled mass transfer coefficients, we proceed with the modelling of the remainder of the experimental data for the runs described in Chapter 3 using the values of mass transfer coefficients given in Table I.

4.3 Boundary Conditions for Solution of Mass Transfer Model

In effect we must solve the differential equation of mass transfer

$$d[Mn] = -\frac{A}{V_M} k_{Mn} \{[Mn]_b - [\frac{-b \pm (b^2 + 4c)^{1/2}}{2}] \} \qquad (2.14)$$

where $$b = \frac{k_{Fe^{2+}}}{\Omega k_{Mn^{2+}}} + \frac{k_{Fe^{2+}}}{k_{Mn}} (Fe^{2+})_b - [Mn]_b$$

$$c = \frac{k_{Fe^{2+}}}{\Omega} \{ \frac{[Mn]_b}{k_{Mn^{2+}}} + \frac{[Mn^{2+}]_b}{k_{Mn}} \}$$

for 3 concentrations via the steady state assumption

$$d(Mn^{2+})_b = -d(Fe^{2+})_b = -d[Mn]_b \frac{V_M}{V_S} \qquad (2.15)$$

In other words, the differential equation contains three variable concentrations $(Fe^{2+})_b$, $(Mn^{2+})_b$ and $[Mn]_b$. Each of these must, therefore, be specified in the initial condition as

$$(Fe^{2+})_{b,0}, (Mn^{2+})_{b,0}, [Mn]_{b,0} \text{ at } t = 0 .$$

Since we are applying (2.14) to three reaction sites and solving these simultaneously as described in 2.5, it is necessary to add that $[Mn]_{b,0}$ must be specified in the electrode tip (i.e. the bulk electrode value) and at the ingot pool site (assumed equal to the bulk electrode value at t = 0). It is further assumed that all three reaction sites see the same concentration of $(Fe^{2+})_b$ and $(Mn^{2+})_b$ at any time. The value $[Mn]_{b,0}$

for the drop site is taken as the value of $[Mn]_b$ in the film after a short period corresponding to the formation of one drop. With the exception of the latter concentration, all other initial values are determined from the experimental data for each individual melt.

4.4 Use of Fe^{2+} "Potentials"

Examination of the data given in Tables II through IX showed that (Fe^{2+}) concentrations range from a low of .03 wt % to a high in excess of 1 wt %. It became evident that the rates of generation and loss of Fe^{2+} were usually quantitatively unpredictable. Without specific knowledge of these rate terms we cannot model the concentration changes for Fe^{2+}. This lack of information was, of course, the rationale behind the experiments using live and insulated molds and the results of these experiments will be duly discussed. Nevertheless, insufficient information was obtained on the Fe^{2+} production phenomenon and we were forced to adopt a different approach.

The concept of using an imposed Fe^{2+} potential was selected. This involved the very simple operation of drawing a series of one or more straight lines through the Fe^{2+} data points. The slopes of these lines were then incorporated into the computer program as production or loss terms for Fe^{2+}. Hence the concentration of Fe^{2+}, termed the "Fe^{2+} potential," was known at any time and was used in the subsequent solution of the differential equations. The model is obviously limited now to predicting concentration changes of only manganese in the ingot and slag.

The plots of the data and of the modelled slag and ingot profiles (where applicable) show generally three types of line. The first of these is an imposed Fe^{2+} potential line, following the data obtained for Fe^{2+} in each experiment. Secondly, there is a line showing the model predicted (Mn^{2+}) composition and finally, a series of 3 lines giving the contributions of the various reaction sites (electrode film, falling drop and ingot pool) towards the overall change in slag (Mn^{2+}) level. These latter lines were normalized at zero time to zero percent contribution.

4.5 Choice of γ_{MnO}

In Figure 10, the known data for γ_{MnO} versus wt % MnO in CaF_2 - CaO melts was presented. It was observed (2.3.2) that γ_{MnO} does not, in all likelihood, obey Henry's Law even in dilute solution. Furthermore, the data given in Figure 10 does not extend to the 20% CaO in CaF_2 system and it was suggested (2.3.2) that in applying the mass transfer model that the approach we would adopt would be to fit the model with self consistent values of γ_{MnO}. It was found that all of the modelling work could be successively correlated using a linear variation of γ_{MnO} as shown in Figure 18, where the dotted lines indicate the degree of scatter of values from run to run. The value of γ_{MnO} for each level of $(Mn^{2+})_i$ was calculated by the subroutine OMT (Appendix IV) and thus internal consistency was maintained. It is also worth noting that these "fitted" values are in line with those one might anticipate with the increased CaO content of the slag.

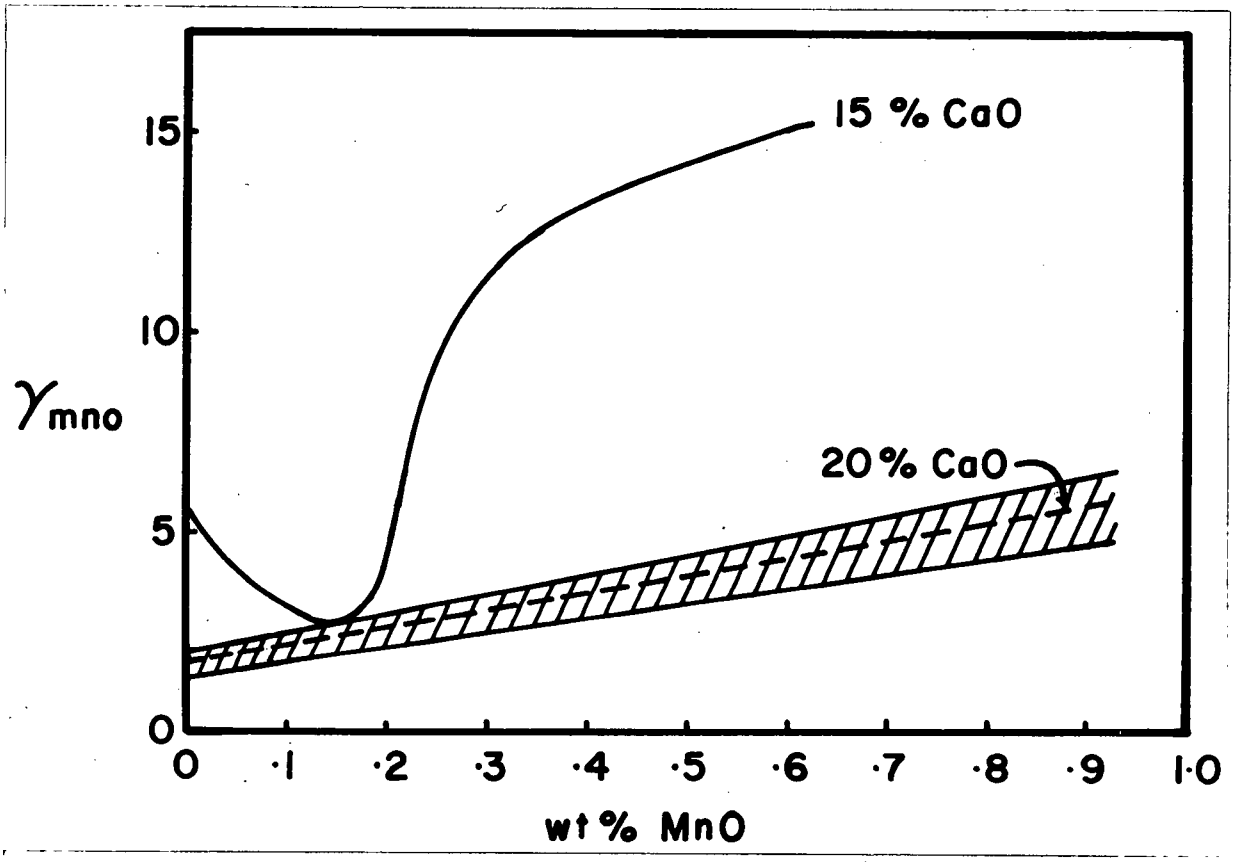

Figure 18 γ_{MnO} Values Fitted by Computer Program for CaF_2-20% CaO Slag

4.6 Modelling Results

All of the necessary parameters and boundary conditions for use in the mathematical model have now been detailed. It was found that taking the positive square root in the quadratic part of the differential Equation (2.14) provided meaningful results. No significance is attached to the negative root since it leads to a negative value of concentration.

The predicted composition changes are presented below in graphical form and compared to the experimental data.

4.6.1 Steady State Results

Figures 19 and 20a (Runs 27, 53, respectively) exhibit very nearly identical patterns of behaviour. The (Fe^{2+}) levels rise from $\simeq$ .3 wt % to $\simeq$ .5 wt % during the course of each melt, the rate of rise of Fe^{2+} being slightly higher in the latter.

The predicted (Mn^{2+}) concentration change in the slag is in good agreement with the experimental data for both of these runs. In Figure 20b, the predicted ingot profile for [Mn] in Run #53 is compared with the ingot analysis, again with satisfactory agreement. The overall axial variation in manganese content is 6.5% which, although it may not be a serious loss for 1018, may represent a substantial loss for another alloy system.

Of particular interest here are the relative contributions to mass transfer at each reaction site. The film site and the drop

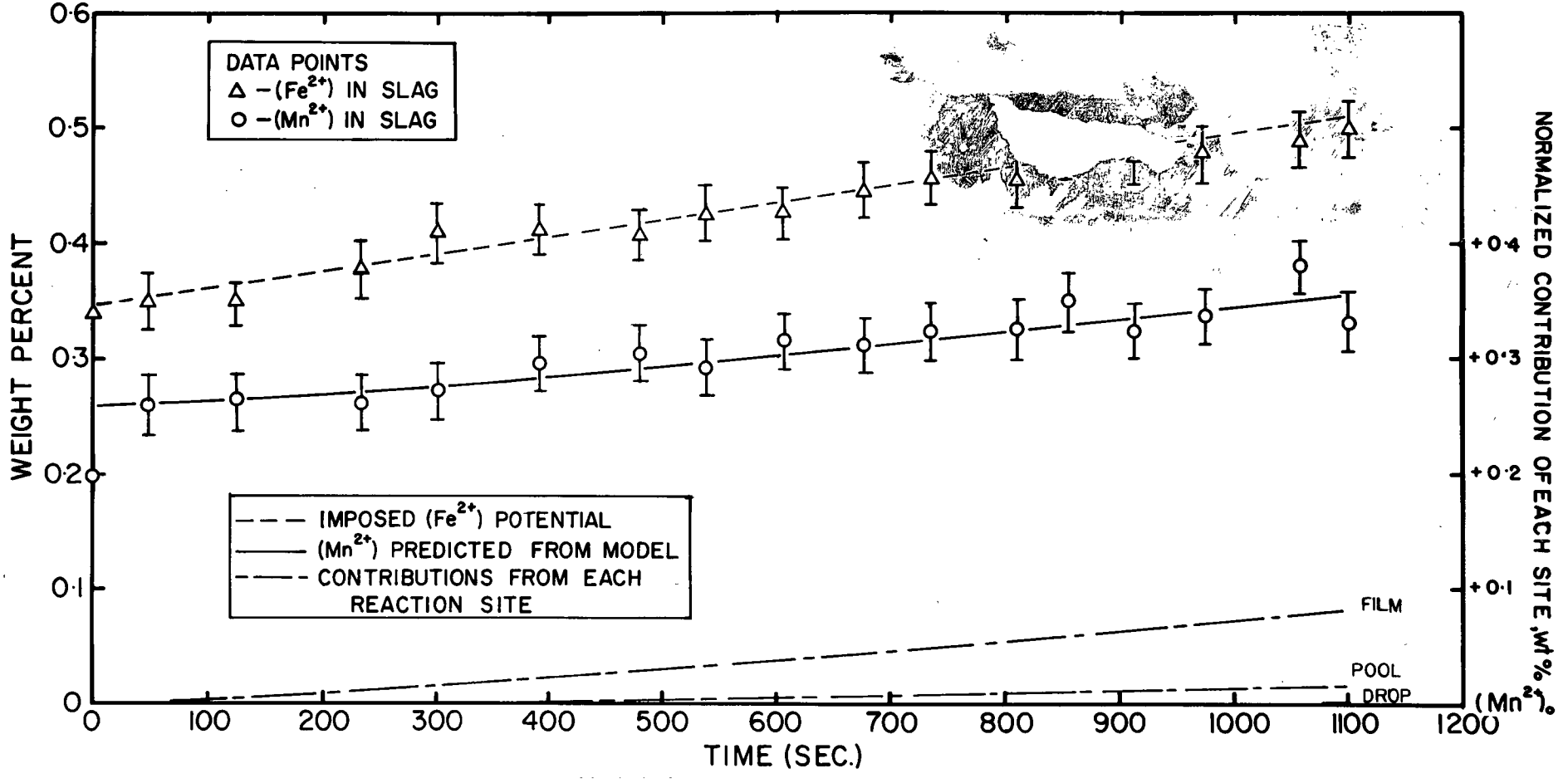

Figure 19 Comparison of Theoretical Mass Transfer Calculations to Experiment Results for Slag Composition vs Time Profile for Steady State Melt #27

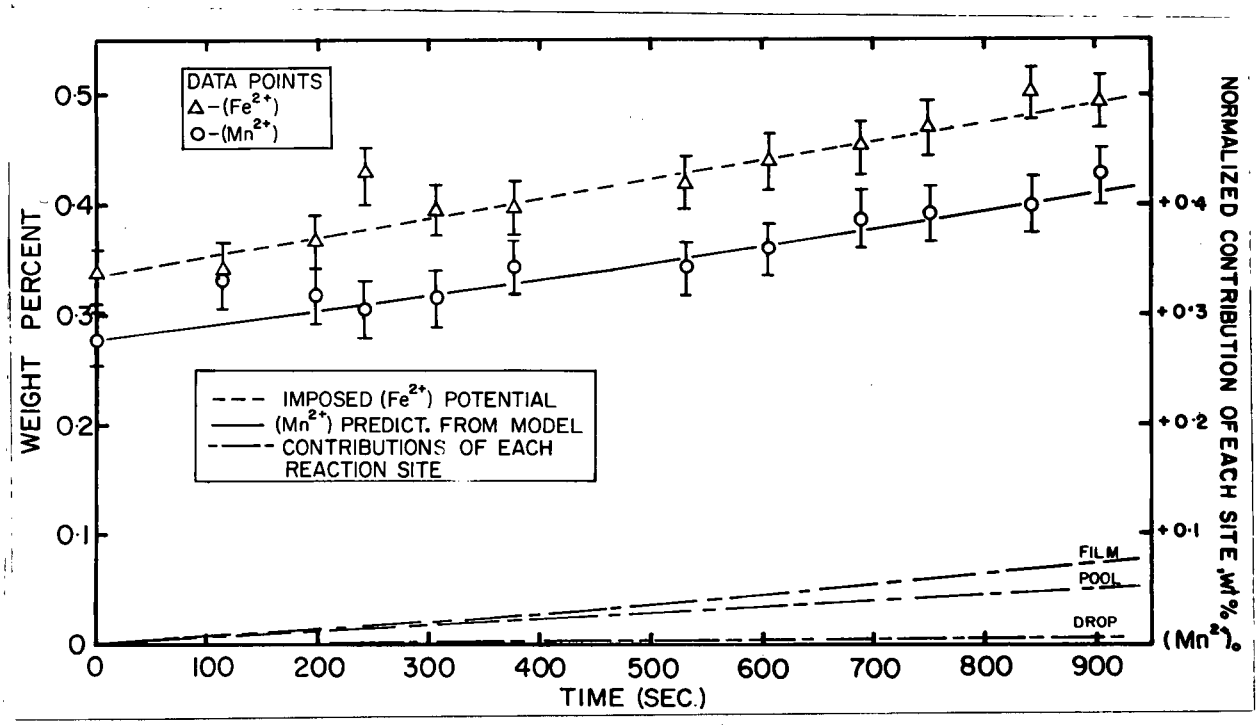

(a)

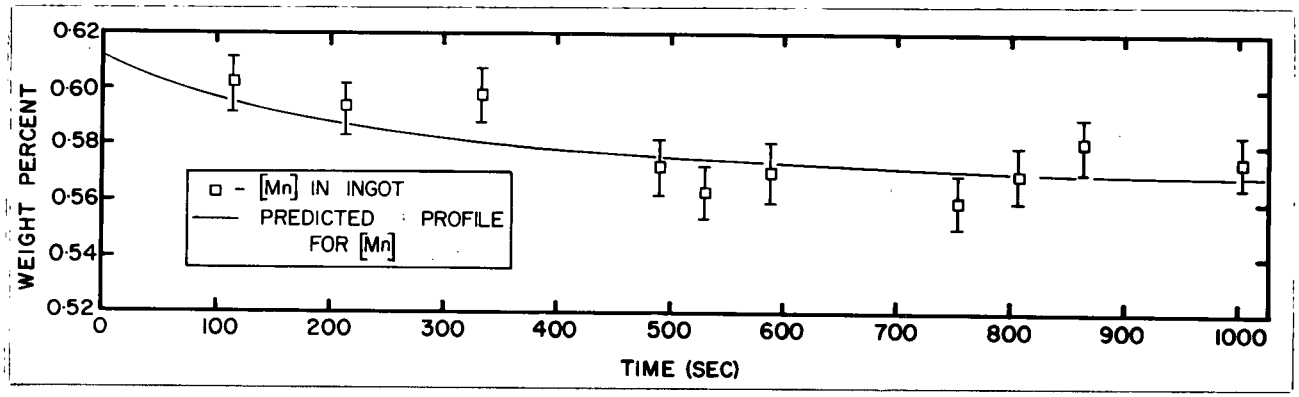

(b)

Figure 20 Comparison of Theoretical Mass Transfer Calculations to Experimental Results for Melt #53
(a) Slag Composition vs. Time Profile
(b) Ingot Composition vs. Time Profile

site exhibit very nearly identical from run to run. The major difference between the runs is the enhanced rate of Mn oxidation at the ingot pool/slag interface in run #53, where the final level of (Mn^{2+}) and (Fe^{2+}) in the slag are somewhat greater than in Run #27. It would appear that the ingot pool reaction is more sensitive to changes in the oxidation potential of the slag than are the other two sites. Should this be the general case, one might expect a much more obvious trend to be observed in the unsteady state condition.

Of note also is the very minor role that is played by droplets in the overall contribution to mass transfer ($\simeq$ 1% in #53; i.e. .005% in total change of .415%). This confirms the evidence of Cooper et al.[14] which indicated that droplets were of little significance in determining the overall rate of desulphurization.

4.6.2 Unsteady State Results

The results of modelling the unsteady state melts #'s 30,31,34, 37,42 are compared to the experimental data in Figures 21 through 24. Again the calculated composition changes are in reasonable agreement with the slag analyses in each case and also for ingot [Mn] profile of Run #42 (Figure 24b).

It is very apparent from these results that, following the deoxidation of the slag with calcium at some time <0 (see Table IV), the system reacts quickly to produce (Fe^{2+}). The level of (Fe^{2+}) builds up very rapidly and then decays in some fashion which is not particularly consistent from melt to melt. It is cases such as these where the necessity of using the imposed (Fe^{2+}) potential becomes

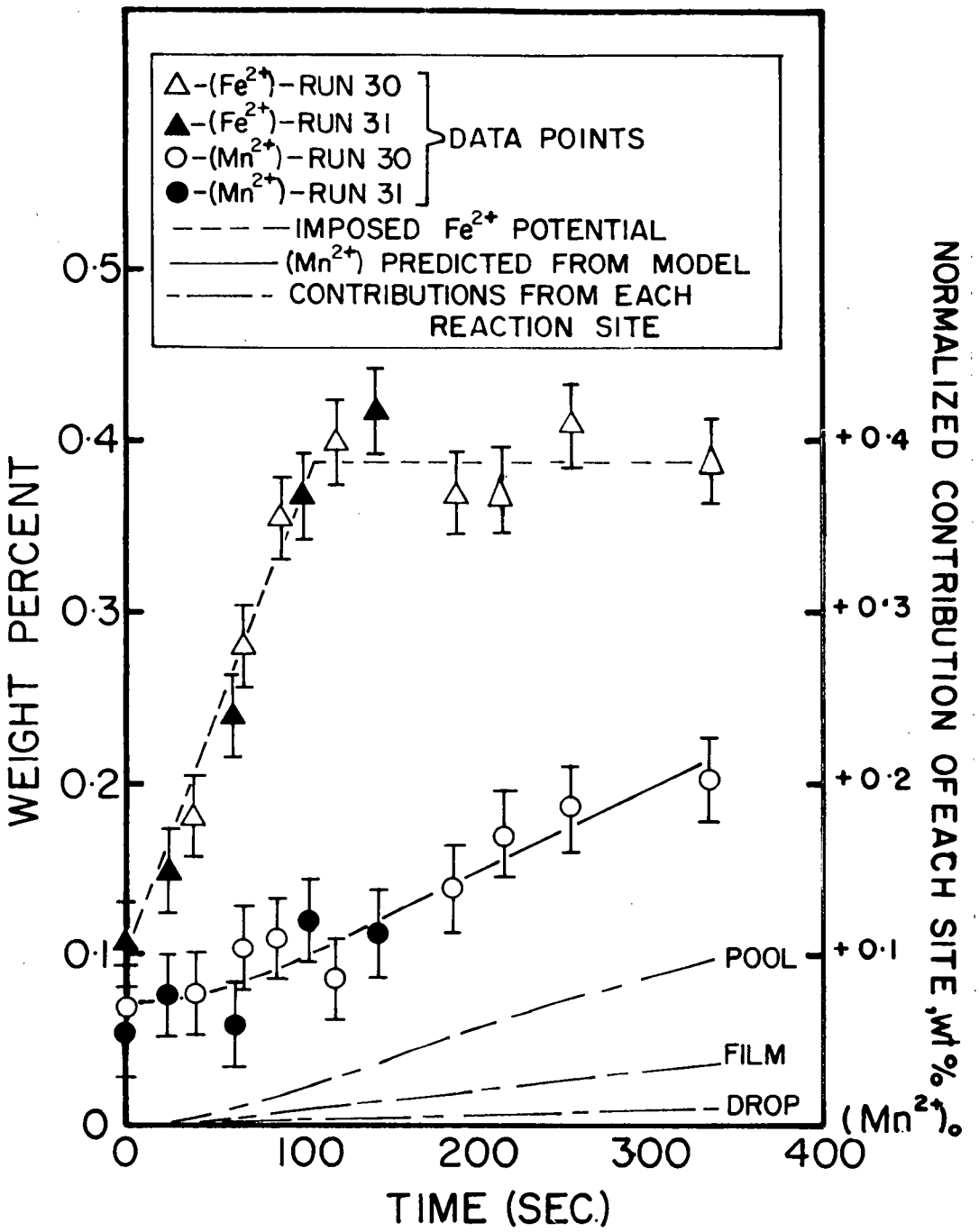

Figure 21 Comparison of Theoretical Mass Transfer Calculations to Slag Composition vs. Time Profile for Melts 30, 31

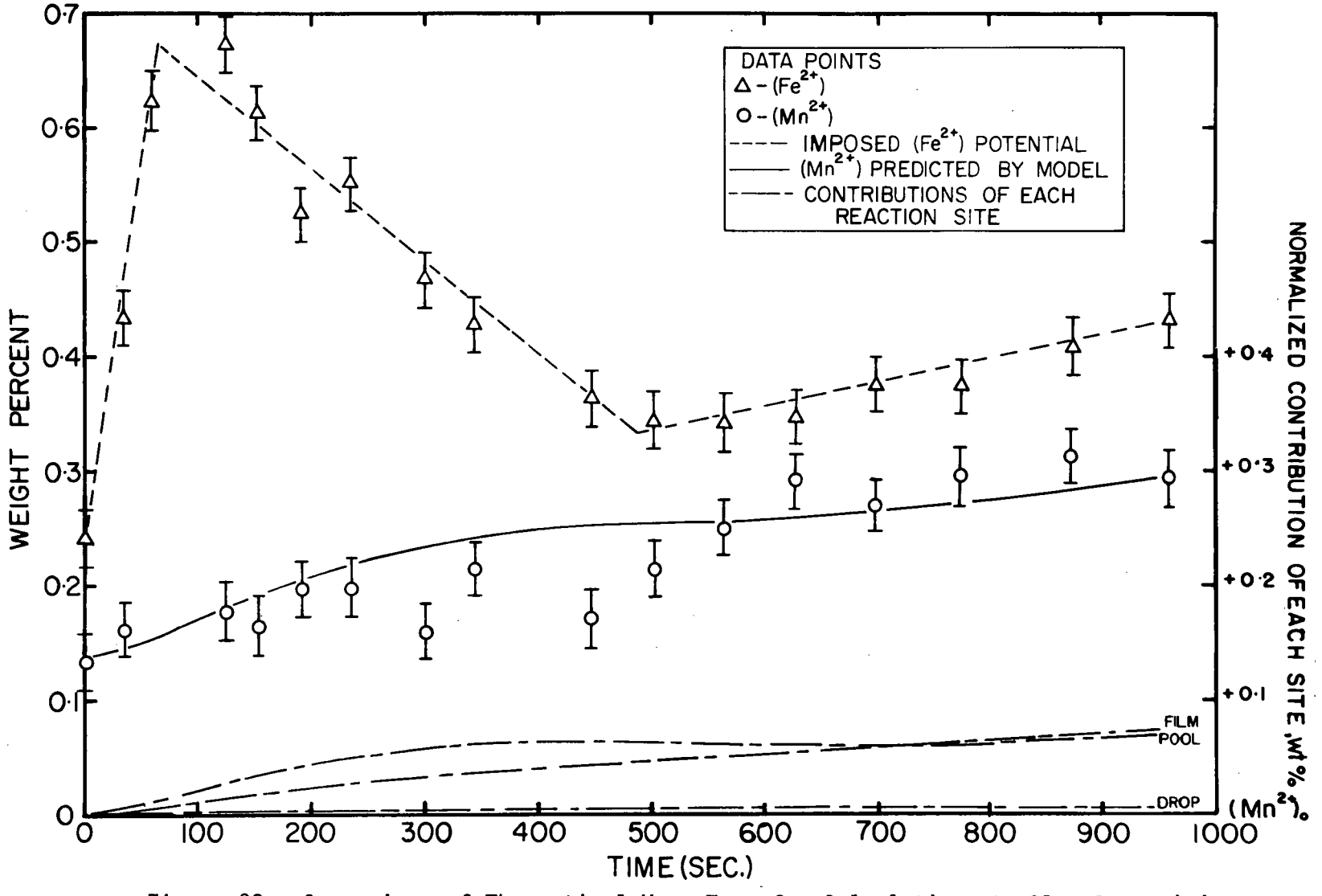

Figure 22 Comparison of Theoretical Mass Transfer Calculations to Slag Composition vs Time Profile for Run #34

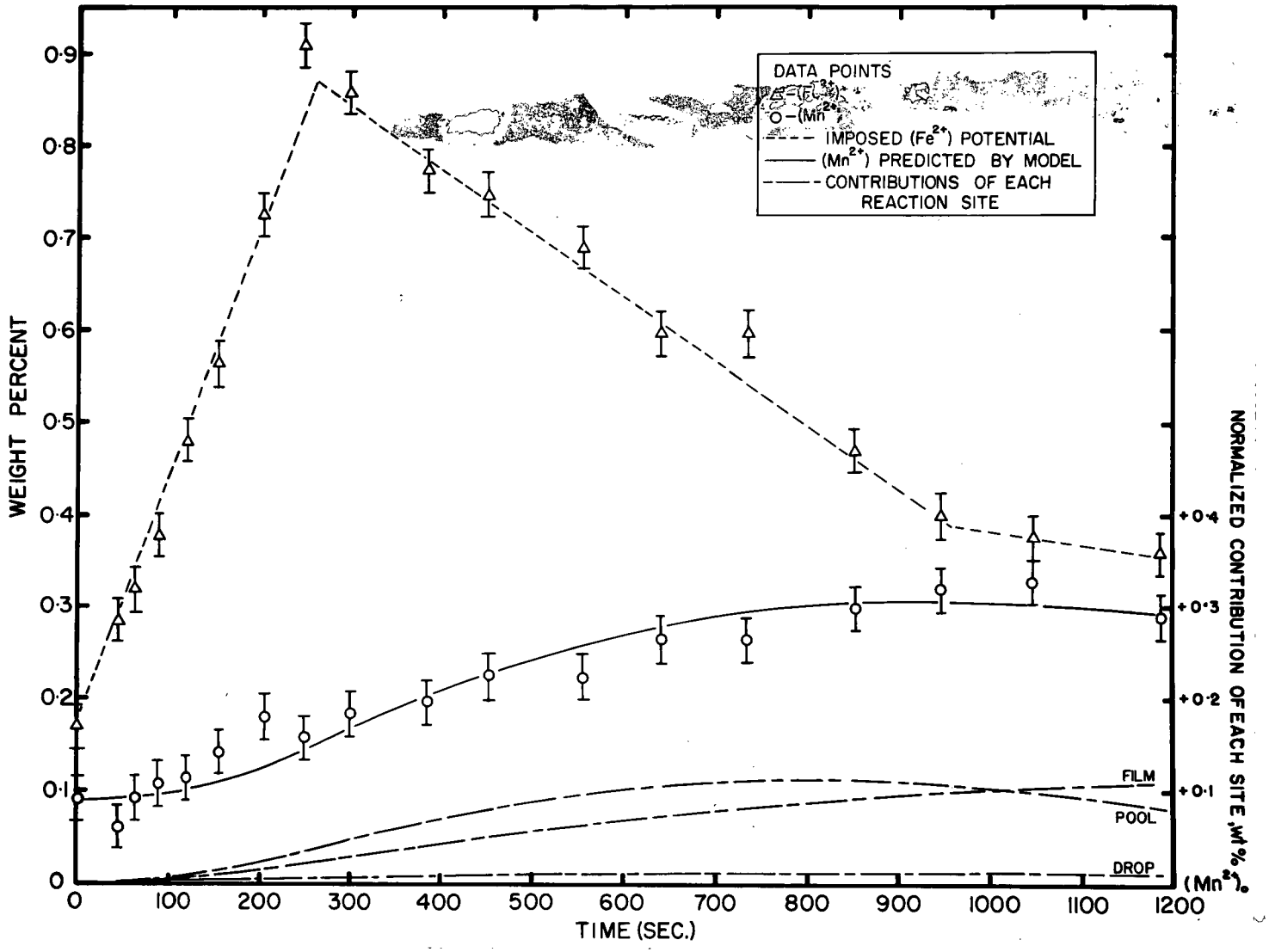

Figure 23 Comparison of Theoretical Mass Transfer Calculations to Slag Composition vs Time Profile for Melt #37

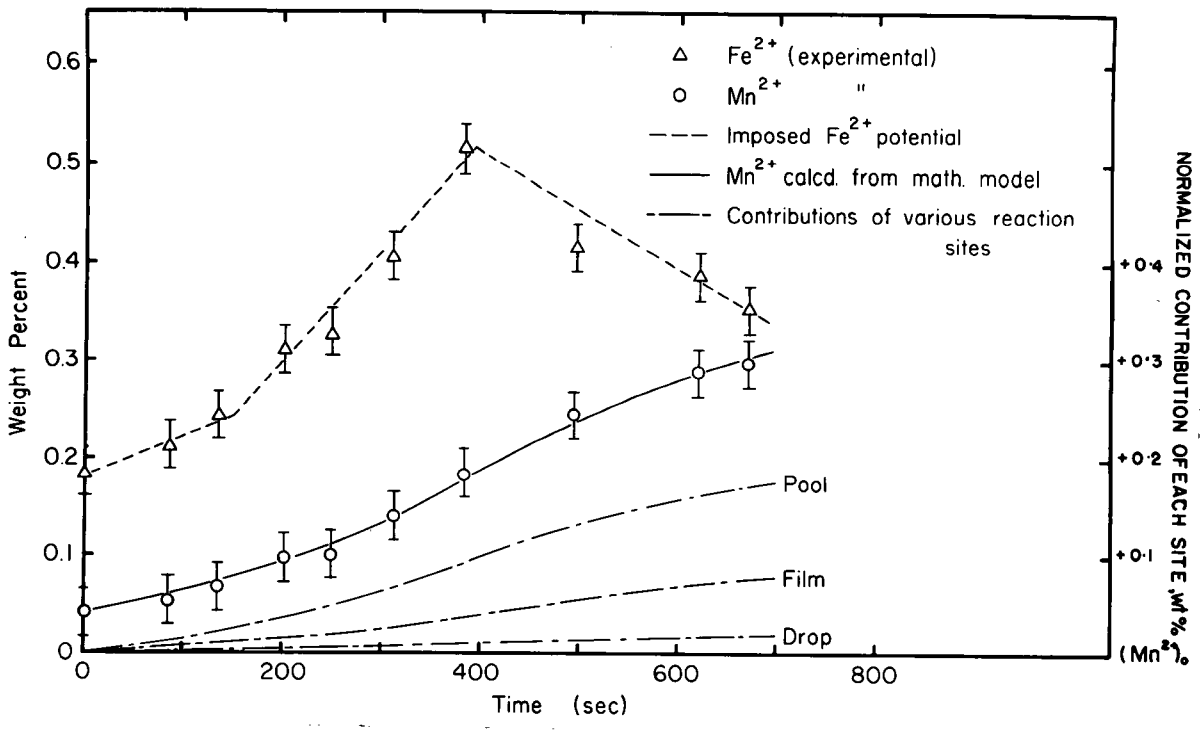

(a)

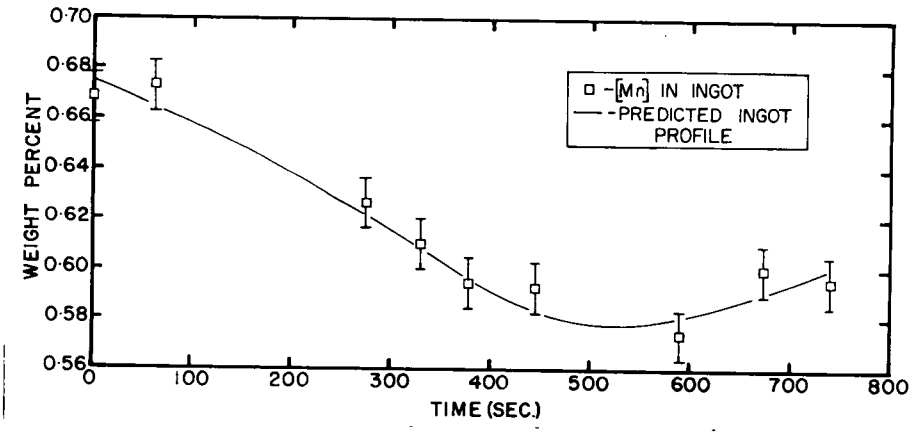

(b)

Figure 24 Comparison of Theoretical Mass Transfer Calculations to Experimental Results for Melt #42

(a) Slag Composition vs. Time Profile
(b) Ingot Composition vs. Time Profile

clearer. The turnover in slope of the (Fe^{2+}) level appears to be connected with an increase in rate of change of (Mn^{2+}) which is what one would expect on a qualitative basis. Also apparent is that the initial rate of generation of (Fe^{2+}) is not constant, further frustrating any attempts at rationalizing this mode of behaviour.

In one run, however, (# 37), the recorded current trace exhibited a large number of discontinuities soon after deoxidizing. It is known that these irregularities are associated with arcing to the mold wall.[85] An arc may be used to rectify an AC signal and this leads us to the conclusion that a certain amount of rectification of the AC current was probably occurring in the only part of this run. The end result of this is a net DC component of the total current which could very likely lead to production of Fe^{2+}.[25] In order to verify this observation the experiments on live and insulated molds (3.85, 3.86) and those on DC power (3.87) were undertaken. The results of these investigations are given in detail later in the next sections.

Recalling the observations made regarding the relative contributions of the three reaction sites, it was stated, (a) that the droplets appeared to have little effect on the total amount of mass transfer and (b), that the rate of oxidation of Mn at the electrode film/slag interface seemed to be constant, with the major response to the changing Fe^{2+} potential arising from the ingot pool reaction. The transient behaviour of the Fe^{2+} potential in the unsteady state melts reinforces this view in every respect. Not only does the contribution of the drops remain relatively trivial and the film rate remain nearly

constant and consistent with the steady state values, but also the rate of transfer at the ingot pool seems to reflect the Fe^{2+} potential variations with a certain time lag effect. This is especially noticeable in the longer time interval experiments, #'s 34, 37 and 42, (Figures 22-24) and particularly in the ingot profile of Run # 42 (Figure 24b). We also notice here, for the first time, the appearance of a reversion reaction (Figures 22 and 23) where rate of Mn oxidation at the ingot pool drops to zero and subsequently is reversed to a reduction of (Mn^{2+}) back into the ingot. These observations have important ramifications in the understanding of inclusion formation in ESR ingots which will be developed at a later stage.

It is clear, then, that the use of an imposed Fe^{2+} potential has enabled us to overcome the problem of unknown rates of Fe^{2+} production and consumption in our efforts to model the composition changes relating to manganese transfer. The mass transfer model appears to predict these concentration changes in both slag and ingot with a good degree of accuracy and with a minimum of curve fitting. It is pertinent, therefore, that we continue with a detailed examination of the experiments done to investigate the nature of the Fe^{2+} production and subsequent experiments designed to further test the model.

4.6.3 Results of the Live Mold Experiments

The data of Run # 47 are compared to the predicted (Mn^{2+}) composition changes in Figure 25 with reasonable agreement between them. The most striking feature of this plot, however, is the similarity with

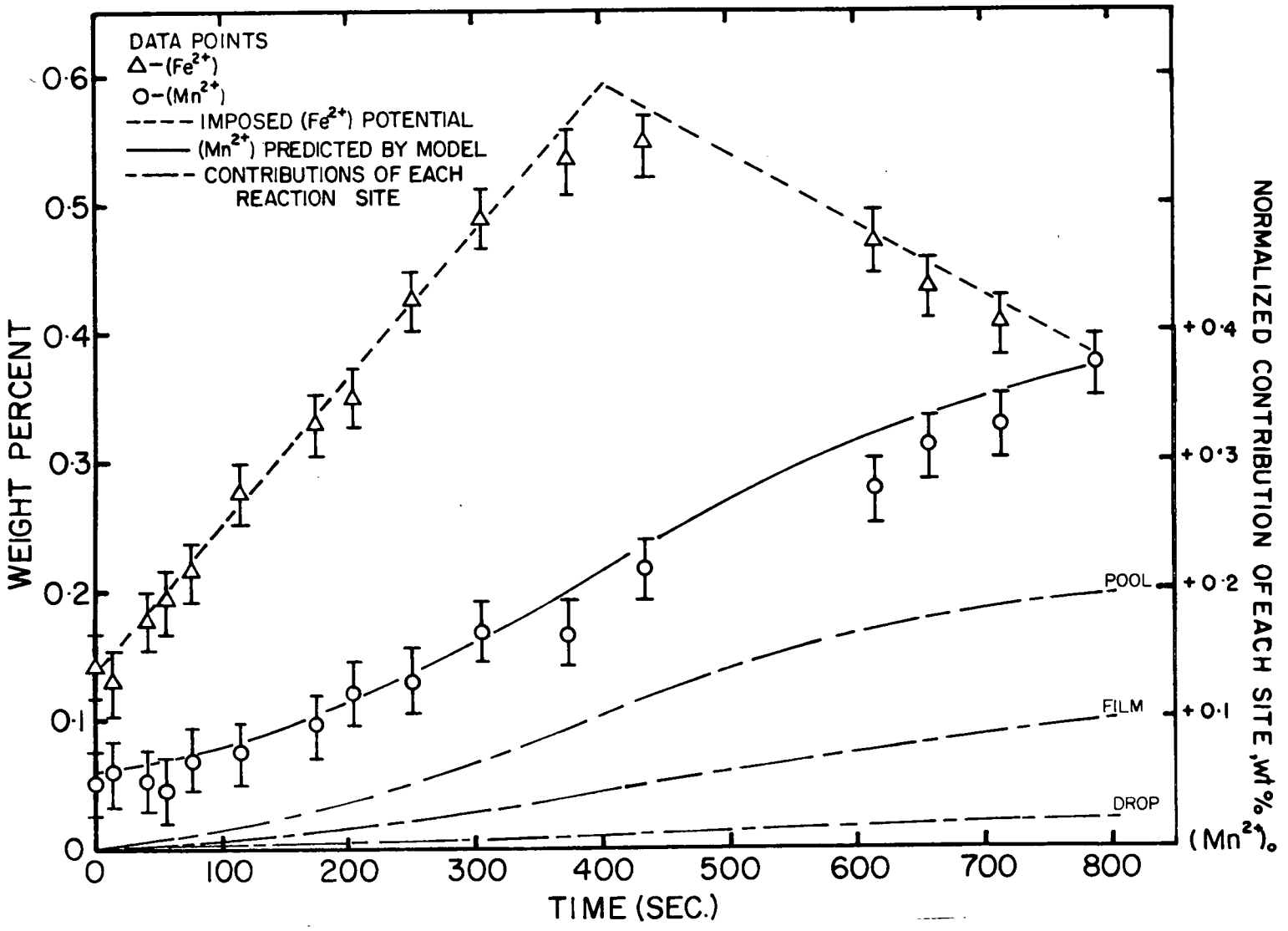

Figure 25 Comparison of Theoretical Mass Transfer Calculations to Slag Composition vs Time Profile for Melt #47 (Live Mold)

the unsteady state melts of the previous section. The former experiments were performed with the normal mold configuration and the latter with live mold. This suggests that in actual practice the normal mold configuration has, in fact, behaved as a live mold, i.e., some current did pass through the mold. The question we must ask now is "how does this relate to the problem of Fe^{2+} generation?"

During the course of Run #47, the mold current was monitored on an oscilloscope as mentioned previously. Although it was, unfortunately, impossible to assess the magnitude of this amperage with any degree of accuracy, the amperage trace itself provides some interesting qualitative information. Figure 26 shows a typical AC waveform of the mold current on the live mold run.

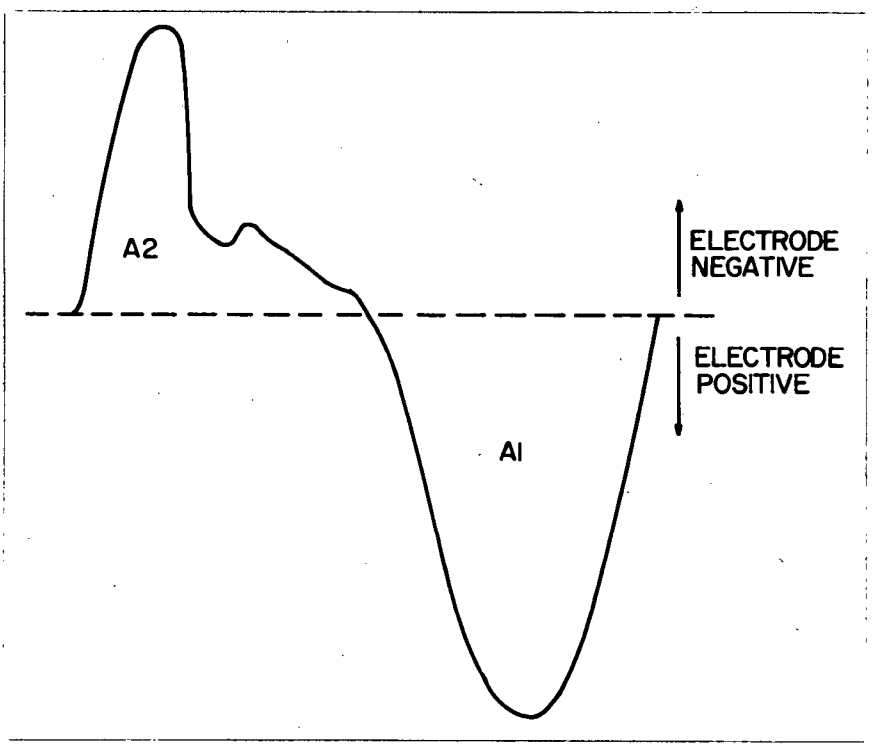

Figure 26 AC Waveform-Mold Current-Run #47 (live mold) (Scope set to trigger on the +ve slope)

It is immediately obvious that different processes are occurring on each half cycle. The precise nature of the processes is not known (but possibly associated with conduction of ions in the frozen slag skin adjacent to the mold wall) and is unimportant as far as this analysis is concerned. However the effects of these processes are important. It is apparent that the areas A1, A2 under the curve of Figure 26 are not equal on each half cycle. In fact, it was found that, using a planimeter, the area A1 under the electrode positive half cycle (i.e. mold and ingot negative) is substantially larger than the corresponding area, A2. Since these areas represent the total number of coulombs passed through the mold wall per half cycle and, since they are not equal, there must be some rectification of the AC current due to passage of some portion of this current through mold wall. The explanation as to how this results in Fe^{2+} production is as follows.

When the electrode was negative, the current through the mold wall was less than when the electrode was positive. However, the mold wall did not carry the total current but rather only some fraction of the total with the balance passing through the ingot. Since the total current passing through the ingot plus mold wall was held constant on each half cycle, it follows that a greater proportion of current was passing through the ingot when the electrode was negative than when it was positive, i.e., the reverse of what we observed at the mold wall. When the electrode was negative and the ingot positive, there was an electrochemical generation of Fe^{2+} at the ingot pool surface.[25] If the same amount of current had passed

through the ingot pool on the other half cycle, one would have expected that the Fe^{2+} generated in the previous 1/120 second would be reduced. However, we have just shown that, due to current rectification at the mold wall, more current passed through the ingot on the Fe^{2+} production cycle (electrode negative, ingot positive) than vice versa. Hence there was a build-up of Fe^{2+} at the ingot pool interface and subsequently in the slag. It is interesting to note that the electrode had the exact same current passing through it per half cycle and thus there was no net electrochemical generation of Fe^{2+} at this site.

In order to assess the ingot pool rate one must accurately determine the current through the mold wall. As stated previously, this was not possible with sufficient reliability to warrant any calculations. In addition, the anodic polarization characteristics of high lime -CaF_2 based slags are not available,[25] without which any Fe^{2+} interface activity calculations are meaningless.

The effect causing the rapid Fe^{2+} build-up after deoxidation, thus, would appear to be due to direct passage of current through the mold wall as in live mold operation and the subsequent rectification of this component of the AC current. In normal AC operation, the varying rates of Fe^{2+} build-up are probably due to different proportions of current leakage through the mold from melt to melt. This leakage would be affected by such factors as slag skin thickness, slag depth and depth of electrode immersion.

The rectification analysis above is consistent also with the conclusions made with respect to the arc induced rectification suspected in Run #37 (4.6.2).

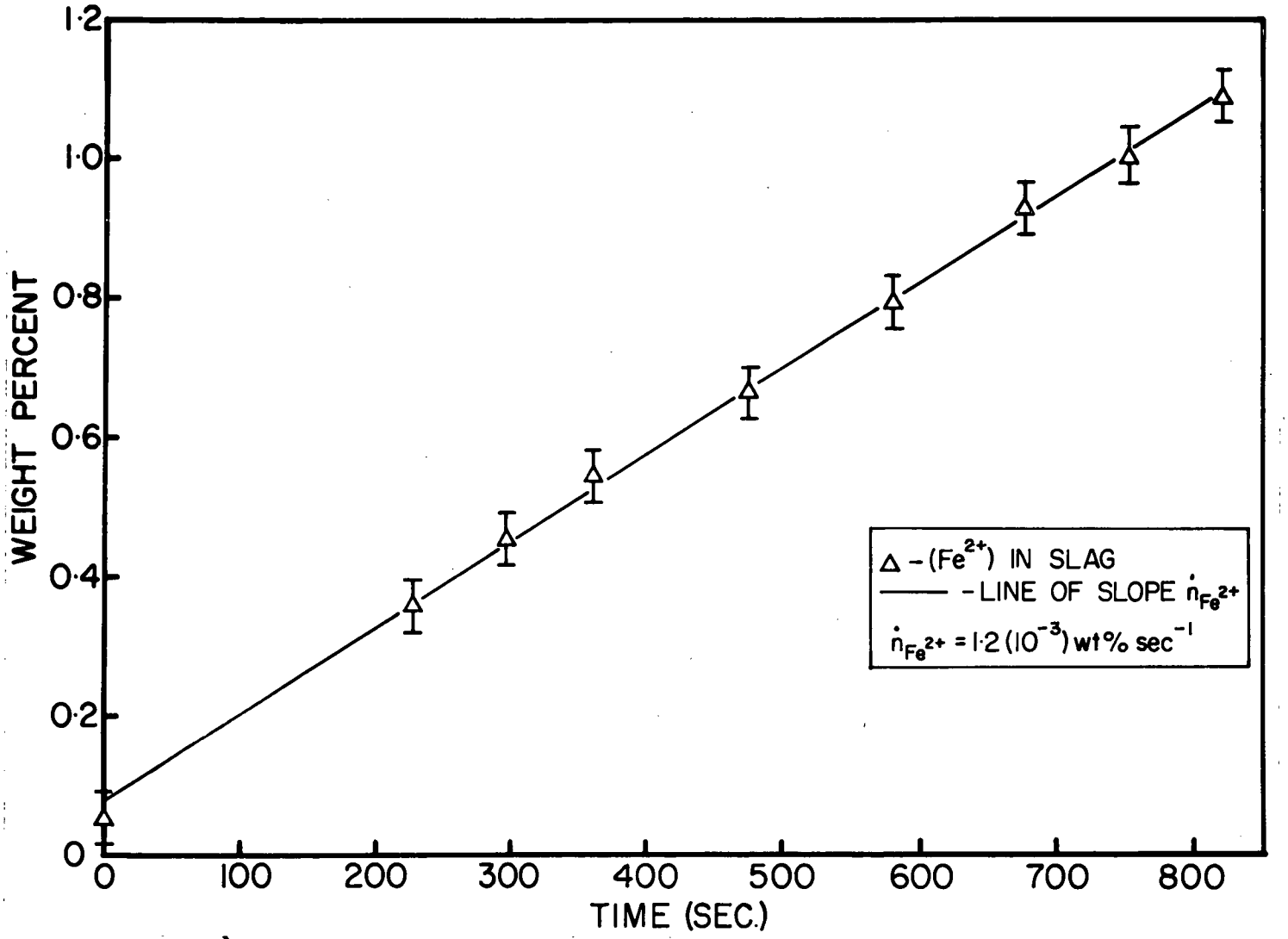

Figure 27 Rate of Rise of Fe^{2+} in Slag when Melting Armco Iron With Live Mold (Melt #59)

In order to establish the reproducibility of the rectification phenomenon, a melt was conducted with relatively pure Armco iron and the live mold configuration. The slag analyses showing the Fe^{2+} build-up occurring during this melt (# 59) are presented in Figure 27. The AC waveform observed on the oscilloscope trace of mold current is shown in Figure 28.

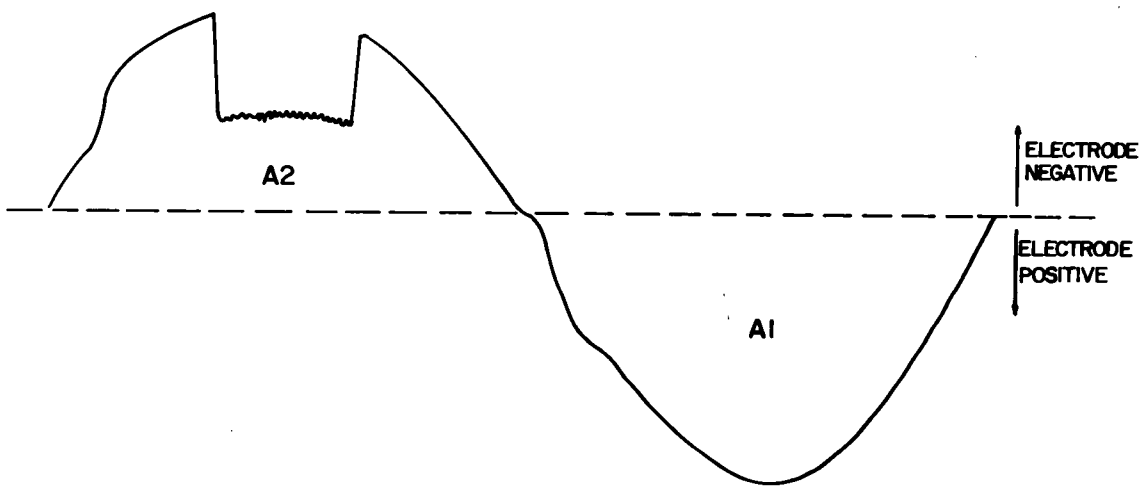

Figure 28 AC Waveform of Mold Current in Armco Live Mold, Run # 59

This waveform, although of different character, shows a similar imbalance between current passed on the opposing half cycles and supports our previous arguments as to the cause of Fe^{2+} generation.

Due to the lower alloy content of the Armco iron, however, the Fe^{2+} continued to increase at a constant rate throughout the course of the run.

As mentioned in Chapter 3, some samples taken in run # 47 were divided up and analyzed for Fe^{2+} and compared to the values obtained for total iron on the same slag samples. There was no detectable difference in the values found by each method and hence, it is likely that there was no Fe^{3+} in these slags under these operating conditions.

4.6.4 Insulated Mold Results

The procedure used in performing the insulated mold experiment # 40 was identical to the unsteady state trials with 1018 of the previous sections. Yet it is evident from Figure 29(a),(b) that the result is not equivalent. The Fe^{2+} level rose only from .08% to 1.2% in 730 seconds. This was a smaller rate of increase (by a factor of $\simeq 5$) than in even the steady state runs of Figures 19, 20. In light of the previous discussion concerning passage of current through the mold wall, it is evident that the boron nitride coating applied to the mold wall has indeed provided a good electrically insulating barrier next to the slag skin. In this case, current flow was restricted to passing only through the electrode tip and the ingot pool surface and the rectification effects observed in the live model case were effectively eliminated. It is suggested that the slight rise in Fe^{2+} concentration may be associated

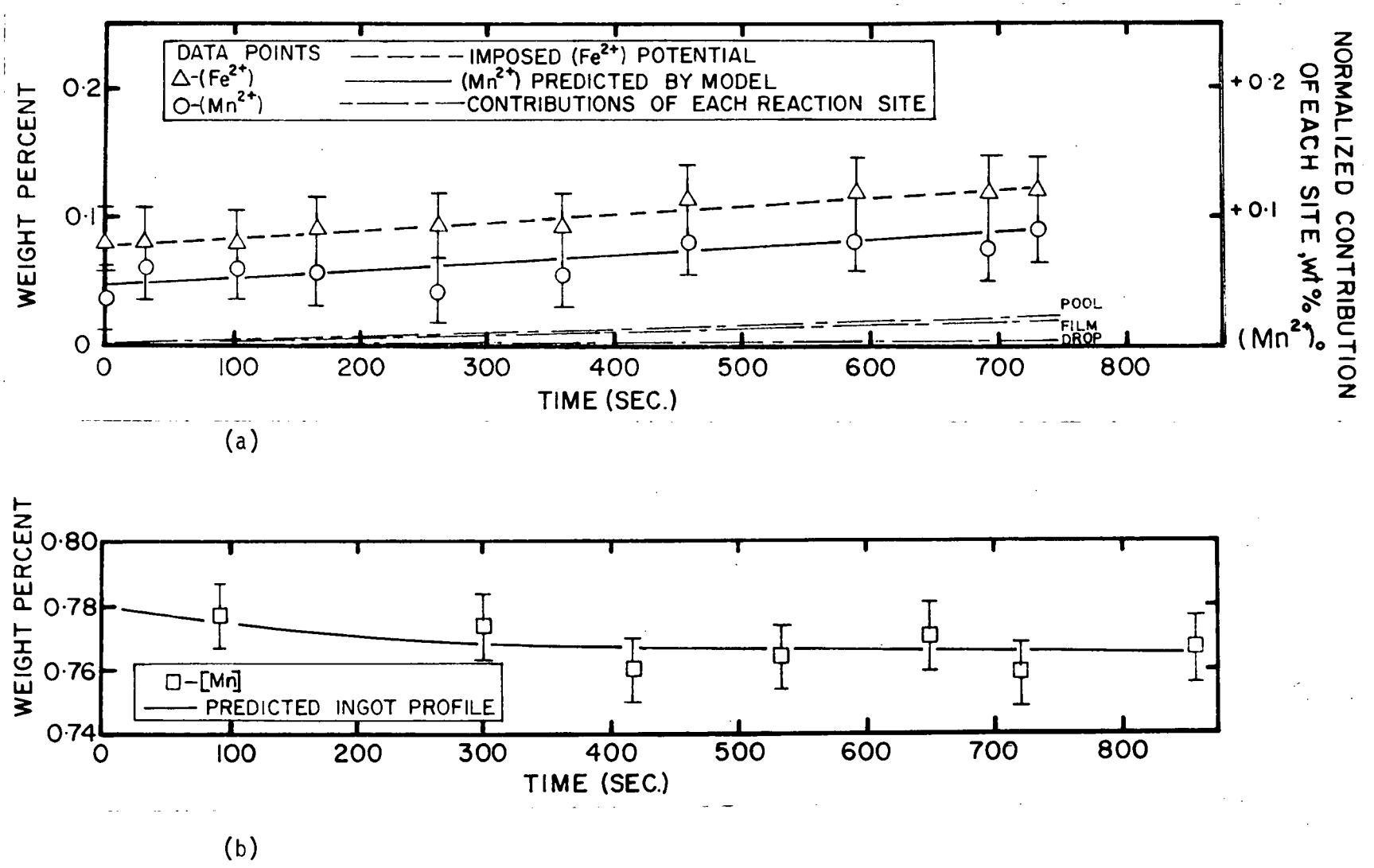

Figure 29 Comparison of Theoretical Mass Transfer Calculations to Experimental Results for Insulated Mold - Melt #40
(a) Slag Composition vs. Time Profile
(b) Ingot Composition vs. Time Profile

with the difference in current densities occurring at the two electroactive poles of the system, the electrode having about 1/3 the area of the ingot.

The predicted composition-time profiles for slag and ingot also agree with the data in this case. However, this instance is the only one so far in which we observe the contribution to mass transfer at film site to be substantially altered from the previous, very consistent behaviour.

All the mathematical modelling so far has been done using the imposed Fe^{2+} potential as indicated by the data for each individual experiment. This device has enabled us to cope with the unknown features of the electrochemical production of Fe^{2+} ions. In the case of the experiment just discussed, we have shown that it is possible to reduce the rate of Fe^{2+} build-up substantially by electrically insulating the inner surface of the mold. Recognizing this feature of the insulated mold, experiments #46, and #58 were designed to test not only the model predictions of [Mn] and (Mn^{2+}) changes but also those of (Fe^{2+}) in the slag. This was done, as previously described (3.8.6), by adding Fe^{2+} as barium ferrite and Mn^{2+} as MnO in Runs #'s 46 and 58 respectively. These experiments were of short duration in order to minimize any extraneous contributions of Fe^{2+} other than that added or produced by chemical reaction.

The predicted and experimental results are in reasonable agreement in both cases as shown in Figure 30(a),(b).

The results are very nearly mirror images of one another, even insofar as the contributions of the reaction sites are concerned,

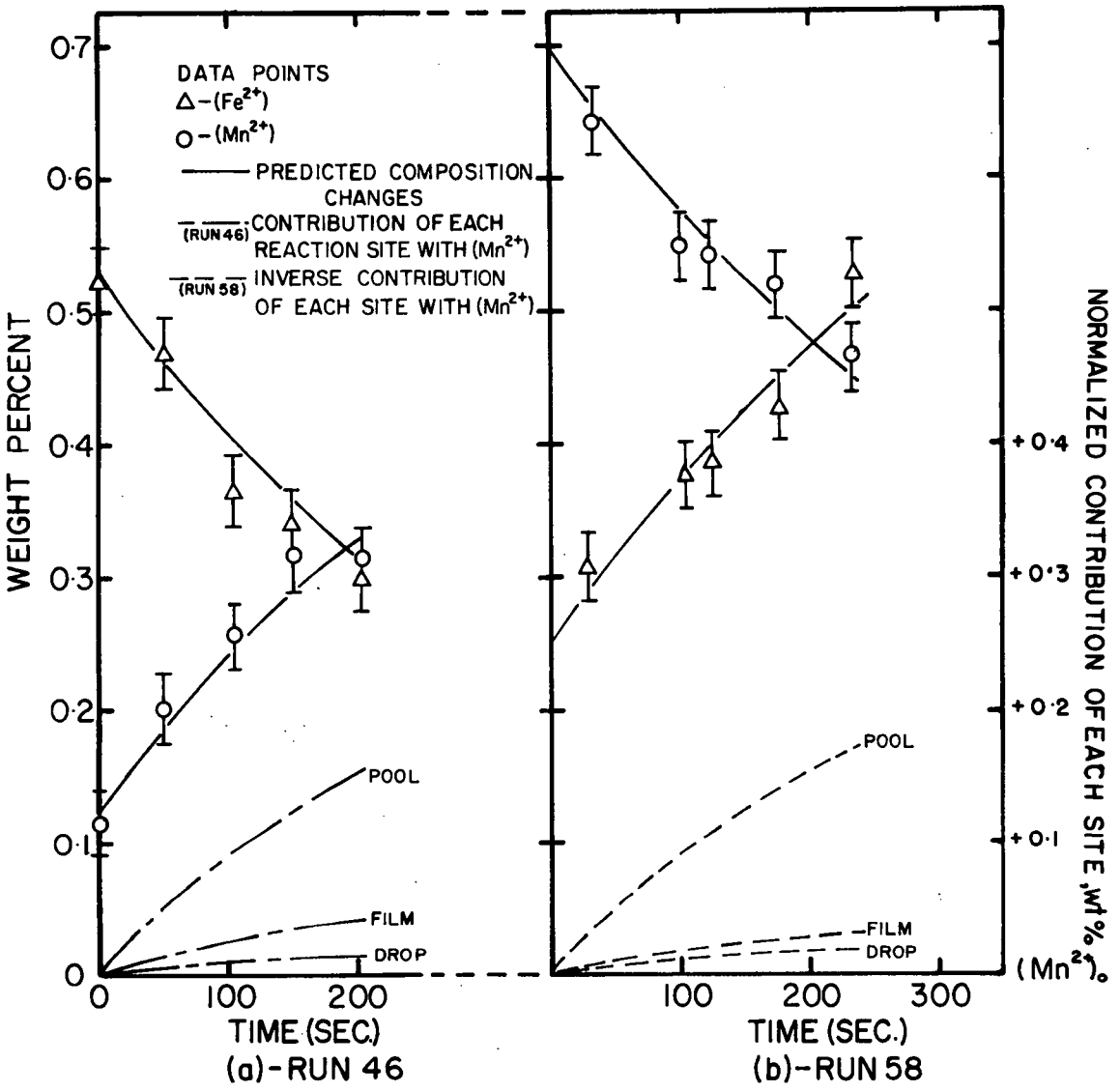

Figure 30 Comparisons of Mass Transfer Model Predictions of Fe^{2+}, Mn^{2+} vs Time with Experimental Composition vs. Time Profiles

thereby confirming the reproducibility of the mass transfer behaviour of the system. Once more it is observed that the ingot pool/slag interface appeared to react more to the stimulus of changing reactant species in the slag than did the other sites.

It appears, then, that the mass transfer model can accurately predict (Fe^{2+}) changes as well as manganese related composition variations under controlled experimental conditions. These runs also demonstrate the precision of the mass balance maintained by the computer model which was not noticeable before.

4.6.5 Results of Steady State Melting in the Absence of Inert Gas Cover

The data and model calculated composition profiles for Run # 50 are presented in Figure 31. It is readily seen that there was a considerable change in the behaviour of the Fe^{2+} content of the slag in comparison with the steady state runs of Figures 19, 20. Since the only difference between the former and present melts was the absence of the inert gas cover in Run # 50 we can attribute this behaviour to the presence of air. The most obvious cause of this difference is the oxidation of the electrode prior to melting.

The rate of Fe^{2+} build-up was of the same order of magnitude as that caused by the apparent rectification effects discussed previously. This observation leads us to the conclusion that both rates, as observed by slag analysis, were controlled by mass transfer rates of Fe^{2+} at respective phase boundaries where Fe^{2+} was generated. Also

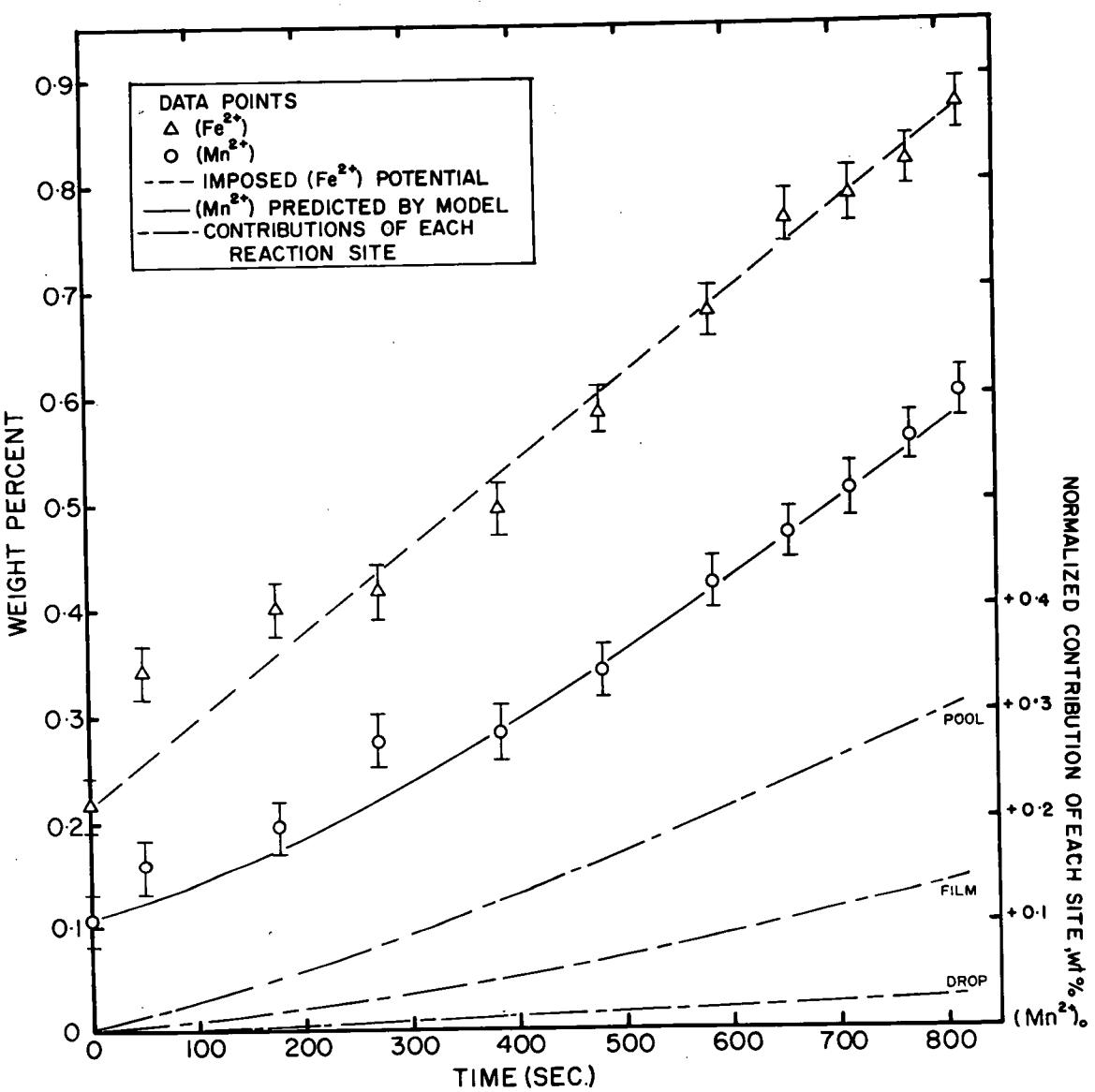

Figure 31 Comparison of Theoretical Mass Transfer Calculations to Slag Composition vs. Time Profile for Melt #50, Performed Without Inert Gas Atmosphere

apparent from this result, is that there is no tendency here for the Fe^{2+} build-up to diminish. On re-examining the unsteady-state runs (Figures 21 through 24), it is observed that, in every case, the Fe^{2+} level at the end of the run had returned to the same level as had been found in the steady state melts; i.e. 0.3% - 0.5%. It would appear, then, that in the absence of air, the electrochemical production of Fe^{2+} adjusted to some level which is relatively consistent. This may be related to the rate of oxidation of manganese as it was noted earlier (4.6.2) that the turnover point in the Fe^{2+} rate appeared to be associated with the maximum rate of (Mn^{2+}) build-up in the slag.

In the presence of O_2 from the air, this apparently did not happen. Certainly the addition of FeO from the electrode oxidation is an important reason for this difference, but the further oxidation of Fe^{2+} to Fe^{3+} may have contributed to the continuation of iron build-up in the slag. In this particular instance, the possible existence of Fe^{3+} was not examined, but such a reaction is known to occur.[53] In large commercial ESR units where the electrode fill ratio (diameter electrode/diameter mold) is about .9 (compared to .5 here) FeO levels in the slag are commonly 0.3 to 0.6 wt %. The area of slag exposed to the atmosphere is proportionately smaller in these larger furnaces, suggesting that any contribution of the Fe^{2+} to Fe^{3+} reaction is reduced and the system behaves more like the inert atmosphere melting situation.

The results, nevertheless, demonstrate the effectiveness of the inert gas cover in reducing overall alloy losses. In addition, the calculated (Mn^{2+}) changes predict the experimentally measured

changes quite reasonably. The predicted contribution of the three reaction sites are also what we might anticipate from previous experience, but there does appear to be a small increase in the mass transfer at the film and drop sites. This was undoubtedly due to the increased driving forces at the higher Fe^{2+} levels

4.6.6 Direct Current Results

Composition changes in direct current melting are generally considered to a direct function of the electrochemical processes occurring at the various electroactive interfaces.[11,25,53,91]

The principal anodic electrochemical reaction occurring in DC ESR processing of an iron base alloy is the corrosion of Fe[25] (Equation 4.7) leading to

$$Fe \rightarrow Fe^{2+} + 2e \qquad (4.7)$$

an Fe^{2+} saturated layer on the anode surface at sufficiently high current densities. The corresponding cathodic reaction for CaF_2 - CaO slags is the deposition of metallic calcium by the faradaic reaction (4.8).

$$Ca^{2+} + 2e \rightarrow Ca \qquad (4.8)$$

The net result of these two reactions is the blocking of the electronegative interface to loss of alloy elements by oxidation due to the zero activity of oxidant of this site. It should, in principle be possible to explain the oxidative loss of alloy elements in terms of

only the electropositive reaction site.

Runs #'s 52 and 53 were carried out in the DC electrode negative and DC electrode positive modes respectively. The experimental data as given in Table IX is presented graphically in Figures 32 and 33. The character of this data is very different from the behaviour we have observed during AC melting.

In the case of the electrode negative melt (Figure 32) the mass transfer model was applied considering only reactions occurring at the ingot pool/slag interface and using the Fe^{2+} potential as derived from the data as was done in the majority of previous cases. The rest of the input parameters were consistent with the AC modelling. The electrode positive run was modelled by reversing the active reaction site from the pool to the electrode film. In both cases the drop reaction was ignored as it appeared to contribute a trivial amount in all the foregoing modelling efforts. The results in each case are as good as were obtained in the AC melts and consistent with the earlier discussion of the blocking of the electronegative reaction site in DC melting.

It is unfortunate that the anodic polarization data for the anodic corrosion of iron in CaF_2 - CaO slags has only been extended to 2 wt % CaO. Without this data we are unable to make any reasonably accurate assessment of the activity of Fe^{2+} at the anodic interface. From the limited data available (Figure 34) we can see that the concentration overvoltages expected for 20% CaO slag would be small, even at relatively high current densities. For the current density, i_0, on the electrode tip of approximately 100 amp cm^{-2}, the estimated over-

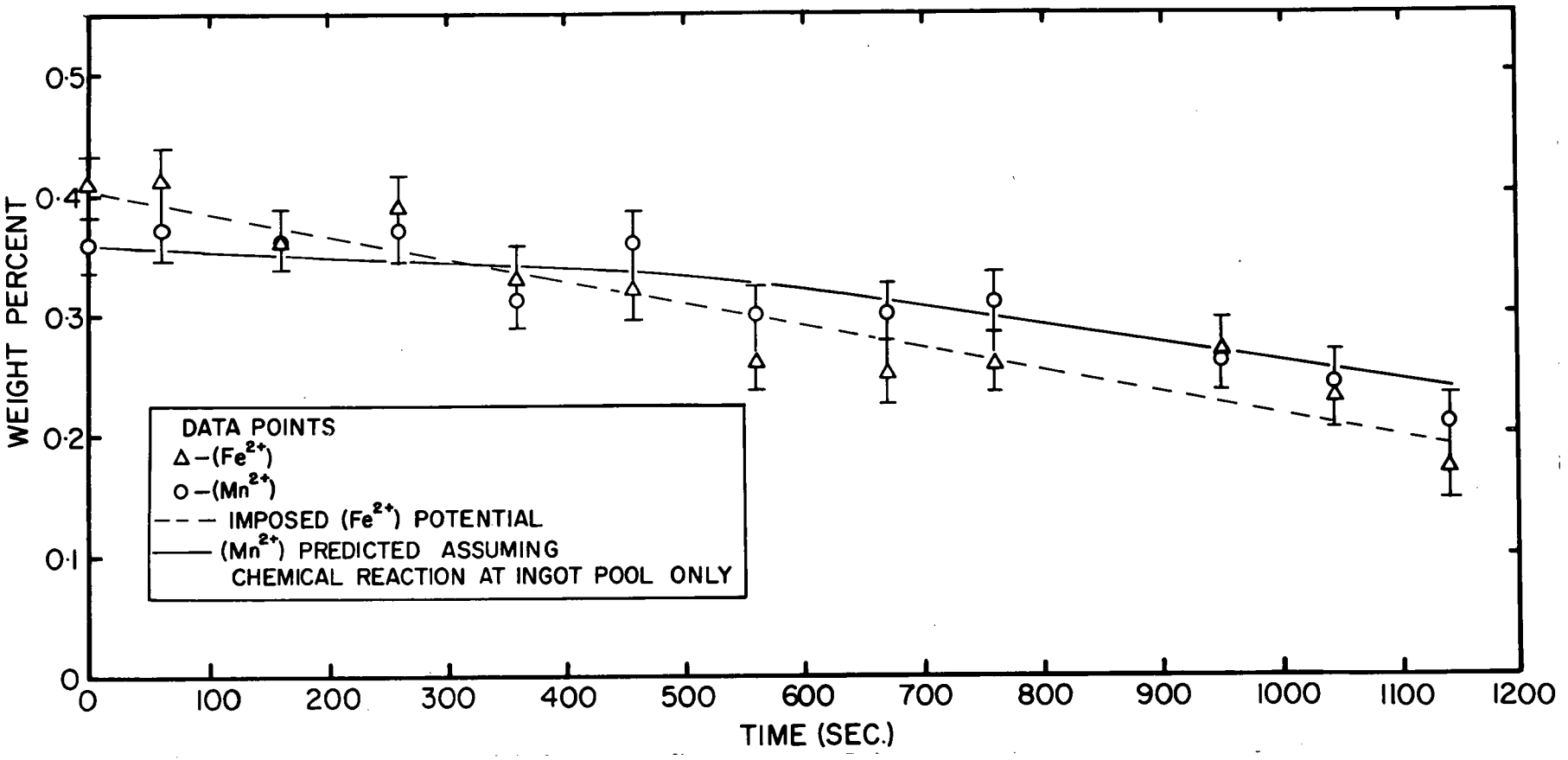

Figure 32 Comparison of Theoretical Mass Transfer Calculations to Slag Composition vs. Time Profile for DC-ve Melt #52

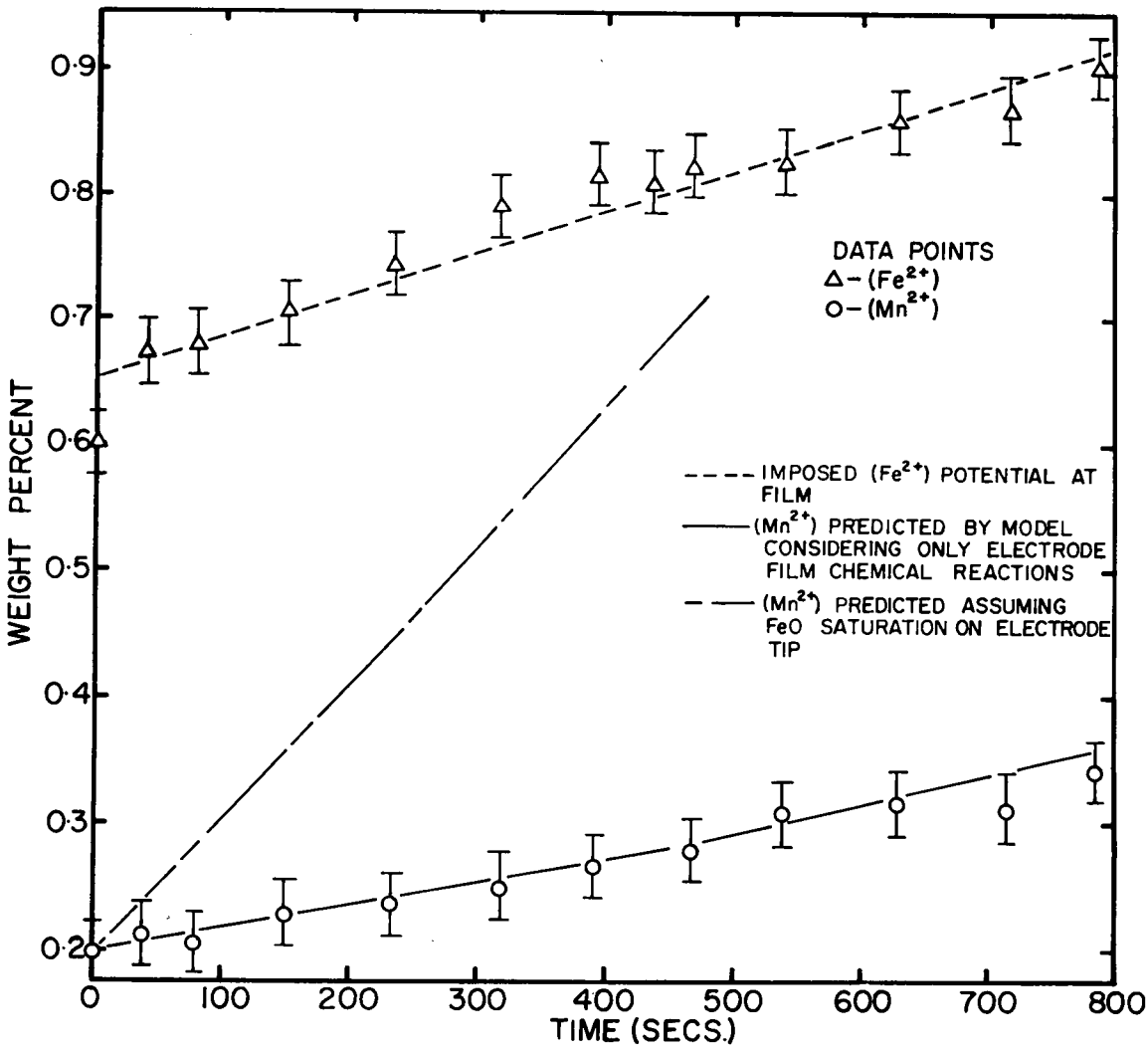

Figure33 Comparison of Theoretical Mass Transfer Calculations to Slag Composition vs. Time Profile for DC+ve Melt #55

voltage would therefore be in the range of 10 to 20 mv. If the knee in the curve for 0.5% CaO represents Fe^{2+} saturation and hence unit activity, it is evident that the activity of Fe^{2+} at the electrode tip in DC + ve melting will be very small. It is therefore suggested that the use of the bulk slag compositions of Fe^{2+} to represent the oxidation potential for the mass transfer process is probably reasonable.

The effect of current density is quite apparent on comparing the two results. The higher current density at the electrode tip (by a factor of $\simeq$ 2) is seen (from Figure 34) to cause a slightly higher level of concentration polarization at this interface for the anodic reaction. Beynon[25] has shown the same to be true for cathodic polarization but also he has demonstrated that a higher limiting current density is required in cathodic polarization to produce saturation. The net result of this on electrode positive was that more Fe^{2+} was being produced at the electrode tip than was being reduced by reaction with calcium metal produced at the ingot pool. Therefore we observe a net increase in bulk Fe^{2+} level.

In the DC -ve run, we observe a lower level of Fe^{2+} in the slag throughout the melt. Also, there is tendency for this level to decrease, although at a lower rate than the rise of Fe^{2+} in the reverse polarity situation. This points up both features of anodic and cathodic polarization mentioned above. Firstly, the current density at the ingot pool was lower leading to a reduced activity of Fe^{2+} at the anodic surface. However, the higher current density at the electrode tip, while increasing the extent of cathodic polarization, did not have as

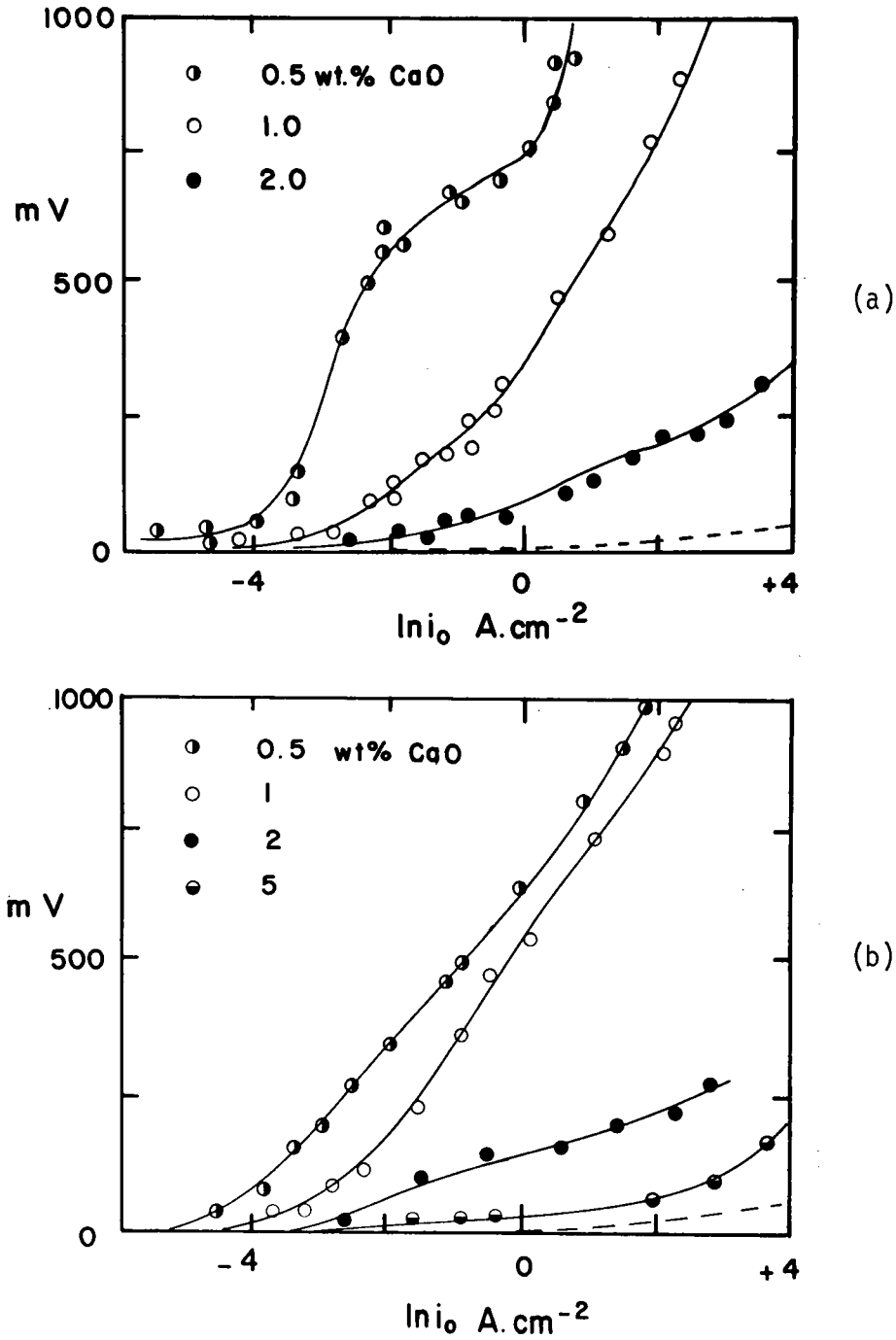

Figure 34 Polarization Characteristics of Iron in CaF_2-CaO Melts.[25] (a) Anodic Polarization Curves. (b) Cathodic Polarization Curves. Dotted line - approximate line for 20 % CaO.

pronounced an effect on the activity of Ca at the interface. Thus, the situation was apparently not completely reversible, providing some rationale for the differences in behaviour between DC + ve and DC - ve melting.

As a matter of interest, the effect of unit activity of Fe^{2+} (total saturation) on the electrode tip on the oxidation of manganese was compared to the results of the experiments in which only local saturation (low activity) of Fe^{2+} was observed. The result shown in Figure 33 is, as anticipated, a greatly enhanced rate of manganese transfer from metal to slag.

It has been shown, then, that DC ESR processing does effectively block the electronegative interface from oxidation reactions and that losses of Mn from the metal may be satisfactorily explained by applying the mass transfer model at the electropositive interface.

CHAPTER 5

DISCUSSION

5.1 Model Parameters

5.1.1 Mass Transfer Coefficients

The accuracy of a mathematical mass transfer model depends critically on the accuracy of the mass transfer coefficients used. In developing the mass transfer model for the ESR process we have tried to use mass transfer coefficients which reflect, as closely as possible, the real physical processes affecting interphase transport. In particular, we have been concerned with the hydrodynamic regimes in the vicinity of each reaction site, this information being gathered from both theoretical considerations (e.g. flow on electrode tip[5]) and direct observation (e.g. slag flow[66]). Consequently, we have been able to justify use of the penetration theory or, some modification of it, in obtaining theoretical estimates of the mass transfer coefficients at each phase boundary.

In addition, the mass transfer coefficients estimated at the ingot pool/slag interface have been investigated experimentally (4.2.1). The results of this work yielded lower values than given by the penetration theory. However, it was felt that a major part of the discrepancy could be accounted for by reduction of Mn^{2+} at the Armco iron electrode tip. Calculation of this loss was accomplished by considering the electrode film in the model to be affected by both (Fe^{2+}) and (Mn^{2+}) potentials as given by Tables IIb for run # 61. The result of

this calculation showed that approximately 6 x 10^{-8} mole $cm^{-3}sec^{-1}$ were lost to the film (Figure 35). In comparison to the rate of rise of (Mn^{2+}) in the slag for Run #60 (Figure 16), there was approximately 9% difference $(\frac{6(10^{-8})}{7.58(10^{-7})} \times 100)$. The experimentally calculated value was thereby corrected to 0.012 cm sec^{-1} which agrees closely with the theoretical value of 0.013 cm sec^{-1}.

Another method of testing the estimates of mass transfer coefficients is to check the consistency of the heat transfer coefficient analogues. The following relation (Reference 39, p. 671) is given for the analogy between heat and mass transfer at low transport rates.

$$h = k_x \rho C_p (\frac{\alpha_h}{D})^{1/2} \text{ cal } cm^{-2}sec^{-1}{}^{\circ}C^{-1} \quad (5.1)$$

where h is a heat transfer coefficient, C_p is heat capacity, α is thermal diffusivity and ρ is the density of the bulk phase. This expression is held to be true in this case since contact times are short (<.5 secs), thereby reducing the effects of reactant depletion during unsteady state diffusion.

If

$$C_p{}^{38} \simeq .2 \text{ cal } gm^{-1}{}^{\circ}C^{-1}; \quad \alpha_h \simeq .02 \text{ } cm^2 \text{ } sec^{-1}; \quad D = 5(10^{-5}) cm^2 sec^{-1}$$

$$\rho_{SLAG} = 2.6 \text{ gm } cm^{-3}; \quad \kappa \simeq 10^{-2} \text{ cal } cm^{-1}{}^{\circ}K^{-1}sec^{-1}{}^{38}$$

then $h \simeq 10\ k_x$. The values of h_S and $k_{Mn^{2+}}$ for the slag phase are given in Table XIV.

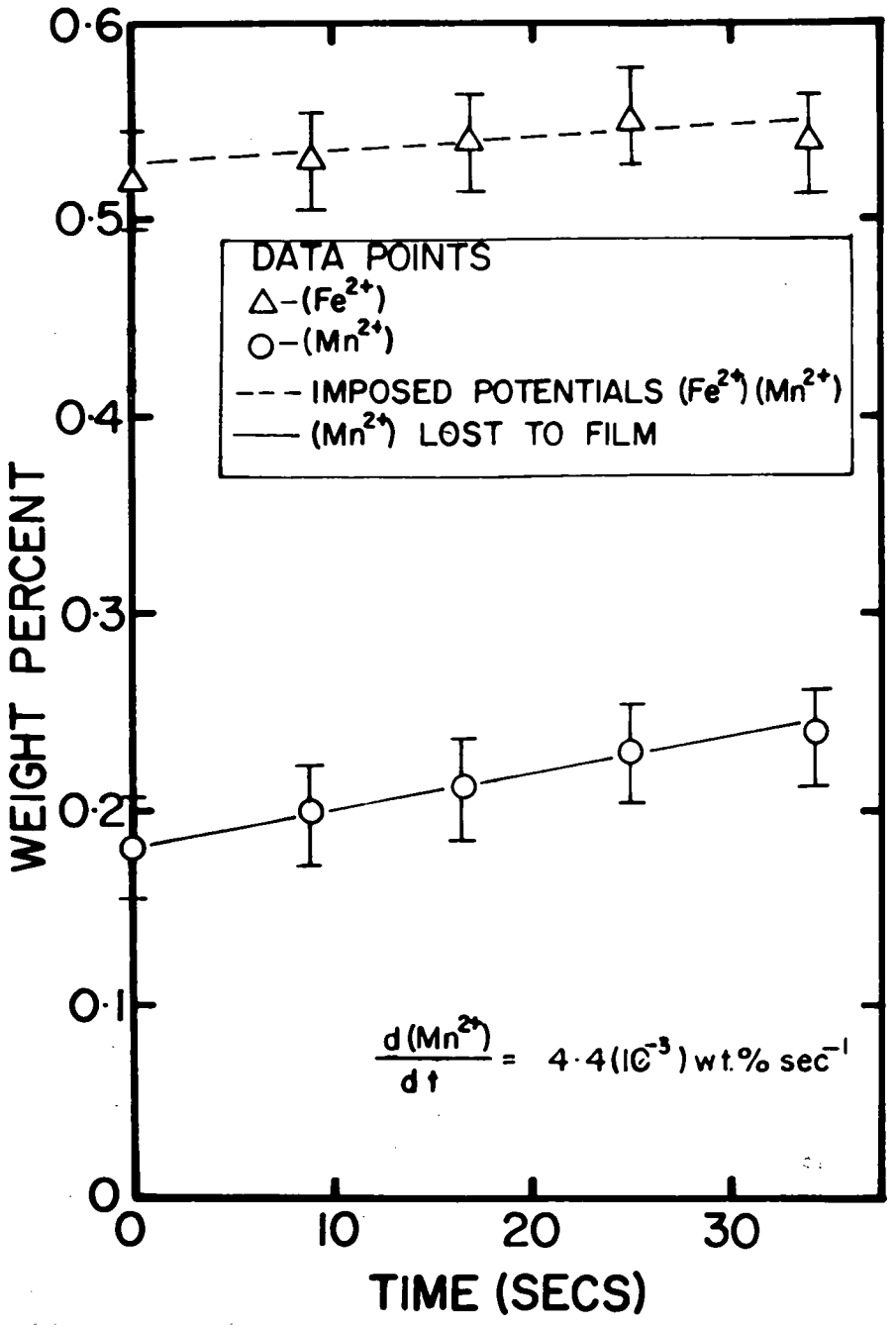

Figure 35 Estimation of (Mn^{2+}) Lost by Reduction at Electrode Tip during Melt #61

TABLE XIV

Heat Transfer Coefficients in Slag at Slag/Liquid Metal Boundaries (as derived from corresponding mass transfer coefficients)

Phase Boundary	$k_{Mn^{2+}}$	h_S
electrode tip/slag	.018	.18
drop/slag	.023	.23
ingot pool/slag	.013	.13

The value of h_S at the electrode tip of .18 cal cm^{-2} sec^{-1} sec^{-1} $°K^{-1}$ is somewhat greater than the value of .07 cal cm^{-2} $sec^{-1}°K^{-1}$ assumed by Mendrykowski[24] et al. in their work on electrode temperature gradients in ESR. Nevertheless, the calculation of superheating of the electrode film (Appendix V.2) shows that very reasonable values were obtained by using the derived value of h_S from Table XIV. In addition, the value of h_S for the pool/slag interface (.13) agrees with the value of .1 cal cm^{-2} $sec^{-1}°K^{-1}$ obtained by Jackson[35] in his study of thermal instabilities in ESR. In Appendix V.3 a calculation is presented showing the temperatures of the falling drop as it passes through slag. The results obtained indicate that each drop will indeed reach the bulk temperature of the slag during drop fall. This had been assumed to happen by other workers but has not previously

been shown to be true.

The heat transfer analogy has, therefore, provided another check on the validity of the theoretical mass transfer coefficients, with the added benefit of verifying some of the previous assumptions currently used in heat transfer modelling.[23,56] To further increase our confidence in the values of these mass transfer coefficients by experimentation would be extremely difficult since this would involve examination in greater detail of the fluid flow patterns. In view of the degree of confidence that we have developed to date in the modelling of the mass transfer coefficients, it is doubtful whether such an investigation would be worthwhile.

It is interesting to examine the effects of changing the mass transfer coefficients by substantial amounts on the predicted concentration changes. In 4.1, an analysis of potential rate controlling steps showed conclusively that transfer of species in the slag phase had the predominant effect. If, in fact, metal phase transport of Mn is unimportant, a large increase in the mass transfer coefficient should not affect the predicted results. This is exactly the case and is demonstrated in Figure 36 (lines B) where we have increased the mass transfer coefficient of k_{Mn} in the metal at each site by 100%. The total change in the predicted (Mn^{2+}) is insignificant for this case. However, on raising the values of $k_{Mn^{2+}}$ by 35%, we observe quite a substantial increase in (Mn^{2+}) as expected. While this change amounts to about 10% it nevertheless passes through a large percentage of the error bars on the data points for (Mn^{2+}).

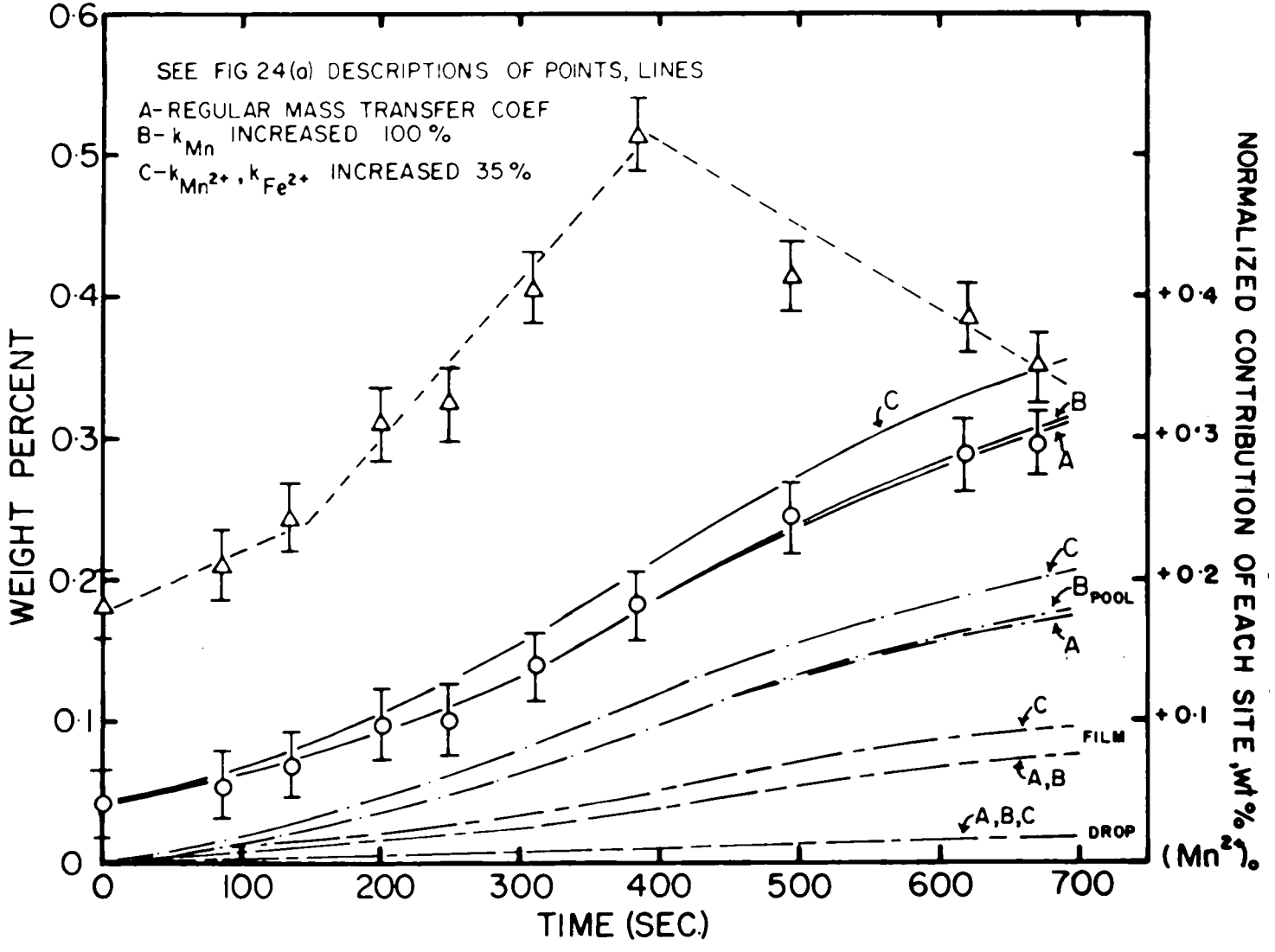

Figure 36 Effects of Varying Mass Transfer Coefficients in Mass Transfer Model on Calculated Slag Composition vs Time Profiles of Run #42

It is important to note that the total change of 10% is less than the change in the mass transfer coefficients.

The theoretical mass transfer model is seen, therefore, to be critically dependent on the values of the mass transfer coefficients. This observation then justifies the prior preoccupation of establishing as much confidence as possible in the modelled values of the mass transfer coefficients. As indicated in 2.3.6, it is likely that overestimates have been used for drop related mass transfer coefficients. In spite of these overestimates, the contribution of the drop to alloy loss remains very small (< 5%). It is probable therefore that a relatively small uncertainty would be introduced by ignoring droplet mass transfer altogether.

It is obvious from a consideration of the penetration model that the major sources of uncertainty in estimating k_{Mn}^{2+} and k_{Fe}^{2+} are the diffusion coefficients and the contact time. The slag flow pattern[5,9,65] and velocity[5,50] of 7-10 cm sec^{-1} have been fairly well established in ESR furnaces up to 20" ϕ. The value of t_e, the contact time, is therefore probably accurate to within ± 10%. However, the diffusion coefficients of Mn^{2+} and Fe^{2+} in the CaF_2 - CaO slag system are virtually unknown and the value of $5(10^{-5})$ cm^2sec^{-1} used is very approximate and the uncertainty conservatively estimated at ± 50%. Fortuitously, k is a function of t_e and D raised to the $-\frac{1}{2}$ and $\frac{1}{2}$ powers respectively. The percentage error in k is then[92]

$$\left(\frac{\delta k}{k} \times 100\right) = \frac{1}{2}\left(\frac{\delta D}{D} \times 100\right) + \frac{1}{2}\left(\frac{\delta t_e}{t_e} \times 100\right)$$

$$= \frac{1}{2}(50 + 10) = 30\% .$$

However, it was shown earlier in this section that this level of uncertainty appears to fall within the error bounds of the experimental data points. Thus ± 30% is an acceptable limit of error in k since a relatively large uncertainty in k is reflected as a smaller effect in the (Mn^{2+}) profiles.

There is a possibility that the mass transfer coefficients may be influenced by spontaneous interfacial motion generated by local changes in interfacial surface tension. It is well known that the surface active solutes, oxygen and sulphur, cause dramatic reductions in interphase surface tension even at relatively low levels and, on a local scale, large surface velocities may be generated.[93] Although this effect has not been directly observed in slag/metal systems, the ESR system is a potential candidate for such occurrences due to the low viscosity of both slag and metal. Also the surface tension of pure iron is known to be in excess of 1800 dym cm^{-1} dropping to levels of ≃ 800 dyn cm^{-1} at several hundred ppm oxygen level. The interfacial tension of iron in a typical ESR system has been estimated at 800 dyn cm^{-1}[18], the low value due probably to the high oxygen ion concentration in the slag. This would tend to reduce the potential effects of mass transfer involving oxygen but not necessarily where desulphurization is occurring. No means have yet been devised to isolate such an effect and therefore we can only anticipate that any increase in surface velocity due to interfacial turbulence would result in higher levels of mass transfer.

5.1.2 Molar Equilibrium Constant

In 2.3.2 it was shown that Ω, the molar equilibrium constant was a function of (a) K, the equilibrium constant for the exchange reaction (2.1); (b) γ_{FeO} and (c) γ_{MnO}. The level of uncertainty in K can be wholly attributed to errors in estimating the temperature of reaction since the expression for K has achieved wide spread acceptance.[34] In Appendix V.2 and V.3, we have demonstrated that the temperatures of 1525°C and 1675°C chosen for the film interface and the pool interface respectively are very reasonable. The error bound is estimated at ± 25°C.

The relative errors in γ_{FeO} and γ_{MnO} are difficult to assess. The value of γ_{FeO} has been evaluated in the CaF_2 - 20% CaO - FeO system[27,36] from a good deal of experimental data and the value is reasonably well established. The estimated values of γ_{MnO}, however, were chosen as that set of values which best fit all of the experimental runs of this work (Figure 18) and although these are consistent with the published values for the system CaF_2 - CaO - MnO at lower levels of CaO (2.3.2) no certain error bound can properly be associated with them. Also we have no idea of the interaction effects of FeO and MnO in CaF_2 - CaO based slags but since they do appear to behave in a similar fashion (large positive deviations decreasing with CaO content[30]) one might anticipate a cooperative effect.

$$\text{Since } \Omega \propto \frac{K\,\gamma_{FeO}}{\gamma_{MnO}}$$

we can estimate the relative contributions of these three factors in the error bound of Ω.

Taking logarithms, we have

$$\ell n\ \Omega = \ell n\ K + \ell n\ \gamma_{FeO} - \ell n\ \gamma_{MnO}$$

$$\ell n\ K = \frac{A'}{T} - B' \text{ (see Equation 2.21) where } A' = 2.303 \times A$$

$$B' = 2.303 \times B$$

$$\text{Therefore } \ln\ \Omega = \frac{A'}{T} - B' + \ell n\ \gamma_{FeO} - \ell n\ \gamma_{MnO}$$

By implicit differentiation we obtain, using the finite difference notation for differentials

$$\frac{\delta\Omega}{\Omega} = -\frac{A'}{T^2}\,\delta T + \frac{\delta\gamma_{FeO}}{\gamma_{FeO}} - \frac{\delta\gamma_{MnO}}{\gamma_{MnO}}$$

To estimate the upper error bound, we must use positive quantities. Since A = 6440 and if T = 1525, δT = 25 then.

$$\frac{A'}{T^2}\,\delta T = .09$$

Multiplying by 100, the error in temperature is seen to contribute ± 9% to the total uncertainty in Ω. It is likely that the uncertainty in γ_{FeO} and γ_{MnO} is at least this large and hence we would anticipate Ω to be accurate to no less than ± ≃ 25%.

However, we assume that our fitted values for γ_{MnO} are reasonably valid as they satisfy a large number of experimental results and are self consistent.

On raising γ_{MnO} by 25% in the input data for modelling Run #42, a profile nearly identical to that of line C in Figure 36 was obtained. As this result was again within the experimental error limits, we can say that even this large uncertainty in Ω will not change the interpretation of the mass transfer modelling results.

Recalling from Chapter I the previous attempts at modelling the ESR system from an equilibrium standpoint, it is easier now to understand the difficulties encountered in such an approach. For example, without the complete thermochemical information concerning the activities of all species in slag and metal one is led to make a number of assumptions. This necessitates use of a somewhat arbitrary equilibrium constant which can lead to puzzling conclusions. The best example of this is shown by the use of different "equilibrium temperatures" for separate reactions[22] occurring in the same system. This problem is not so great in the mass transfer model since we define the interface and hence equilibrium temperatures in advance, thereby leaving only the activities to be sorted out. The greatest aid to resolving this problem is to use as simple a system as possible to reduce the number of species involved. Of course, in this instance the prime objective was to establish that alloy losses in general are mass transfer controlled. It is very evident from the error analysis of the equilibrium constant, Ω, that any large discrepancy in activity coefficients will

have a substantial effect on the predicted alloy losses. This situation is compounded by the addition of more reacting species. Nevertheless, it is felt that the mass transfer model can be used to resolve this problem partially, through iterative calculation of the equilibrium constant as shown by the subroutine OMT (Appendix IV).

5.1.3 Melt Rate

Variation of the melt rate in the electroslag process is known to produce a number of effects in the system as a whole. These effects are all related to the increase in temperature as melt rate increases.[38,56]

The most pronounced difference at high melt rates is an increase in the depth of the liquid metal pool. The related mass transfer effects will include an increased residence time of an element of metal in the molten pool thereby increasing the closeness of approach to slag/metal equilibrium. In addition, the temperature gradients in the pool are altered so that the metal flow may be different. Generally a higher temperature gradient results in high flow rates, but since the gradients are related to pool geometry, it is difficult to assess the exact effect of increasing the pool depth. In any event, we have shown metal phase transfer to be unimportant and therefore the major result of high melt rate for this part of the system will be the increased residence time in the pool.

The higher slag temperatures, which are a necessary prerequisite of high melting rates, will cause some change in the interface temperatures and consequently in the equilibrium constants. It is

anticipated that the major effect would occur at the ingot pool/slag boundary since an increase in melt rate would probably not raise the electrode film temperature appreciably. Temperatures of the order of 1800°C are observed at high melt rates thus reducing the equilibrium constant at the ingot pool surface substantially. This decrease would enhance the likelihood of reversion reactions and might, in fact, reduce the overall alloy losses.

Since higher melt rates are accomplished by passing more current through the system, it is probable that the local slag velocity would be increased. This increased velocity would reduce the time, t_e, used in the penetration theory model for mass transfer coefficients and result in an enhanced mass transfer rate of the slag phase species. Again, this effect tends to bring a closer approach to equilibrium for the ingot pool reactions.

The effect of high melt rates on the electrode tip is actually the converse of the case for the pool. The film thickness will tend to decrease[5] thereby increasing the area to volume ratio. Also an element of molten metal will spend less time on the film. These effects appear to oppose one another and thus it is suggested that the major effect will be due to increased bulk slag flow as above. Other minor changes such as the thinning of the slag skin will occur at high melt rates as well, but these affect mass transfer in a neglible fashion.

In the relatively small ESR furnace used throughout this work, large variations in melt rate are not observed (and, in fact, were avoided $\simeq \pm$ 10% cf. Tables II-IX). However, on large commercial

units variations of up to 50% are readily achieved and, indeed, are necessary for diverse operations such as hot topping and starting. The potential effects of melt rate on mass transfer are, therefore, not apparent in this modelling work but should be readily observed on, say, a 20" ϕ furnace.

5.1.4 Rate of Slag Loss

During the course of an ESR melt, slag is continuously being lost to due formation of a solid crust or slag skin on the mold wall. In the small furnace used here it was not necessary to replace this slag as stable melting conditions could be maintained throughout. It was necessary, therefore, to include this loss (which amounts to up to 30%) in the computer program (Appendix IV). Some variation in slag skin thickness is observed from melt to melt and even over the course of a single melt. To obtain the amount of slag at the start of each experiment it was necessary to back-calculate from the final slag volume to the appropriate initial time. This approach must be taken since a disproportionate and variable amount of slag is lost during starting and switch over to AC from DC.

The effect of slag loss may be observed in the steady state runs #'s 53 and 40. The ingot concentration profiles (Figure 20b and Figure 29b respectively) show a non linear decrease over the course of the run. However, the corresponding slag profiles (Figure 20a, 29a) show a linear rate of rise of Mn^{2+}. This is probably due to the diminishing volume of the slag compensating for the gradual

levelling off of mass transfer rate as a constant concentration of Mn in the ingot is approached. These experiments are rather short and an upward trend in the Mn^{2+} of the slag would be observed at longer times (cf. 5.2.1).

In commercial practice, fresh slag is added at the same rate slag skin is formed. Therefore, in treating this situation one would have to allow for slag freezing out with the current bulk levels of Mn^{2+}, etc., but entering with no Mn^{2+}, etc.

5.2 The Mass Transfer Model

5.2.1 Model Results

As was mentioned in the Introduction, the ESR system is ideally suited to mass transfer analysis primarily due to the progressive, stage-by-stage fashion in which melting and freezing occur. It was also convenient that a number of important parameters such as electrode film thickness, ingot pool volumes and slag flow were known or could be calculated with reasonable certainty. All of these factors have contributed to the success of the proposed model in predicting the observed composition changes of Mn in both slag and ingot. (Figures 19-33) The use of the imposed Fe^{2+} potential has allowed us to proceed in the majority of instances where the sources and/or sinks of Fe^{2+} were not accessible to accurate (or even inaccurate) measurement.

It has been stated repeatedly that the agreement between the predicted and experimental composition changes was good. However, no reference has been made of how one might expect an equilibrium-

type model (such as discussed in 1.3.1) to behave. Figures 37, 38 provide such a comparison.

In Figure 37, the equilibrium model prediction for the (Mn^{2+}) in the slag during normal or steady operation is shown along with mass transfer prediction. The mass transfer prediction was previously shown to agree well with the data (Figure 19) and thus it is evident that the equilibrium predicted line does not. Since the ingot pool is the last contact metal has with the slag, the temperature of the ingot pool/slag interface was used in calculation of the equilibrium temperature in this model. Use of this temperature, however, results in somewhat high prediction. By substantially raising this temperature it would be possible to make the equilibrium fit the data, but we have previously shown (Appendix V.2, V.3) that the temperature of 1675°C is entirely reasonable. This problem, then, is the root of the dilemma faced with the equilibrium model and the cause of the fictitious and sometimes anomalous "equilibrium" temperatures.[21,22]

Although the steady state equilibrium model may be adjusted to coincide with the data, it is doubtful that any amount of temperature adjustment would permit the unsteady state equilibrium modelling attempt in Figure 38 to achieve satisfactory agreement with the data. The shape of the curve is not at all similar to that of the mass transfer prediction and changing the equilibrium temperature could not alter the basic shape. Therefore, it is clear that these unsteady state experiments are a much more realistic test of the mass transfer model than the steady state tests where the changes predicted by either kinetic

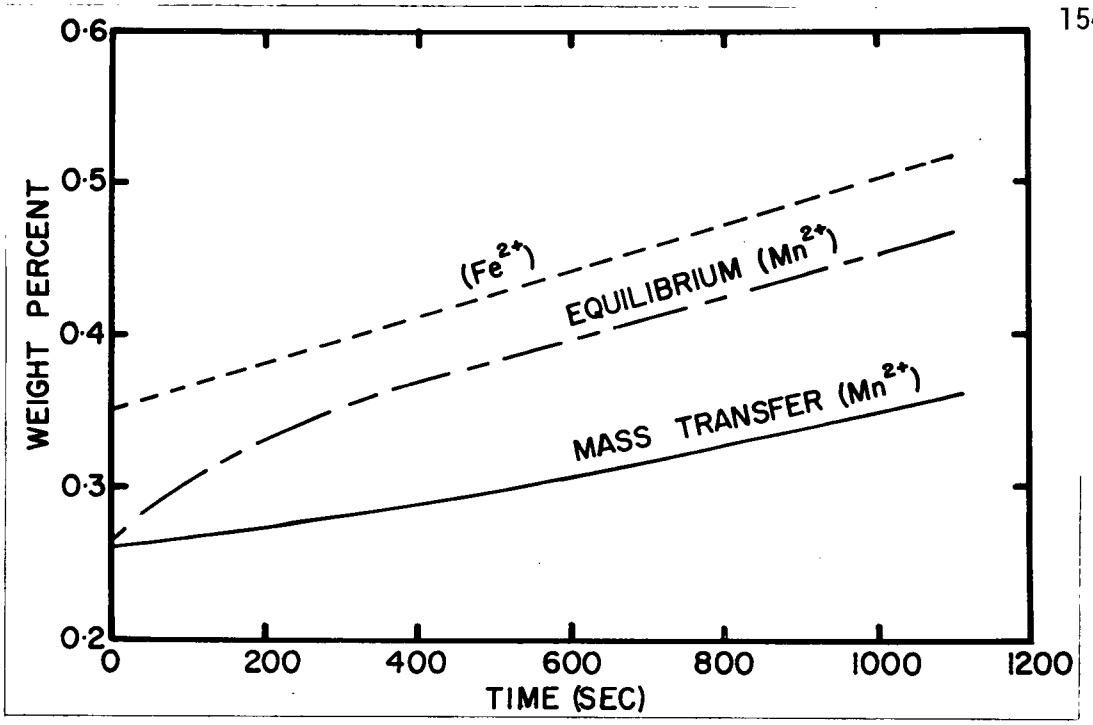

Figure 37 Comparison of Equilibrium and Mass Transfer Model Calculations for Steady State Melt #27

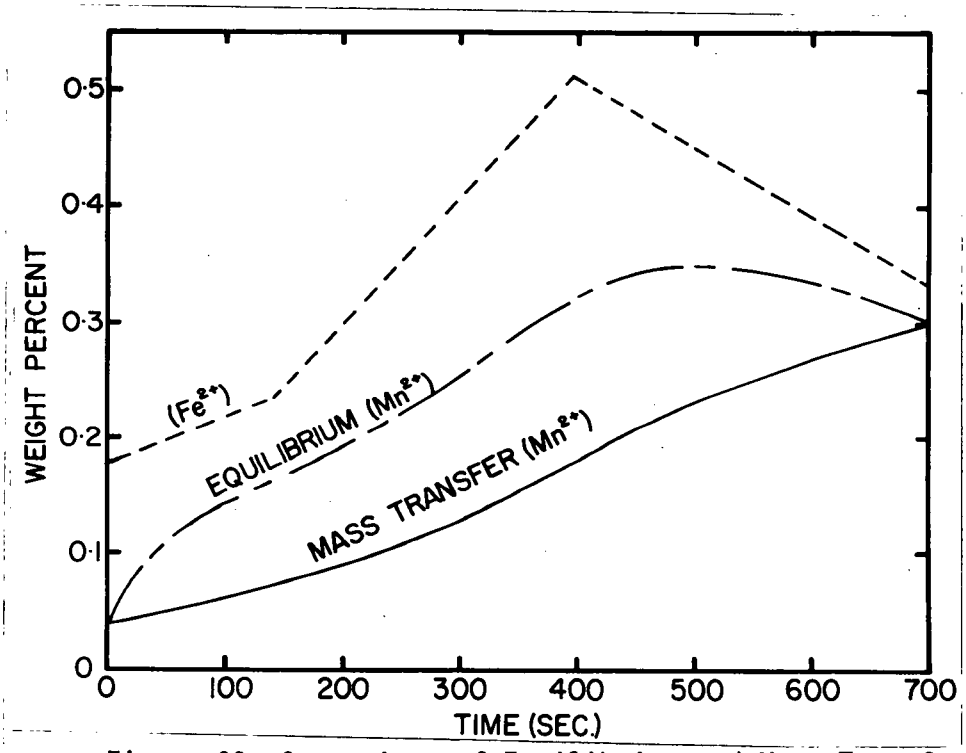

Figure 38 Comparison of Equilibrium and Mass Transfer Model Calculations for Unsteady State Melt #42

or equilibrium model are basically linear. (The transient in Figure 37 is due to the starting point being different from the "equilibrium" composition).

The ability of the mass transfer model to predict successfully the (Mn^{2+}) levels in the slag during DC processing (4.6.6, Figures 32, 33) is another example of the superiority of the mass transfer model in handling the wide range of operating conditions that can occur in ESR processing. These model results also corroborate the results of Beynon[25] who proposed the concept of blocking of the electronegative interface to alloy losses in DC ESR. He was able to infer such behaviour from gross composition differences between ingot and electrode, but lacked any kinetic information on alloy losses. The mass transfer model overcomes this difficulty.

There can be no doubt that manganese losses in the system studied are mass transfer controlled. All the evidence points to a considerable departure from equilibrium type behaviour, as was suspected at the outset. The equilibrium constant of the manganese-iron exchange reaction is quite low and one might well inquire of the situation involving, say, aluminum oxidation where the equilibrium constant is of the order of 10^{12}.

In this case, one or other of the reacting species $(Fe^{2+})_i$ or $[Al]_i$ would tend to zero. Since we have shown that slag phase transport is predominant, it would be reasonable to assume that $(Fe^{2+})_i$ would tend to zero and the driving force for mass transfer of (Fe^{2+}) would be increased. The overall rate, of course, would be strongly affected by

the activity of alumina in the slag. In spite of the increased driving force, it is likely that mass transfer control would still limit the approach to equilibrium. In fact, Boucher[98] has shown that substantial losses of Al do occur even in high Al_2O_3 slags. The true nature of the steady state melting conditions will be discussed shortly, but basically the reason equilibrium cannot be achieved is because of the temperature differences at the two major reaction interfaces (film, pool). In addition, it appears from the work of Knights and Perkins[21] that it was necessary to adopt isothermal temperatures of the order of 1900°C to explain losses of more reactive alloy elements. This is clear evidence of mass transfer control as illustrated earlier in this section.

5.2.2 Solidification Effects

We have totally excluded any effects of solidification phenomena from our model. The only effect of significance to mass transfer is, of course, macrosegregation which is a function of solidification rate, stirring in the liquid metal and the solute under consideration. In fact, the parameter in which we are interested is the distribution coefficient k_0 (ratio of concentrations of solute in solid and liquid at equilibrium) or more properly, the effective distribution coefficient, k_e, where

$$k_e = C_S / C_0$$

C_S being the concentration of solid at any time formed from a liquid of average composition, C_0. k_e is a function of the rate of advancement of the solidification front, the extent of fluid flow and value of k_0

for each particular solute. Chalmers[95] goes through a treatment of these factors on the value of k_e, but his arguments are based on the assumption of a planar interface.

The ESR solidification front is definitely dendritic and thus, we cannot use his arguments. For the solidification of ESR ingots, it has been shown[14,35,56] that k_e is apparently independent of the solute for the purposes of predicting macro segregation, for solutes with k_0 values ranging from .08 for sulphur, to .7 for tin. The value of k_e was invariably found to be in the range of .8. It is considered[56,95] that k_e levels of this order result in very low degrees of macro-segregation in ESR and, thus, our assumptions in regards to ignoring such effects remain valid.

5.3 Model Predictions

We have so far only alluded to the prospects of improving our knowledge of the real nature of the ESR process through use of the predictive aspects of the mass transfer model. It was pointed out in the Introduction and in the discussion of previous modelling efforts that one of the chief drawbacks of the equilibrium and single stage reactor models was their failure to reveal any new information about the process. Since this ability is the essence of successful mathematical modelling, it also is one of the best criteria for evaluating the worth of the modelling exercise.

5.3.1 Relative Contributions of Reaction Interfaces

Accompanying each model calculation in Chapter 4 (Figures 19-31) the contribution of each reaction site to the overall mass transfer effect was plotted. Several important trends were observed from the additional information predicted by the model. Firstly, there was a consistently low and almost negligible contribution($\simeq$ 1%) of the drops to the total alloy loss and this, in spite of our apparent overestimation of the mass transfer coefficients of slag and metal species (2.3.6). Previously, droplets had been the subject of some controversy; on the one hand, the total amount of alloy loss being attributed to mass transfer from the drop[18] and on the other, only a small fraction of the total being considered due to droplet related losses.[10,14] The latter view is in accordance with current findings and is generally accepted although one might express some doubt in the arguments and techniques previously used to arrive at this conclusion. The reason the drop contributes so little is, of course, the extremely short residence time ($\simeq$ .1 sec) in the slag. (Table 1) Droplets are therefore never likely to be of much significance from the mass transfer point of view, even when multiple droplets are falling from large electrodes.

From the heat transfer standpoint, however, we now know that droplets leaving the electrode tip with little superheat do heat up almost to the bulk slag temperature. (Appendix III). This contribution to the sensible heat of the molten ingot pool is of great significance in affecting the geometry of the solidification front and hence the overall ingot quality.[56]

The second important observation made with respect to the contributions of the individual reaction sites was the way in which the electrode film/slag and ingot pool/slag sites reacted to changes in Fe^{2+} in the slag. From run to run the electrode film mass transfer rate appeared to be very nearly constant. Only when there was a great excess of Fe^{2+}, as in the melt in air (Figure 31), did this rate change significantly. Conversely, it was the ingot pool site which reacted to the stimulus of the Fe^{2+} variations and hence the site which determined the individual character of each run.

The reason for this behaviour is similar to that given above for the neglible droplet effects. The residence time of an element of metal on the electrode tip was estimated to be in the order of 1 sec compared to that in the pool of about 80 sec (Table I). However, the short residence time on the electrode tip is partially offset by the extremely high area/volume ratio of the liquid metal ($\simeq$ 100 cm^{-1}) and therefore the overall alloy element loss is significant. The long residence time of a metal element in the pool, on the other hand is tempered somewhat by the much lower area/volume ratio ($\simeq$ .6 cm^{-1}) in this instance. The primary effect, nonetheless, still would seem to the residence time at each site since this ultimately controls the extent of approach to slag/metal equilibrium.

5.3.2 Nature of Steady State Mass Transfer

Probably the most consistently misinterpreted phenomenon related to slag/metal reactions in ESR processing is the steady state operation in which there would appear to be no slag/metal reaction occurring.

Figure 39 is the result of an extrapolation of the model for Run #27 (Figure 19) at constant Fe^{2+}. It is seen that the Mn^{2+} level in the slag approaches a constant value after some 1200 additional secs. Although this constant level has been interpreted previously[21,22] as equilibrium behaviour, it is obvious from the net relative contributions of the film and the pool sites that chemical reaction and mass transfer are occurring at each site. Note again that Mn oxidation at the film is occurring at the same rate as observed in prior runs. The more interesting observation, however, is that the rate of Mn reduction at the higher temperature pool site due to the reversion reaction is very nearly identical to the oxidation rate. Thus, the net rate of Mn loss is virtually zero.

It is also of interest to recall Figure 37, in which an equilibrium model for Run #27 was compared to the mass transfer results. The constant level of Mn^{2+} predicted for constant Fe^{2+} of .5 wt % in Figure 39 is .05% higher than the equilibrium model calculation. This observation confirms the conclusion that steady state is not an equilibrium situation, the higher level of Mn^{2+} in the steady state being due to the balance of mass transfer effects at the different temperatures of the film and pool reaction interfaces.

Reversion reactions may, in fact, produce undesirable effects on the ingot quality. In Figure A5.1 (Appendix V.1), it is clear that, should there be any silica in the slag; the Si/SiO_2 line would rotate anticlockwise. In addition, one might anticipate reduction of silica in the slag by Mn in the metal. This effect would increase with temperature as the Mn/MnO and Si/SiO_2 lines diverge with increasing

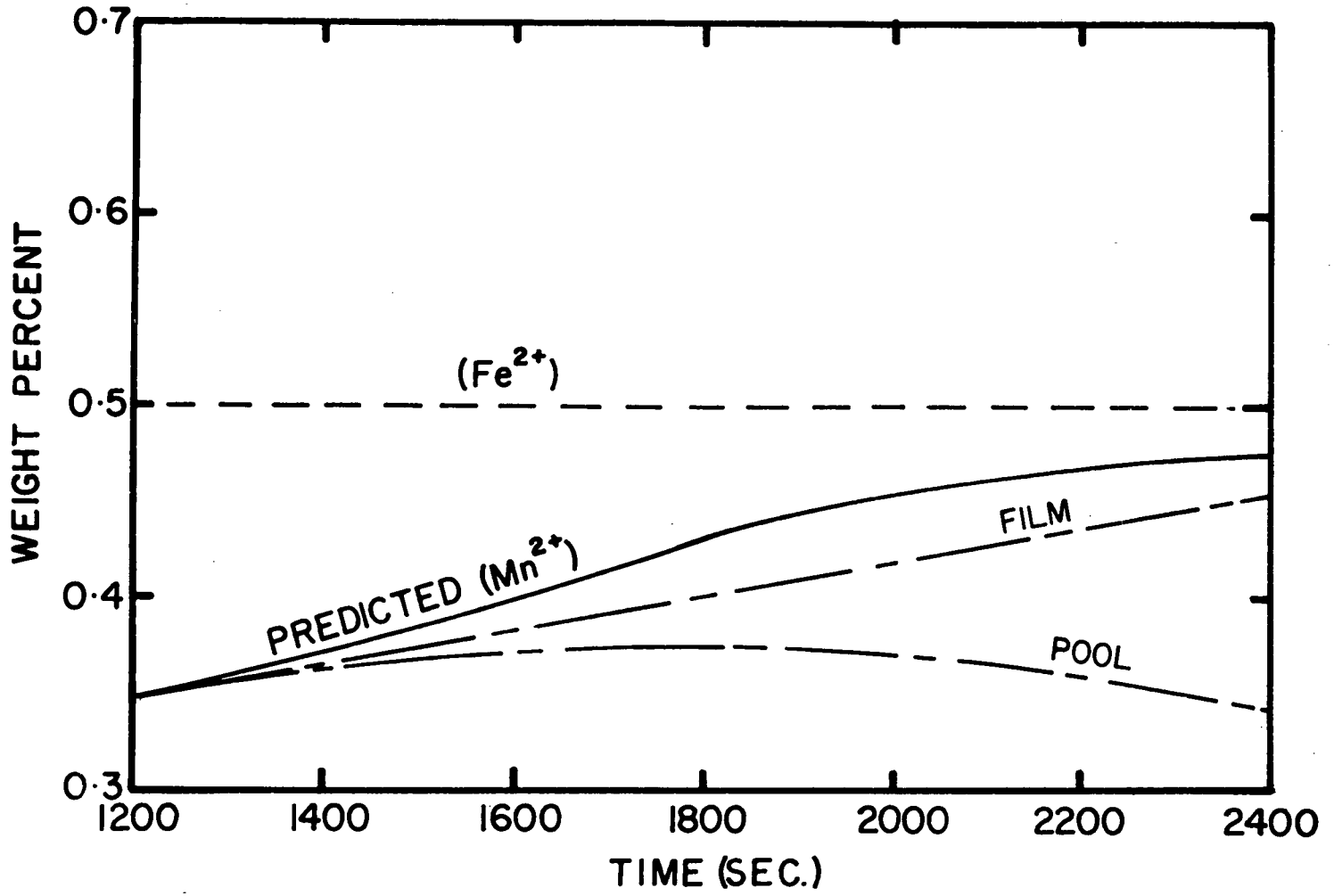

Figure 39 Extrapolation of Theoretical Mass Transfer Predictions for Steady State Melt #27 to 2400 Seconds at Constant Fe^{2+}

temperature. As a result of the reversion reaction putting manganese back into the ingot pool, it is seen that silicon may also revert to the metal in the pool by reduction with manganese. Since silicon is an inclusion forming element and since inclusions are known to precipitate on freezing[94,101] of the metal, it would be possible to introduce inclusions into the ESR ingot. These inclusions may possibly be of a type not found in the electrode.

It is known that the inclusion content of ESR ingots is affected by the slag materials used.[96] In this example we have necessarily dealt with only a simple case of the possible reactions that might occur. In the multicomponent slags used in commercial ESR (e.g. CaF_2 - Al_2O_3 - CaO - MgO - SiO_2 - TiO_2), the likelihood of such reactions leading to inclusion formation is probably increased. Inclusions present in the electrode material may thereby be replaced in the ingot by inclusions bearing elements previously present only in the slag.

5.3.3 Extension of the Model to Combined Manganese and Sulphur Transfer

To date, we have shown that manganese losses are controlled by mass transfer effects and that the model can provide additional useful information about the kinetics of the ESR process. This section will deal with the extension of the model to combined manganese and sulphur transfer. This system has a much lower equilibrium constant (Appendix A.III.2). and has the additional benefit again of known thermochemical data. We have previously evaluated $k_S{}^{2-}$ (4.2.2), the mass transfer coefficient of (S^{2-}) in the slag at the pool site by

both theoretical and experimental methods with satisfactory results. Other values for the mass transfer coefficients may be determined as in Chapter 2.

Cooper et al.[14] have published a very complete set of data (including all the parameters necessary for our mass transfer model) for the melting of AISI 1117 through a CaF_2 - 20% CaO slag. This data is presented in Table XV. In addition to the operating data, complete slag and ingot analyses were given, along with experimentally obtained assessments of the relative rates of desulphurization at the ingot pool, electrode tip and drop sites. It will therefore be a worthwhile exercise to apply the mass transfer model to this system and compare the theoretical predictions to Cooper's data.

The formulation of the mathematical mass transfer relationships for the desulphurization reaction

$$\underline{Mn} + \underline{S} \rightarrow (S^{2-}) + (Mn^{2+})$$

is given in Appendix A.III.2. Although Cooper et al.[14] have only considered the behaviour of S in their paper, Olsen[97] has shown that manganese and sulphur losses are related and therefore desulphurization should be considered as a cooperative phenomenon. Also in Appendix A.III.2, it has been shown that the desulphurization constant of $(S^{2-})(Mn^{2+})$ is greater than that for the couple $(S^{2-})(Fe^{2+})$ and thus the Fe^{2+} level does not enter into this desulphurization reaction.

Cooper et al. used an ESR furnace twice the diameter of the machine considered in all the previous calculations. Therefore, in

addition to the change in reaction species we must introduce some scale-up criteria.

Several of the model parameters may be evaluated directly. We have no reason to assume any different temperatures of the reaction interfaces and thus we shall use 1525°C and 1675°C for the film and pool respectively as before. The electrode diameter of 3" is still small enough to form only single drops. It is well known that the drop size does not vary appreciably with electrode diameter in ESR[2,38] and the increase in melt rate observed is due entirely to the increase in the number of drops formed per unit time. Therefore we can consider that the drop fall time (for similar height of slag bath) and area/volume ratio remain the same as before. The area/volume ratio at the pool is, different, however, but may be easily calculated from Cooper's data on pool volumes. Calculation of the film volume and areas as in 2.3.4 and 2.4 shows that the area/volume ratio remains approximately constant as the increase in volume due to a thicker film compensates for the increase in area. This effect is actually maintained to reasonably large electrode sizes as long as the electrode exhibits a conical tip. The rate of slag loss is easily calculated from Appendix I.3 since the slag skin thickness remains constant ($\simeq$ 1mm) with mold diameter. The number of drops/sec is found as before by dividing the melt rate by average drop weight. This information is summarized in Table XV.

The remainder of the information needed now is the mass transfer coefficient of each species at the three reaction interfaces. A total of twelve parameters are required. The information needed for

the evaluation of the mass transfer coefficients is the diffusion coefficients of sulphur, manganese in both metal and slag phases and the contact times for the penetration theory model. We have already estimated the manganese diffusion coefficients ($D_{Mn,Fe} \simeq 10^{-4}$, $D_{Mn^{2+},SLAG} \simeq 5(10^{-5})$) and the diffusion coefficients of S^{2-} ($D_{S^{2-}} \simeq 10^{-4}$). The value of $D_{S,Fe}$ given by Darken and Gurry is $1.2(10^{-4})cm^2sec^{-1}$. We are left, therefore, to estimate the values of t_e.

Consider first the droplet mass transfer coefficients for S, S^{2-} (k_{Mn}, $k_{Mn^{2+}}$ are given in Table I for the drop and remain the same). Using Equation 2.36 for k_S and $1.2(10^{-4})$ for $D_{S,Fe}$, we have

$$k_{S,DROP} = \left(\frac{4 \times 1.2(10^{-4}) \times 40 \times (1+1.07)}{\pi} \right)^{1/2} = .113$$

Similarly using 2.43 for $k_{S^{2-}}$

$$k_{S^{2-}} = .69 \left(\frac{61(10^{-4})}{\pi \ .88} \right)^{1/2} = .032$$

The rest of the mass transfer coefficients are estimated from the penetration theory as before where

$$k_X = 2 \left(\frac{D_X}{\pi \ t_e} \right)^{1/2}$$

The problem, as mentioned above, is the evaluation of t_e. It is assumed that the slag velocity remains the same at 10 cm sec^{-1} since this value has appeared in the literature for furnaces up to at least 12" in diameter.[50] This result simplifies the problem considerably and we

can, in fact, derive a general formula for $k_{X,SLAG}$ as a function of diameter of electrode or mold diameter, depending on the choice of reaction site. Since t_e is the time taken for an element of slag to pass over the metal surface and if R is the radius of electrode or mold and u is the slag velocity

$$t_e = \frac{R}{u}$$

Since u is constant

$$\frac{(t_e)_1}{(t_e)_2} = \frac{R_1}{R_2}$$

Substituting into the expression for k_X, we have

$$\frac{(k_X)_1}{(k_X)_2} = \frac{2\left(\frac{D_X}{\pi(t_e)_1}\right)^{1/2}}{2\left(\frac{D_X}{\pi(t_e)_2}\right)^{1/2}} = \left(\frac{(t_e)_2}{(t_e)_1}\right)^{1/2} = \left(\frac{R_2}{R_1}\right)^{1/2}$$

or
$$(k_X)_2 = (k_X)_1 \left(\frac{R_1}{R_2}\right)^{1/2} \qquad (5.2)$$

Size effects may be correlated, then, by the square root of the ratio of the radii of the electrode and mold. Thus, for the manganese transfer coefficients, we simply multiply by $(.5)^{1/2}$ or .71 since the electrode and mold are exactly twice as big in Cooper's equipment.[14] It is found, however, on using the expression for t_e (2.29), that the calculated value of .95 sec is identical to the case of the 1 1/2" electrode. This

is due to the higher melt rate in the larger system. $K_{Mn,FILM}$ is the same, therefore, as before.

The sulphur mass transfer coefficients can be obtained directly from the penetration theory using the appropriate values for t_e consistent with the reaction interface under consideration. All of the above information is summarized in Table XV.

The last bit of information needed is the activity coefficient of S^{2-} in CaF_2-20%CaO. From the data of Hawkins et al.,[17] the value of γ_{CaS} of 2.4 is obtained for the level of S^{2-} of $\simeq$ .5% in CaF_2 - 20% CaO slag. γ_{MnO} values were found as previously described.

The computer calculations were carried out using a program similar to that given in Appendix IV and the results were compared to the experimental data of Cooper et al.[14] for sulphur loss (There is no data for Mn) (Figure 40). It is evident that there is very reasonable agreement here between the experimental and calculated sulphur levels in both ingot and slag. The predicted results for the ingot do, however, appear to be slightly high. The reason for this is probably due to the fact that the experiments were carried out open to the air and a certain amount of sulphur was lost to the air. The model does not take this into account. The predictions are, nevertheless, consisted with melting under inert atmosphere as one would anticipate a lesser degree of desulphurization than the system is open to air.

The main purpose of the experimental work,[14] as pointed out in the introduction, was to investigate the nature of the reaction sites in ESR. Consequently, rates of sulphur loss at the electrode film and at the ingot pool surface were measured experimentally using

TABLE XV

Summary of Data for Modelling

Combined Mn, S Losses

Parameter	Film	Pool	Drop
k_{Mn} ($cm\ sec^{-1}$)	.012	.011	.112
k_{Mn}^{2+}	.013	.009	.023
k_S	.020	.014	.113
k_S^{2-}	.012	.013	.032
$V(cm^3)$	.53	800	.35
$A/V(cm^{-1})$	100	.19	24
Volume of Slag (cm^3) -Rate of loss	1456 $-.2(cm^3 sec^{-1})$	melt Rate ($gm\ sec^{-1}$)	13.7
Slag Type	CaF_2-20%CaO	Electrode ϕ (inches)	3
Electrode Analysis	1.34%Mn .154%S	Mold ϕ (inches)	6

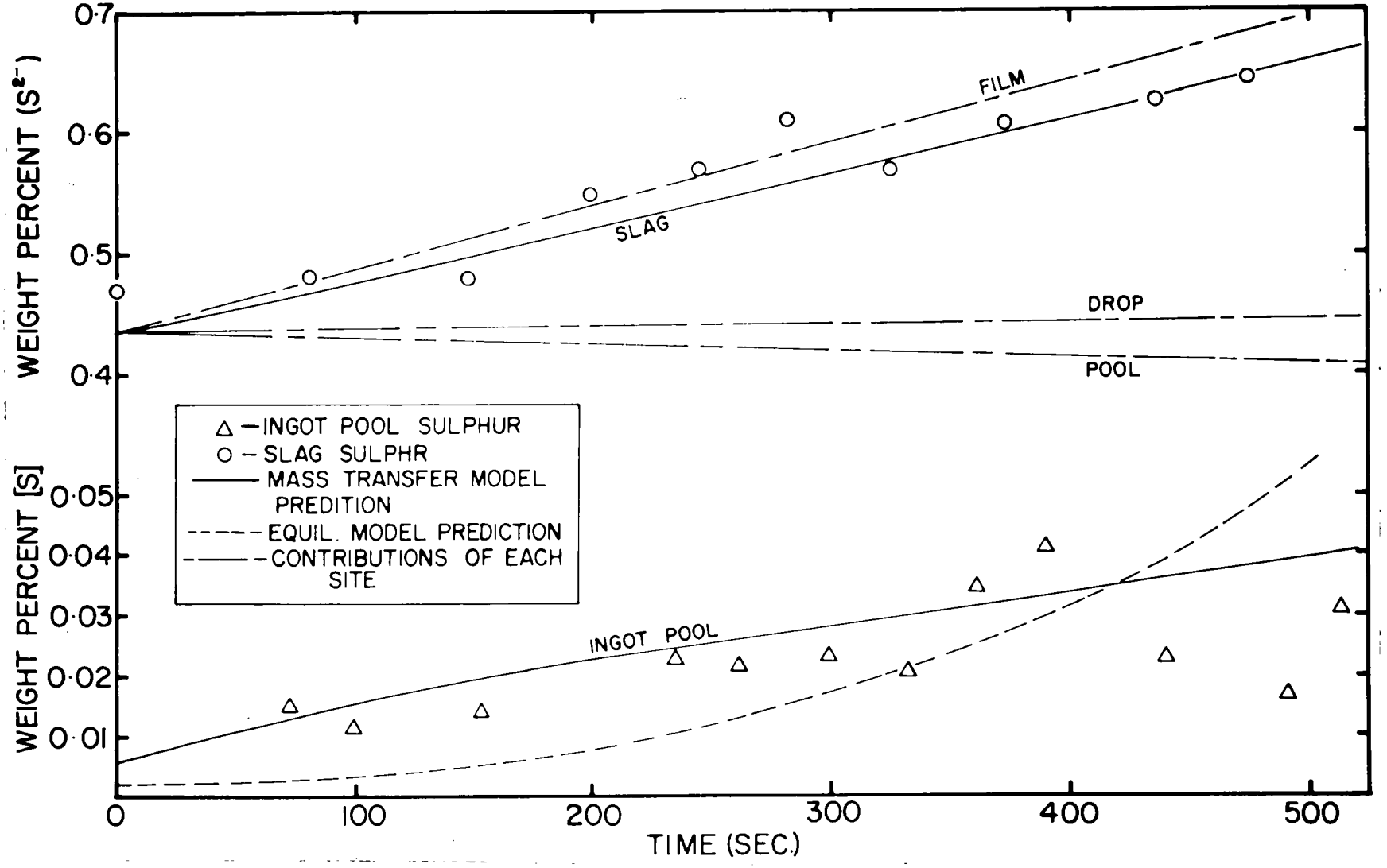

Figure 40 Comparison of Theoretical Mass Transfer Model Calculations to Ingot and Slag Sulphur vs. Time Profiles Obtained by Cooper et al.[14]

a technique involving catching the falling drops.

The rate of desulphurization found by Cooper et al. at the electrode tip was 1.8 (10^{-2}) gms sec^{-1}. From the slope of the line for the film contribution to overall mass transfer, we find that the mass transfer model predicts a rate of 1.9 (10^{-2}) gms sec^{-1}. There is very good agreement between the two values. However, the rate of loss of the pool site, as calculated from the experimental evidence is -1.1 (10^{-3}) gm sec^{-1} whereas the mass transfer model predicts a reversion reaction with a rate of 2.1 (10^{-3}) gm sec^{-1}. This difference by a factor of two may be ascribed to the loss of sulphur to the atmosphere in the experiments. The assessment of reaction with air was considered by Cooper to be extremely inaccurate and thus we cannot make any quantitative statements regarding the differences in the reversion rates. In both cases the contribution of the drops to the overall effect was found to be trivial.

The results of this modelling exercise and the apparent success of the model in interpreting the nature of the mass transfer phenomena at the various reaction sites is very encouraging. The impact of these results is even greater when one considers that we have changed not only the chemical reaction involved, but also the size of the furnace. Since results for desulphurization of a similar steel are available for a very small ESR unit,[99] namely 16 mm ϕ, it is extremely interesting to extend our model to, say, a 20" ϕ unit (510 mm) and then compare the extent of desulphurization over this wide range of ESR processing equipment.

5.3.4 Scale-Up Predictions

The choice of a 510 mm ϕ ESR unit was based on the popularity of this size of commercial unit and therefore the availability of data such as melt rates, pool volumes, etc. The following procedures were used to estimate some of unknown physical parameters.

The fill ratio of larger ESR furnaces is of the order of .9. The electrode diameter was therefore taken to be 460 mm. This size of electrode is observed to melt by forming a liquid metal film approaching 1000 microns thick. Although it retains the conical shape, the effect is less pronounced and metal is observed to leave the electrode by formation of droplets at a number of points. Calculation of the area/volume ratio gave a value similar to that used in the previous examples. Examination of an electrode tip of this size shows that the drop site density is about one for every 45 - 50 sq. cm of electrode surface area. For the electrode under consideration (Area $\simeq$ 1660 cm^2), there would then be about 35 drop sites. Since the drops are known to be approximately the same size regardless of electrode tip dimensions,[2,38] we would expect about 50 drops/sec for a melt rate of 150 gm/sec (1200 lbs/hr). The residence time of any element of metal on the electrode tip was then estimated by dividing the number of drop sites into the number of drop per sec. This procecure resulted in a residence time of about 1.4 sec.

The ingot pool was assumed to be hemispherical[38] and the resultant volume of molten metal was approximately 35,400 cm^3. The area to volume ratio was therefore .06 cm^{-1}. The quantity of slag present was calculated by assuming the typical slag bath depth of 5

inches and the result was 25,950 cm^3. Also, since slag skin thickness is relatively constant for a particular slag regardless of furnace size, we calculated a rate of slag loss of about .7 cm^3 sec^{-1}.

The mass transfer coefficients in the slag phase were found with the aid of relation (5.2), where

$$(k_x)_2 = (k_x)_1 \times (R_1/R_2)^{1/2}$$

For $R_1 = 6$, $R_2 = 20$, the conversion factor for $k_{Mn}2+$, k_S2- at the ingot pool/slag boundary was .54 and for $R_1 = 3$ and $R_2 = 18$ at the electrode tip, the slag transfer coefficients conversion factor was .41. The drop mass transfer coefficients remained the same as before and remaining metal phase coefficients were calculated from the local residence times. We assumed here that the flow regimes in the slag and metal did not change substantially with the increase in size. All of the above data necessary for the scale-up modelling is summarized in Table XVI.

The results of the mass transfer model calculations are presented in Figure 41, being plotted as ingot sulphur by electrode sulphur level vs time. There is a very definite trend from the 16 mm to the 510 mm diameter furnace and this trend is an enhancement of desulphurization with increasing size. This result cannot be attributed to increased mass transfer rates since a comparison of Tables I and XVI shows that the mass transfer coefficients are generally lower for the larger units. The decrease in area/volume ratio at the ingot pool/slag boundary would also appear to contradict the observed trend. However,

TABLE XVI

Summary of Data Used in Scale-up Modelling of

510 mm ϕ ESR Furnace

Parameter	Film	Pool	Drop
k_{Mn} (cm sec^{-1})	.005	.006	.112
k_{Mn}^{2+}	.010	.007	.023
k_S	.008	.008	.113
k_S^{2-}	.010	.010	.032
V (cm^3)	19.1	35400	.35
A/V (cm^{-1})	100	.06	24
Volume of Slag -Rate of loss	25950 cm^3 -.7 cm^3 sec^{-1}	melt rate (gm sec^{-1})	150
Slag Type	CaF_2-20%CaO	Electrode diameter (mm)	460
Electrode Analysis	1.34%Mn .154%S	Mold diameter (mm)	510

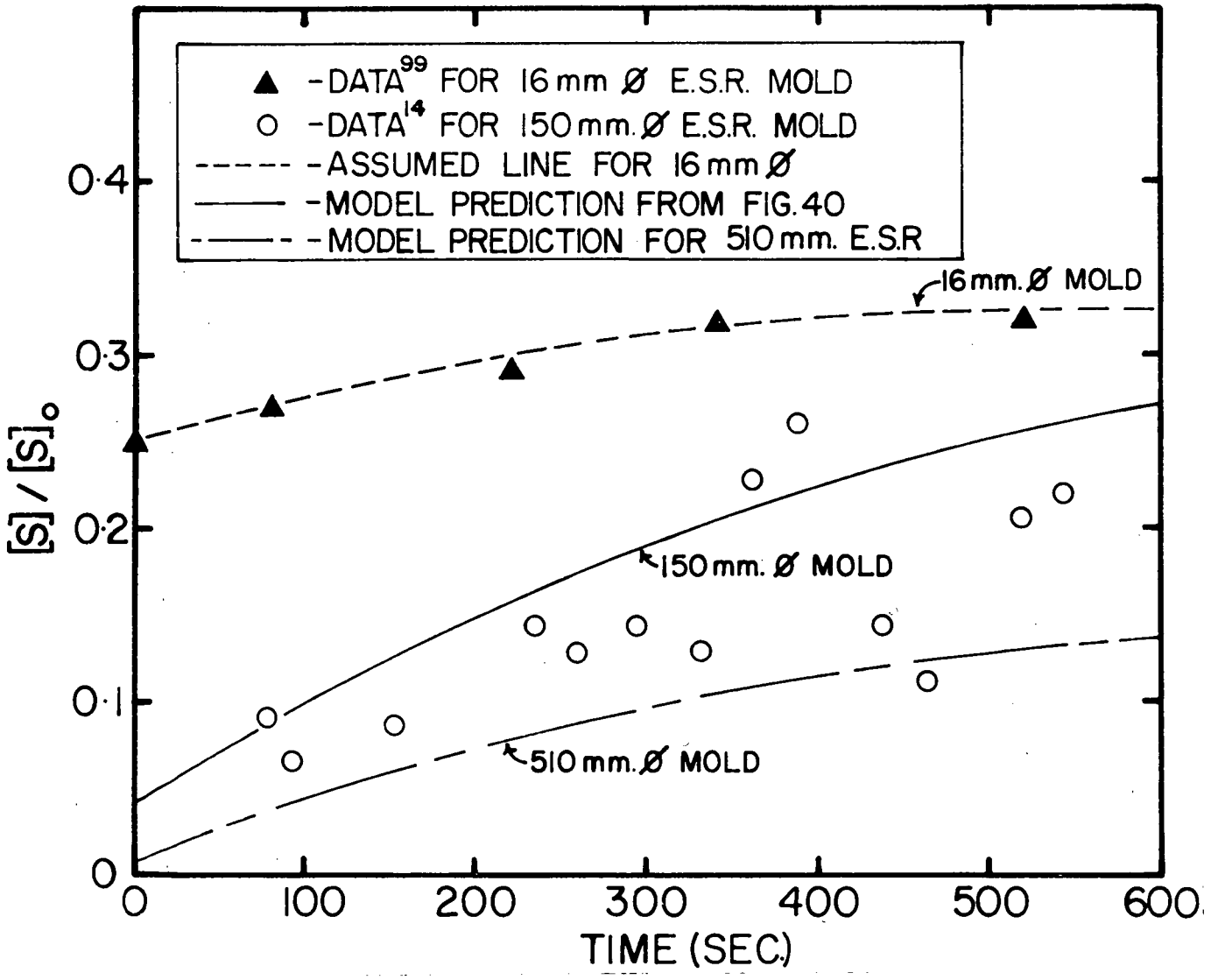

Figure 41 Effect of ESR Furnace Size on Desulphurization Characteristics of the ESR Process

on recalling the reaction occurring at this particular site, we find that it is most likely to be a reversion reaction (5.3.3).

Therefore, the effect of decreasing the area/volume ratio in the mass transfer equation is to limit the effect of the reversion reaction.

It was also pointed out earlier in this section that the residence time of an element of metal on the electrode tip was about one and half times greater in the largest unit compared to the 150 mm (6") unit. This residence time led to an increase in the amount of desulphurization occurring at this stage. Thus, this argument and the one preceding at least partly explain the observed results.

The model appears to be adaptable to use in scale up predictions. The desulphurization levels of 81% (.134 - .025%) for the 16 mm ϕ mold and 89% (.154 - .034%) for the 150 mm ϕ mold are consistent with unpublished work at U.B.C. showing that 84% (.256 - .040%) is obtained in a 76 mm furnace. However, all of the above work was done with very high lime slags which have an unusually high capacity for sulphur. Nevertheless, removal efficiencies of 40 - 70% are reported in remelting steels of low initial sulphur levels (.007% - .037% respectively) in large ESR furnaces (1480 x 640 mm $\simeq$ 40 tons) using complex, multicomponent slags.[100] This level of desulphurization observed in large units tends to confirm our model calculations for the 510 mm mold.

An additional aspect of electroslag remelting in reasonably large units (>150 mm ϕ x 1 metre high) is the change in pool volume during the course of a melt. A typical example of this is shown in

Figure 42. The increase in pool volume as the ingot grows is caused by the greater separation of the heat source (slag bath) and the predominant heat sink which is the base plate. The mold walls, however, exert a stronger effect as the ingot grows thereby increasing the radial heat flow component.

This pool volume growth in large ingot manufacture might be expected to exert some influence on the mass transfer characteristics of the ingot pool/slag interface since the residence time of an element of metal in the pool is directly proportional to the pool volume and inversely proportional to the melt rate (at steady state). Generally, however, commercial ESR units are operated on the basis of constant melt rate. Therefore, the residence time will progressively increase with ingot height, thereby tending to enhance alloy losses (assuming no reversion reaction). On the other hand, the area/volume ratio will be decreased at larger pool volumes offsetting somewhat the increase in residence time. Thus, at constant melt rate, one might anticipate little or no effect of the increasing pool volume on the pattern of alloy losses during ingot production. That this is so is demonstrated in Figure 43 in which is observed the familiar transient culminating in steady state behaviour for the axial distribution of carbon in a 14 ton ingot. Although the final, steady state level of carbon in this ingot was influenced by the effects of increasing pool volume, the overall behaviour is consistent with our prior observations in other systems.

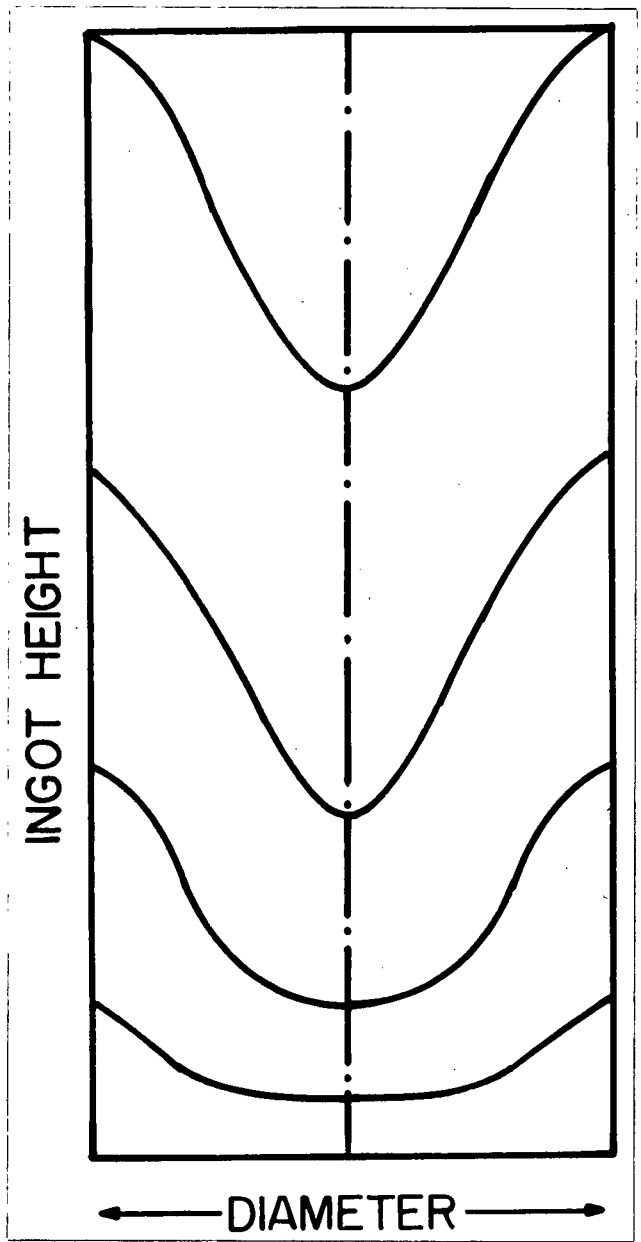

Figure 42 Pool Geometry as a Function of Ingot Height in a Large ESR Furnace (102)

It is interesting to speculate briefly on some other aspects of large ingot manufacture. The melting program generally followed in very large ESR operations (>100 tons) is to melt initially at an abnormally high rate to build up a deep liquid metal pool. Since such ingots are often not much taller than twice the mold diameter, this liquid metal pool may comprise 50% or more of the ingot up to the halfway point. High melt rates as mentioned previously (5.1.3) may result in enhanced slag mass transfer coefficients due to, say, an increase in the slag velocity. It is likely, however, that the increased temperature at the ingot pool/slag interface, resulting from the higher bulk slag temperatures necessary to sustain high melt rates, would have the major effect by increasing the likelihood of reversion reactions. This, in turn, will result in more reduction of potential inclusion forming elements from the slag into the ingot pool, this effect again being assisted by the higher temperatures (5.3.2). Lower alloy losses may be achieved but at the expense of an increase in inclusion content.

The process of completing the upper portion of the ingot may be considered simply as a hot topping operation wherein the power is gradually reduced, cooling the system slowly and maintaining good ingot structure. At these lower melt rates, however, one can anticipate higher alloy losses, but lower inclusion levels by using the converse of the above arguments. Some evidence of the validity of this speculation is to be found in the literature. Myzetsky et al.[104] show that sulphur

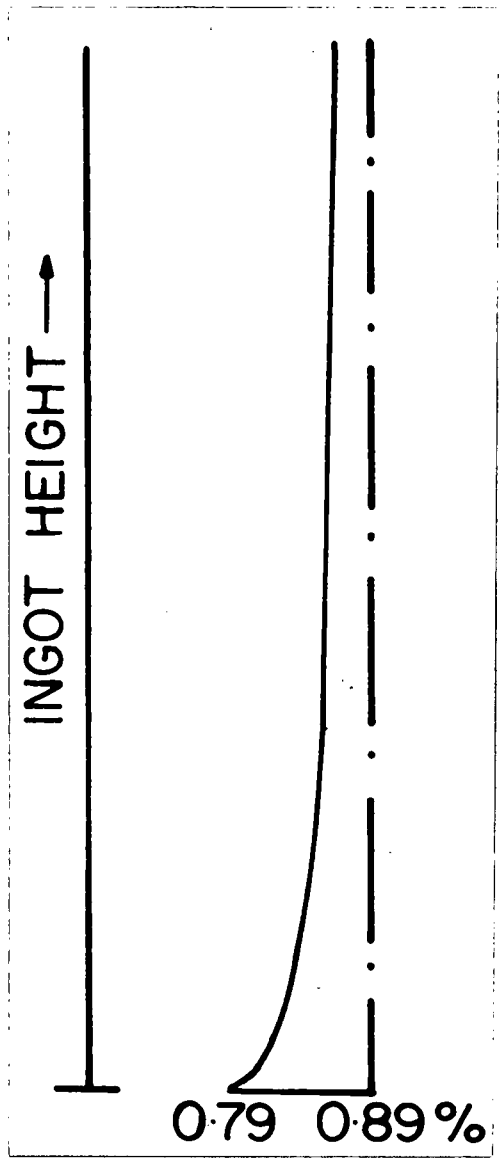

Figure 43 Carbon Distribution along the Axis of an ESR Ingot of High Carbon Chromium Steel. 0.89% - Mean C Content of Forged Electrode.

losses to the slag in a 40 ton ESR unit are decreased at high melt rates in accordance with our predictions with respect to higher temperatures and enhanced slag mass transfer coefficients. In addition, they have shown that the rate of alumina loss from the slag is substantially decreased at lower melting rates.

The above discussion deals with only a few examples of the usefulness in applying the present mass transfer model. The fact that we can see the relation between model parameters and known ESR phenomena shows very distinctly the benefits of mass transfer analysis. Important also has been the constant link with the heat transfer analysis. For example our analysis of the mass transfer phenomena would have been much more difficult and, likely impossible, without specific knowledge of interface temperatures and pool volumes.

5.3.5 Control of Alloy Losses

It is pertinent at this time, then, to attempt to establish some guidelines for control of alloy losses in ESR processing. A number of practical suggestions have already been made and a good many of these are in day to day use as mentioned in 1.2. These ideas include such practises as (a) melting under argon instead of air, (b) use of balanced slags and (c) surface preparation of the electrode material prior to use.

Melting under argon, however, would appear to decrease slightly the efficiency of the desulphurization reaction but this problem might be overcome by increased lime content of the slag.

Corrective additions of material into the slag to raise the activity and suppress the reaction could indeed backfire, as we have shown, by resulting in a increased tendency for reduction of inclusion forming elements into the ingot pool. A few different ideas arising out of this work are given below.

Firstly, we know that slag composition closely reflects the extent of the alloy losses. Sampling the slag is a much simpler operation than sampling the metal. Therefore, provided some rapid analysis technique were available it should be possible to monitor the alloy losses as they are occurring and perhaps make corrective additions. In any event, once one run was made a correction could be made to the electrode composition to produce an ingot of required specifications. This method would appear to be preferable to correcting the slag.

We have shown (4.1) that mass transfer is controlled by the slag transport steps. Since these mass transfer coefficients are functions of the slag velocity, it seems reasonable that any measures that we take to reduce the flow rate of slag would be beneficial from a mass transfer point of view. The most practical method of doing this would appear to be the use of as large an electrode as possible. This would have the beneficial effect of reducing the Lorentz-force induced velocity since this velocity is inversely proportional to the electrode radius. The use of external controls on the slag velocity has not yet been shown to produce a beneficial effect. A large electrode/mold ratio will have other secondary benefits as well. These effects include removing a large amount of slag/air contact surface and improving the geometry of the ingot pool.[56]

Finally, it appears from our results and from the published data that smaller furnaces seem to produce smaller changes in alloy content from electrode to ingot. However, accompanying this trend may be the increased number of inclusions in the final ingot due to reduction reactions. In large furnaces, therefore, it is suggested again that electrodes be made up with higher than specification levels of essential alloy elements to avoid substandard ingot quality. Since it seems that large furnaces are less prone to producing high levels of inclusions due to the cooler slag bath temperatures, there is a finite probability of producing superior ingots in large ESR installations. Also, if low sulphur levels are important, the use of large units would be helpful.

5.4 Electrochemical Phenomena

We have established, in our discussions in Chapter 4, that rectification of the AC waveform by current leakage through the mold wall is responsible for the production of Fe^{2+} in the slag. Unfortunately, the actual measurement of the rate of this electrochemical reaction could not be assessed due to difficulties in measuring the necessary currents. Nevertheless, the existence of the phenomenon would appear not to be confined to our small furnace for there are numerous reports[2,53,96,103,104] on levels of FeO in ESR slags similar to those observed in this work (.1 - 1%).

We have, however, found that insulating the mold very efficiently reduces this effect and thus we will limit ourselves to suggesting a method for preventing current leakage in the mold. It is impractical

and, undoubtedly, very expensive to use boron nitride paint in commercial practice. Conveniently, however, a great number of ESR furnaces use a withdrawal mold, much like a continuous casting operation. In such a configuration, it may be possible to insert some type of insulating gasket in the mold at some point below the slag surface and above the ingot metal pool. Since the slag is not subject to much vertical translation, this device could effectively prevent current leakage. At present we know nothing of the nature of this leakage and this would appear to be a profitable area of future research because of its important consequences.

5.5 Conclusions

The oxidative loss of manganese has been successfully interpreted by the proposed mass transfer model in a wide variety of ESR conditions. This success may be attributed to relative simplicity of the system chosen for this study, the availability of the appropriate thermochemical information and to the well defined mass transport processes affecting the loss of alloy elements.

The model has been used to provide specific, quantitative information on the nature of the mass transfer phenomena occurring in ESR processing. Previous assumptions of isothermal behaviour have been disproved while those concerning the negligible contribution of the falling droplets to alloy losses have been confirmed. In addition, much new information has been realized as a consequence of the model predictions.

We have ascertained that mass transfer is predominantly controlled by slag phase transport and that the alloy losses at the ingot pool/molten slag interface determine the ultimate extent of composition change. It has been possible to identify the critical parameters, such as slag flow velocity and ingot pool volume, which exert major influences on the overall mass transfer behaviour of the system. In turn, these parameters have been used as the basis for prediction of alloy losses in scaled-up ESR furnaces. Such calculations have shown that the alloy losses observed on small scale ESR are not, in fact, representative of that which is to be expected in the larger, commercial operations. Certain information relating to the nature of inclusions found in ESR ingots can also be derived from the model predictions, which indicate the close connection between slag composition and inclusion composition.

An additional major source of oxidant in AC electroslag processing has been identified. The electrochemical generation of ferrous ions has been found to be due to rectification of the AC waveform as a result of current leakage through the mold. A procedure to eliminate this harmful reaction in commercial practice was outlined. Finally, it was concluded that, with proper recognition and control of the factors affecting composition change, it should be possible to manufacture reproducibly good ingots in larger commercial electroslag furnaces.

5.6 Suggestions for Future Work

Possible avenues of future effort to extend this work may be divided approximately into three categories. Initially, as a prerequisite of extension of the model to the study of losses of the more

reactive elements (Si,Cr,Ti,Al), one must establish a complete body of thermochemical information relating to the activities of these components in the various CaF_2-based slags. The need for this data has been shown to be critical for successful implementation of the mass transfer model.

It would undoubtedly be beneficial to continue with tests on the small laboratory ESR unit to evaluate mass transfer behaviour of these more reactive elements. In particular, it is suggested that the apparent close relationship between inclusions and slag composition be studied extensively from a mass transfer point of view.

The electrochemical aspects of AC ESR may also best be investigated further on the laboratory unit. Such a program should include a investigation into the nature of electrical conduction through the slag skin and accurate measurement of the mold current component.

Finally, there appears to be an increasing necessity for experimentation on the larger commerical ESR furnaces. Although such investigations would undoubtedly be costly, there is great lack of knowledge of the specific detailed behaviour of these units. The parameters about which information should be obtained have been outlined in the text. In addition, there are great potential benefits to be realized in the heat transfer modelling of the large furnaces and such information has been shown to be indispensible not only to the successful scale-up of the heat transfer behaviour but also to the scale-up of the mass transfer model.

PRINCIPAL SYMBOLS

$[A]$	concentration of A in metal phase	mole cm^{-3}
$[A]_0$	initial concentration of A in metal phase	mole cm^{-3}
(A)	concentration of A in slag phase	mole cm^{-3}
$(A)_b, [A]_b$	bulk concentrations of A in slag, metal phases respectively	mole cm^{-3}
$(A)_i, [A]_i$	interfacial concentrations of A in slag, metal phases respectively	mole cm^{-3}
A_j	area of reaction interface j	cm^2
A_{max}	maximum area of oscillating drop	cm^2
a_i	activity of species i	
c_p	heat capacity	cal $gm^{-1}{}^\circ K^{-1}$
d	drop diameter	cm
d_{max}, d_{min}	maximum, minimum diameters of oscillating drop	cm
D_i	diffusivity of species i	$cm^2 sec^{-1}$
ΔG	free energy ($\Delta G^\circ = A + BT$)	cal mol^{-1}
g	acceleration due to gravity	cm sec^{-2}
h	heat transfer coefficient	cal $cm^{-2} sec^{-1} {}^\circ C^{-1}$
I	absolute current	ab amperes
K	equilibrium constant	
k_i	mass transfer coefficient of species i	cm sec^{-1}
k_L	lumped mass transfer coefficient	cm sec^{-1}
L	mass transfer boundary layer thickness	cm
MW_i	molecular weight	

$\dot{n}_i$	mass flux		mole $cm^{-3} sec^{-1}$
P	$\frac{\rho_s^2 \sigma^3}{g(\rho_m - \rho_s)\mu_s^4}$	Physical Properties Group	dimensionless
q	heat flux		cal sec^{-1}
Q	latent heat		cal gm^{-1}
R	radius		cm
Re	Reynolds number	Du ρ/μ	dimensionless
Sc	Schmidt number	$\mu/\rho D$	dimensionless
T	temperature		°C, °K
t	time		sec
t_e	contact time		sec
u	velocity		cm sec^{-1}
V_j	volume of phase j		cm^3
W_M	weight of metal		gm
W_S	weight of slag		gm
$\dot{W}_M$	melt rate		gm sec^{-1}
$\dot{W}'_M$	volumetric melt rate		cm^3 sec^{-1}
We	Weber number	$\frac{\rho u^2 L}{\sigma}$	dimensionless
X_i	mole fraction		

Greek Symbols

α_h	thermal diffusivity	cal $cm^{-2}sec^{-1}$
γ_i	activity coefficient of species i	
δ	electrode tip film thickness	cm
$\Delta(x)$	hydrodynamic boundary layer thickness	cm
ε, ε_0	amplitude correction factor for oscillating drop	dimensionless
θ	cone angle of electrode tip	degrees
κ	thermal conductivity	cal $cm^{-1}sec^{-1}{}^{\circ}K$
μ_m, μ_s	viscosity of metal, slag respectively	poise
ν	μ/ρ kinematic viscosity	cm^2 sec^{-1}
ξ	dimensionless mass transfer function	$\frac{\rho_s k_c A}{\dot{W}_M}$
ρ_m, ρ_s	density of metal, slag respectively	gm cm^{-3}
σ	surface tension	dyn cm^{-1}
ω	oscillation frequency	sec^{-1}
Ω	molar equilibrium constant	mol cm^{-3}

BIBLIOGRAPHY

1. DECKER, R.F. Seminar on Maraging Steels held by Int. Nat. Nickel Co. Pittsburgh, 1962.

2. MEDOVAR, B.I. et al. "Electroslag Remelting."B. Ye. Paton ed. Moscow, 1963.

3. HLINERY, J. and BUSEK, Z. Sbornik Ved. Praci, V.S.B.O. (Ostrava)(1965), II, 3, 483.

4. YUASSA, G. Proc. Second Int. Symp. on ESR Tech. V.2. Mellon Inst., 1969.

5. ETIENNE, M. Ph.D. Thesis, University of B.C., 1970.

6. HOLZGRUBER, W., MACHNER, P. and PLOECKINGER, E. Trans. Vac. Met. Conf., Amer. Vac. Soc. N.Y. V1, 1969.

7. HOYLE, G., DEWSNAP, P., SALT, D.J. and BARRS, E.M. "Electro-Slag Refining Technology," BISRA, Open Report, # MG/A/416/66.

8. LATASH, Yu.V. et al. "Electroslag Remelting," IZV-VO Metallurgiya, Moscow, 1970.

9. PATCHETT, B.M. and MILNER, D.R. Welding Research Supplement, October 1972, pp. 491-s - 505-s.

10. KLJUEV, M.M. et al. Neue Hütte (1971), 16, 9/10, 603-606.

11. ETIENNE, M. and MITCHELL, A. Elec. Furn. Conf. Proc., AIME, (1970) 28, p. 28.

12. PANIN, V.V., FROMIN, N.I. and GALKIN, V.K. Liteinol Proizvod (1971), 6, p. 29.

13. STEINMETZ , E. Arch. Eisenhüttenwes. (1968) 6, 421.

14. COOPER, C.K., GHOSH, D., KAY, D.A.R. and POMFRET, R.J. Elec. Furn. Conf. Proc., AIME, (1970), 28, p. 8.

15. WOLFENBÜTTEL, H.M. and HANAU, M.W. Arch Eisenhüttenwes. (1972), 44, 2, 81-85.

16. ZHMOIDEN, G.I., Izv. Akad. Nauk. SSSR. Metal. (1972), 4, 60-66.

17. HAWKINS, R.J., MEHERALI, S.G. and DAVIES, M.W. JISI, (1971), 209, 8, 646-657.

18. CRIMES, P.B. Ph.D. Thesis, Imperial College, Univ. of London, 1968.

19. DUCKWORTH, W.E. and HOYLE, G. "Electro-Slag Refining." Chapman and Hall, 1969.

20. WHITTAKER, D.A. Ph.D. Thesis. McMaster University, 1968.

21. KNIGHTS, C.F. and PERKINS, R. ISI/SMEA Conf. on ESR. January, 1973, VI, paper 3.

22. HAWKINS, R.J., SWINDEN, D.J. and POCKLINGTON, D.N. Ibid., V.2, Paper 1.

23. MITCHELL, A., SZEKELY, J. and ELLIOTT, J.F. Ibid., V1, Paper 1.

24. MENDRYKOWSKI, J., POVEROMO, J.J., SZEKELY, J. and MITCHELL, A. Met. Trans (1972), 3, 7, 1761.

25. BEYNON, G. Ph.D. Thesis, University of B.C., 1971.

26. MORI, K., HATAMAKA, T. and OHNO, Y. Trans ISIJ (1968), 8, 401-408.

27. HAWKINS, R.J. and DAVIES, M.W. JISI (1971), 209, 3, 226-230.

28. DAVIES, M.W., HAWKINS, R.J. and SMITH, P.N. Steel Times (1969), 197, 4, 237-240.

29. Ibid., Steel Times (1969), 197, 5, 353-356.

30. DAVIES, M.W. "Chemistry of CaF_2-Based Slags," in Chemical Metallurgy of Iron and Steel, ed. Buckle, E.R. and Hawkins, R.I. ISI, 1973, pp. 43-51.

31. NIWA, K. and YOKOKAWA, T. Ibid., pp. 77-81.

32. BODSWORTH, C. "Physical Chemistry of Iron and Steel Manufacture." Longmans, 1963.

33. CHIPMAN, J., GERO, J.B. and WINKLER, T.B. TRANS AIME (1952), 194, 1173.

34. Basic Open Hearth Steelmaking, ed. G. Derge., 3rd Ed. AIME, 1964.

35. JACKSON, R.O. M.A.Sc. Thesis, University of B.C., 1971.

36. KAY, D.A.R., MITCHELL, A. and RAM, M. JISI (1970), 208, 2, pp. 141-146.

37. SMITH, P.N., and DAVIES, M.N. 1 MM Trans. (1971), 80, C87-C92.

38. JOSHI, S. Ph.D. Thesis, University of B.C., 1971.

39. BIRD, R.B., STEWART, W.E. and LIGHTFOOT, E.N. "Transport Phenomena." Wiley, 1960.

40. MITCHELL, A. Unpublished Research.

41. KLJUEV, M.N. and MIRONEV, Yu.M. Stalin English, (1967) 1, 480.

42. WHITMAN, W.G. Chem. and Met. Eng. (1923), 29, 147.

43. HIGBIE, R. A.I.CH.E. (1935), 31, 365.

44. DANCKWERTS, P.V., Trans. Faraday Soc. (1950), 46, 300.

45. Ibid., Ind. Eng. Chem. (1951), 43, 1460.

46. Ibid., A.I.Ch.E.J. (1955), 1, 456.

47. TOOR, H.L. and MARCHELLO, J.M. A.I.Ch.E.J. (1958), 4, 1, 97.

48. DARKEN, L.S. and GURRY, R.W. "Physical Chemistry of Metals" McGraw Hill, 1953.

49. PAVOLOTSKÜ, D.Yu. et al. Steel in the USSR (1972) 2, 4, 289-291.

50. KAMENSKY, Yu. M. et al. "Thermal Stability of the Slag Bath. . ." in "Conf. on Special Electrometallurgy" ed. B.E. Paton, Kiev, 1972, V1, 33-46.

51. MAECKER, H. Z. Physik (1955), 141, 198.

52. BIRD, R.B., STEWART, W.G. and LIGHTFOOT, E.N. op. cit., Wiley, 1960, pp. 605-608.

53. MITCHELL, A. "Electrochemical Processes in ESR" in "Conf. on Special Electrometallurgy," ed. B.E. Paton, Kiev, 1972, V2, 95-109.

54. KAY, D.A.R. "Reaction Sites in AC ESR", Ibid., 63-82.

55. BALLANTYNE, A.S. and FRASER, M.E. Unpublished Research.

56. MITCHELL, A., JACKSON, R.O. and BALLANTYNE, A.S. Proc. 4th Int. Symp. on ESR Processes, Tokyo, 1973, pp. 1-12.

57. HEERTJES, P.M. and de NIE, L.H. "Mass Transfer to Drops" in "Recent Advances in Liquid-Liquid Extraction" C. Hanson ed. Pergammon, 1971, pp. 367-406.

58. von BERG, R.L. "Simultaneous Heat and Mass Transfer," Ibid., pp. 407-427.

59. von BERG, R.L. and HENKEL, W.M. "Simultaneous Heat and Mass Transfer in Single Drop Liquid-Liquid Extraction." International Solvent Extraction Conf., The Hague, 1971, pp. 852-871.

60. SIDEMAN, S. and SHABTAI, H. Can. J. Chem. Eng. (1964), 42, 107.

61. OLANDER, D.R. Nucl. Sci. and Eng. (1968), 31, 1, 1-18.

62. KATZ, H.M., HILL, F.B. and SPEIRS, J.L. TRANS. AIME (1960), 218, 10, 770-775.

63. CHON, M., YOSHIZAWA, A. and TATE, M. Proc. I.C.S.T.I.S. Suppl. Trans. ISIJ, 1971, Vol. II, pp. 500-505.

64. ISHÜ, K., KISHIMOTA, S. and YOSHÜ, C. Ibid., pp. 506-571.

65. CAMPBELL, J. and DAWSON, D.I. "Magneto-hydrodynamics in Casting Processes," BISRA OPEN Report, MG/58/71.

66. CAMPBELL, J. J. Metals. (1970), 22, 7, 23-35.

67. FRASER, M.E. et al. Met. Trans (1971), 2, 3, 817-823.

68. DISTIN, P.A., HALLETT, G.D. and RICHARDSON, F.D. JISI (1968), 206, 8, 821-833.

69. BAKER, L.A., WARNER, N.A. and JENKINS, A.G. TRANS. AIME (1964), 230, 10, 1228.

70. WHITEWAY, S.G. Can. Met. Quart. (1971), 10, 3, 185.

71. HAMIELEC, A.E., LU, W-K, and McLEAN, A. Can. Met. Quart. (1968), 7, 1, 27.

72. HANDLOS, A.G. and BARON, E.T. A.I.Ch.E.J. (1957) 3, 1, 127-136.

73. ANGELO, J.B., LIGHTFOOT, E.N. and HOWARD, D.W. A.I.Ch.E.J. (1966), 12, 4, 751-760.

74. WARREN, T.J. Ph.D. Thesis, Purdue University, 1971.

75. BAKER, L.A. and WARD, R.G. JISI (1967), 205, 7, 714.

76. KNIGHTON, J.B., JOHNSON, I. and STEUNENBERG, R.K. "Uranium and Plutonium Purification by the Salt Transport Method." in Symp. on Reprocessing of Nuclear Fuels" Nuclear Metallurgy, 1969, V 15, P. Chiotti, ed. USAEC Report Conf.- 690801, pp. 337-362.

77. OLANDER, D.R. and PASTERNAK, A.D. Ibid., pp. 467-510.

78. GARNER, F.H. and TAYEBAN, M. AM. R. Soc. esp. Fis. Quim. (1960), 56B, 479.

79. HU, S. and KINTNER, R.C. A.I.Ch.E.J. (1955), 1, 1, 42-48.

80. LAPIDUS, L. "Digital Computation for Chemical Engineers." McGraw-Hill, 1962.

81. LAMB, H. "Hydrodynamics". 6th ed.Dover, New York, 1945.

82. ELLIOTT, J.F., GLEISER, M. and RAMAKRISHNA, V. "Thermochemistry for Steelmaking." Addison-Wesley, 1963.

83. ISAKSSON, I. and Öberg, K.E. Scand. J. Met. (1973), 2, 1, 1-4.

84. KOR, G.J.W. and RICHARDSON, F.D. TRANS. AIME (1969), 245, 2, 319-327.

85. CAMERON, J. et al., MEt. Trans. (1970), 1, 7, 1839-1844.

86. MITCHELL, A. and JOSHI, S. Met. Trans. (1973), 4, 3, 631.

87. SUN, R.C. and PRIDGEON, J.W. Second. Int. Symp. on ESR Tech. (1969), Pittsburgh, E.K. Shat ed. Part II.

88. WARNER, N.A. Advances in Extractive Metallurgy, 1 MM, 1968, p. 317.

89. WARD, R.G. and SALMON, K.A. JISI, (1960), 198, 12, 393.

90. BLOOM, H. "The Chemistry of Molten Salts." Benjamin, 1967.

91. PEOVER, M.G. J. Inst. Metals (1972), 100, 97.

92. BAIRD, D.C. "Experimentation." Prentice-Hall, 1962.

93. BRIMACOMBE, J.K. "Interfacial Turbulence in Liquid Metal Systems" in "Richardson Conference on "The Physical Chemistry of Process Metallurgy." Proc. to be published.

94. MITCHELL, A. "Oxide Inclusion Behaviour during Consumable Electrode Remelting" to be published.

95. CHALMERS, B. "Principles of Solidification," Wiley, 1964.

96. MITCHELL, A. and BELL, M. Can. Met. Quart. (1972), 11, 2, 363.

97. OLSEN, V. in "Physico-Chemical Aspects of Process Metallurgy" ed. A.M. Samarin, Nanka, Moscow, 1973, pp. 135-141.

98. BOUCHER, A. "Application of ESR." in "Bulletin de Centre des Etudes de Metallurgie" (1972), 12, 229-263.

99. COOPER, C.K. and KAY, D.A.R. JISI (1970), 208, 9, 856.

100. ELTXOV, K.S. et al. "Peculiarities of Large Plate Ingot . . . ESR" in "Conf. on Special Electrometallurgy," ed. B.E. Paton, Kiev, 1972, V1, 23-32.

101. VOLKOV, S.E. "On Mechanism of Removal of Inclusions . . ." Ibid., 12-32.

102. PATON, B.E. et al. "Investigation of Temp. Fields of Large ESR Ingots . . ." Ibid., 144-157.

103. VASILJEV, Ya. M. et al., Ibid., 3-12.

104. MYZETSKY, V.L. et al. "Quality of 22K ESR Steel," Ibid., 119-126.

105. FORTUNE, W.B. and MELLON, M.G. Ind. Eng. Chem. Anal. (1938), 10, 60.

106. CHARLOT, G. "Nouveau Tracte de Chimie Analytique," Masson et al., Paris, 1961, p. 786.

107. DEVUYST, E. Private Communication.

APPENDIX I

DETERMINATION OF AUXILARY PARAMETERS FOR MASS TRANSFER MODEL

A.I.1 Calculation of Average Melt Rate

From the motor speeds given in Tables II-VII, we obtain an electrode travel rate from the appropriate calibration curve. For example, taking the average motor speed from Run #27, Table II, the corresponding electrode travel rate 3.1 (10^{-2}) cm sec^{-1}.

The volumetric melt rate for the 3.81 cm ϕ electrode commonly used here is then

$$\frac{\pi d^2}{4} \times ETR = \frac{\pi(3.81)^2}{4} \times 3.1(10^{-2}) \qquad (A.1.1)$$

$$\dot{W}'_M = 0.36 \text{ cm}^3 \text{ sec}^{-1}$$

Multiplying by ρ_{Fe}, we obtain the melt rate in mass sec^{-1}

$$\text{or } \dot{W}_M = 2.6 \text{ gm sec}^{-1}$$

A.I.2 Drop Weight Calculation

The regularly occurring amperage peaks found on the recorded amperage trace have been shown to correspond to the detachment of drops from the electrode tip.[35] It was a relatively simple matter to

count these peaks for a given number of seconds to obtain the number of drops per sec. (Figure A.I.1)Dividing the melt rate, $\dot{W}_M$, by this quantity yields the average drop weight. Experience has shown that this weight averages about 2.5 gm for lime slags in melts on AC power.[5] The melt rate is, then, a direct indication of the number of drops/unit time passing through the slag. On a large ESR unit, where multiple drop sites are found, the average drop size may be calculated from the estimated number of sites and the average melt rate although the frequency of drop formation is unknown.

A.I.3 Rate of Slag Loss

The amount of slag lost to the slag skin was important in determining overall mass balances. Although the slag skin was often not uniform in thickness over the length or circumference of an ingot, we have quoted an average of these values in the Tables II-VII. Since the slag bath necessarily rose at the same rate as the ingot grew, the slag skin frozen was proportional to the melt rate.

$$\text{Volume of slag skin of height } h = \pi(R^2_{mold} - R^2_{ingot})\, h \quad \text{(A.1.2)}$$

Rate of rise of the ingot, RI, may be estimated by

$$RI = \text{Volumetric Melt Rate/Cross Sectional Area of Ingot}$$

$$= \dot{W}'_M / \pi r^2 \quad \text{cm sec}^{-1}$$

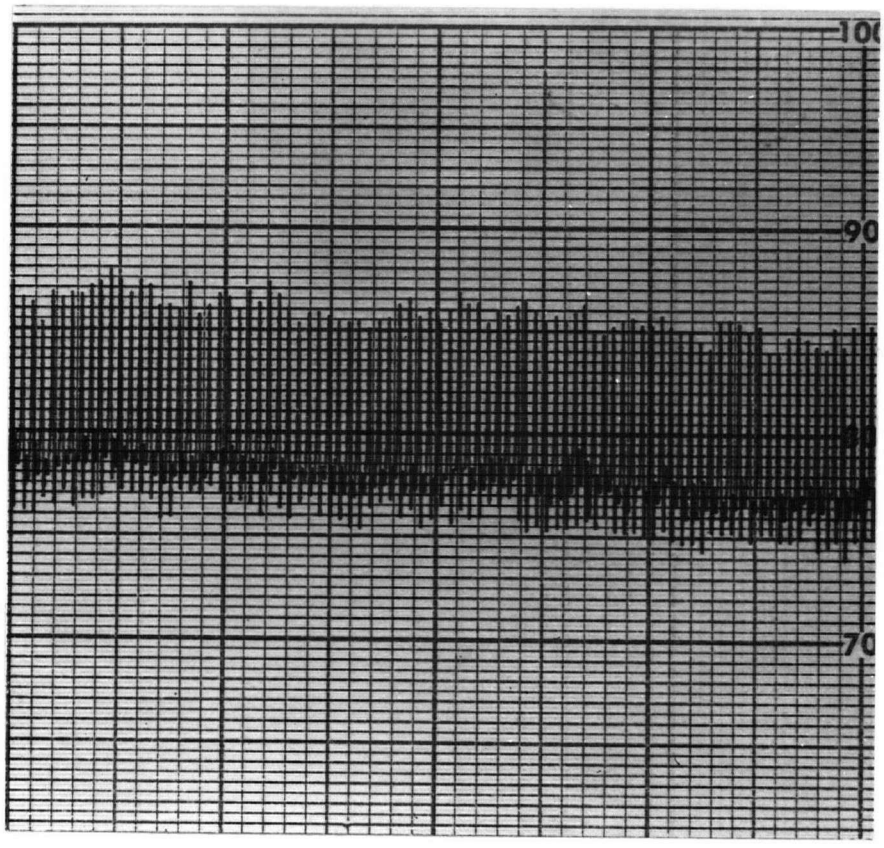

Figure A1.1 Oscillographic Current Trace Obtained While Melting 1½" ϕ C1018 in CaF_2-20% CaO using 3" ϕ Mold. Chart Speed 5" min^{-1}

Substituting RI for h in A.I.2 and since the rate of ingot rise is equivalent to the rate of rise of slag skin, we have the rate of slag loss, VL, where $\dot{W}'_M = \dot{W}_M / \rho_{Fe}$ (melt rate (gm sec^{-1})/density = MR)

$$VL = \pi(R^2_{mold} - R^2_{ingot}) \times RI \times \rho_{slag}$$

$$= \frac{(R^2_M - R^2_I) \times MR}{R^2_I \ \rho_{Fe}} \rho_{slag}$$

$$\text{Rate of slag loss} = .36 \ MR \ \{(\frac{R_M}{R_I})^2 - 1\} \qquad (A.1.3)$$

For a slag skin thickness of 1 mm and melt rate of 2.6 gm sec^{-1}

$$\text{Rate of slag loss} = .36 \times 2.6 \times ((\frac{3.81}{3.71})^2 - 1)$$

$$= .05 \text{ gm } sec^{-1}.$$

APPENDIX II

ANALYTICAL METHODS

A.II.1 Determination of Total Iron

Iron in the dissolved slag sample was estimated by a colourimetric method using the orange-red complex of orthophenanthroline. Ferric iron has no effect on this reaction and hydroxylamine hydrochloride was added to ensure that all the iron in the solution was reduced to the ferrous state. Buffering of the solution at pH 4.5 was obtained with a sodium acetate-acetic acid buffer solution.

A composite reagent was prepared by mixing the following solutions.

Buffer Solution: 816 gm anhydrous sodium acetate dissolved in ≃ 1 12 l. of water with heat. Add 810 ml glacial acetic acid. Cool and make up to 3 l. with water.

Reducing Solution: ($Fe^{3+} \rightarrow Fe^{2+}$) 10 gm hydroxylamine hydrochloride dissolved in 1 l. of water.

Colour Producing Solution: 1 1/2 gm orthophenanthroline dissolve in ≃ 200 ml water with enough HCl to just dissolve. Made up to 1 l. with water.

The analysis was carried out using 5 ml aliquots of the slag sample solution with 90 ml of the reagent solution made up to 100 mls with water. The optical density of each solution was measured on a

Beckman Model B spectrophotometer, using light of wavelength 510 mμ. The concentration of iron was read directly from a calibration curve prepared by using standard iron solutions.

Fluorine is known to interfere in the orthophenanthroline method but only when the amount of fluorine is 50 times greater than the ferrous iron. Although this situation may exist in the solid slag sample, by the time the sample is dissolved, a large amount of fluorine has been driven off as HF. This is evidenced from the etching of the glass during even a single analysis. Also Fe^{2+} standards run with comparable levels of CaF_2 to the slag samples showed no effect on the accuracy. Therefore we have assumed no interference from F in the analysis of iron.

A.II.2 Determination of Manganese

Mn^{2+} was oxidized to MnO_4^- by potassium periodate.[106] Phosphoric acid addition prevented precipitation of MnO_2 or manganese periodate and decolourized the ferric solution while stabilizing MnO_4^-. It was also necessary in this case to heat the 10 ml aliquot of the slag sample solution with a small amount (≃ 5-10 mls) of nitric acid to ensure complete oxidation of ferrous iron.

A composite reagent was prepared by mixing 100 mls of concentrated sulphuric acid, 100 mls of concentrated phosphoric acid and 800 mls of 5% potassium periodate solution.

The 10 ml aliquot of sample solution was evaporated with HNO_3 to ≃ 5 ml. To this 90 mls of reagent solution were added and

heated to 90°C for five minutes to oxidize Mn^{2+} to MnO_4^-. After complete oxidation, the cooled solution was made up to 100 ml with water. The concentration of manganese was determined from the spectrophotometer absorbance for light of 524 mμ and a calibration curve obtained from prepared manganese standard solutions.

Some ions do interfere in this analysis, especially Mo(VI), V(V), Ti(IV) and Cr(VI). Since the slag samples were taken with Mo wires, there was a possible source of Mo interference. The following simple test was performed to show that no significant amount of Mo dissolved in the slag sample. Two slag samplers of Mo wire were weighed and one dipped in a CaF_2 - CaO - FeO slag. Both were then placed in hot and 50% HCl solution until the slag had dissolved. Upon reweighing the Mo wires, it was found that the weight loss of each was identical at .1 mg. The total weight loss would thus appear to be due to the dissolution of Mo in the acid solution and not in the slag. Mo interference was, then, not a factor in Mn analysis.

A.II.3 Determination of Fe^{2+}. [107]

A portion of the slag sample was dissolved in 20% H_2SO_4 under Helium to protect any ferrous from oxidation. The dissolved sample was then titrated with .004299 N $Ce(SO_4)_2$ with a known amount of orthophenanthroline ferrous sulphate complex. The end point was a very pale green colour, the original solution being light amber. The concentration of Fe^{2+} was calculated from the reaction.

$$Ce^{4+} + Fe^{2+} \rightarrow Ce^{3+} + Fe^{3+}$$

and the number of equivalents of Ce^{4+} used in the titration. A correction was then made for the Fe^{2+} in the ferrous sulphate complex.

APPENDIX III

DERIVATIONS OF ADDITIONAL MASS TRANSFER EXPRESSIONS

A.III.1 Desulphurization of Fe-S Alloy During ESR Using CaF_2 - CaO Slags

Desulphurization is undoubtedly the most beneficial chemical reaction occurring in ESR processing of many commercially refined alloys and, as such, it has been a common area of interest amongst previous workers in the field[2,14,15,17,28,29]. The exchange reaction is normally written as

$$(O^{2-}) + \underline{S} \rightarrow (S^{2-}) + \underline{O} \qquad \text{(A.3.1)}$$

In order to include the effect of FeO on this reaction, we combine the reaction

$$Fe + \underline{O} \rightarrow (FeO) \qquad \text{(A.3.2)}$$

where (FeO) may be written as $(Fe^{2+}) + (O^{2-})$ for a completely ionic slag.[30]

The relation that will be used in the formulation of the mass transfer model for desulphurization is

$$\underline{S} + Fe(\ell) \rightarrow (S^{2-}) + (Fe^{2+}) \qquad \text{(A.3.3)}$$

obtained by combining (A.3.1) and (A.3.2)

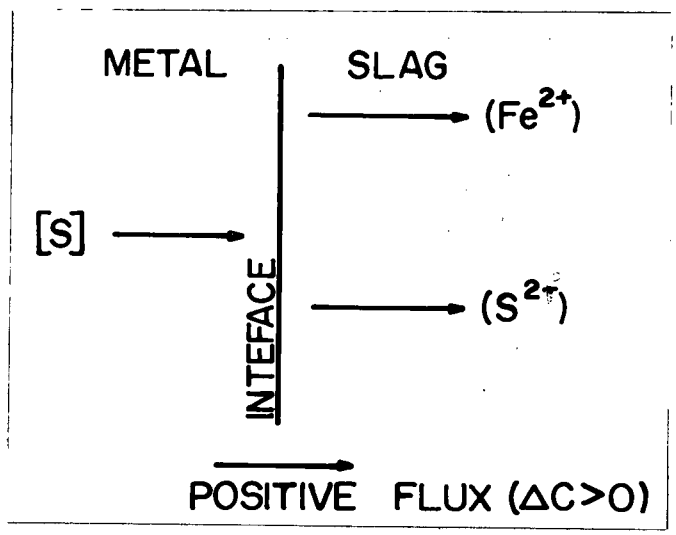

Figure A.3.1 Schematic Representation of Mass Fluxes in Desulphurization Reaction $\underline{S} + Fe(\ell) \underset{\leftarrow}{\overset{\rightarrow}{}} (Fe^{2+}) + (S^{2-})$

The procedure followed is identical to that of Chapter 2 for the mass transfer processes occurring during the oxidation of Mn by FeO, using the assumptions of steady state and instantaneous interfacial reaction; i.e. interfacial equilibrium.

The flux equations are

$$\frac{\dot{n}_S}{A} = k_S \{[S]_b - [S]_i\} \qquad (A.3.4)$$

$$\frac{\dot{n}_{S^{2-}}}{A} = k_{S^{2-}} \{(S^{2-})_i - (S^{2-})_b\} \qquad (A.3.5)$$

$$\frac{\dot{n}_{Fe^{2+}}}{A} = k_{Fe^{2+}} \{(Fe^{2+})_i - (Fe^{2+})_b\} \qquad (A.3.6)$$

at steady state, we have, by conservation of mass.

$$\dot{n}_S = \dot{n}_{S^{2-}} = \dot{n}_{Fe^{2+}} \qquad (A.3.7)$$

The existence of instantaneous interfacial reaction normally assumed in pyrometallurgical mass transfer studies does not always apply to sulphur transfer situations.[89] With increasing silica content of a slag, the overall transfer rate appears to become chemically controlled. Although Ward[89] was unable to pinpoint an exact mechanism for sulphur transfer in general from his experimental evidence, he did show that slags with CaF_2 additions exhibited no traces of chemical control behaviour with respect to sulphur transfer. Since the slags dealt with here are 80% CaF_2, the original assumption of fast interfacial reactions leading to interfacial equilibrium is still valid. Hence,

$$\Omega_S = \frac{(Fe^{2+})_i \ (S^{2-})_i}{[S]_i} = \text{molar equil. Const.} \qquad (A.3.8.)$$

This series of equations can now be used to develop an expression for $k_{S^{2-}}$ in terms of quantities that have been measured in Run #62. Therefore, taking (A.3.5) and substituting (A.3.8) for $(S^{2-})_i$ we obtain

$$\frac{\dot{n}_{S^{2-}}}{A} = k_{S^{2-}} \left\{ \frac{\Omega_S [S]_i}{(Fe^{2+})_i} - (S^{2-})_b \right\} \qquad (A.3.9)$$

but from (A.3.6), we have

$$(Fe^{2+})_i = \frac{\dot{n}_{Fe^{2+}}}{A} \frac{1}{k_{Fe^{2+}}} + (Fe^{2+})_b \qquad (A.3.10)$$

From the steady state assumption, we know that

$$\dot{n}_{Fe^{2+}} = \dot{n}_{S^{2-}} = V_S d(S^{2-})/dt \qquad (A.3.11)$$

Substituting (A.3.11) and (A.3.10) into (A.3.9) and solving for $k_{S^{2-}}$, we obtain

$$k_{S^{2-}} = \frac{\frac{V_S}{A} d(S^{2-})/dt}{\frac{\Omega_S [S]_i}{\frac{V_S}{A} \frac{d(S^{2-})}{dt} \frac{1}{k_{Fe^{2+}}} + (Fe^{2+})_b} - (S^{2-})_b} \qquad (A.3.12)$$

This is the relation used in IV.2.2 for calculation of $k_{S^{2-}}$. The expression for the evaluation of Ω_S is derived as follows. The equilibrium constant for reaction (A.3.3) is

$$K_{FeS} = \frac{(a_{CaS})(a_{FeO})}{[Wt\%S]} \qquad (A.3.13)$$

where

$$\ell n\ K_{FeS} = \frac{2330}{T} - 4.07^{32} \qquad (A.3.14)$$

for the reaction written with $\underline{S}$ in the 1 wt% standard state but

$$a_{CaS} = \gamma_{CaS}\ X_{CaS}$$

$$= \gamma_{CaS}\ \frac{(wt\ \%\ S^{2-})}{MW_{S^{2-}}\ (\frac{80}{78.08} + \frac{20}{56.08})} \quad (\text{for } CaF_2\text{-}20\%CaO\ \text{Slag})$$

$$\text{since wt \% } S^{2-} + (S^{2-}) \times \frac{100 \times MW_{S^{2-}}}{\rho_{Slag}}$$

$$\therefore\ a_{CaS} = \gamma_{CaS}\ \frac{(S^{2-}) \times 100}{(1.38)\ \rho_{Slag}}$$

$$\text{Similarly } \alpha_{FeO} = \gamma_{FeO}\ \frac{(Fe^{2+}) \times 100}{(1.38)\ \rho_{Slag}}$$

$$wt\ \%\ S = [S] \times \frac{100 \times 32}{\rho_{metal}}$$

Substituting these expressions into (A.3.13) and solving for Ω_S (A.3.8), we get

$$\Omega_S = \frac{(Fe^{2+})_i (S^{2-})_i}{[S]_i} = \frac{K_{FeS} \times 64 \times (1.38)^2 \times \rho_S}{100\ \gamma_{CaS}\ \gamma_{FeO}\ \rho_M}$$

Replacing K by the appropriate form of A.3.14,

$$\Omega_S = \frac{1.22 \exp(2330/T - 4.07)\ \rho_S}{\gamma_{CaS}\ \gamma_{FeO}\ \rho_M} \qquad (A.3.15)$$

A.III.2 Desulphurization of Resulphurized Steel in CaF_2-CaO Slags

Resulphurized steels are generally known for their free machining qualities. The cause of this machinability is the presence of a relatively large number of MnS inclusions due to typical sulphur levels of 0.1 - 0.25 wt % and manganese levels of 0.8 - 1.4%. At steelmaking temperatures, MnS dissolves in the molten iron and we must consider the species Mn and S in our analysis. It is readily shown[32] that the equilibrium constant, K, for the reaction

$$\underline{Mn} + \underline{S} \rightleftarrows (Mn^{2+}) + (S^{2-}) \qquad (A.3.16)$$

is given by

$$K_{MnS} = \exp\left\{\frac{17160}{T} - 10.86\right\} \qquad (A.3.17)$$

for the reaction written in terms of 1 wt % standard state for [S] and [Mn] in the metal.

$$\text{Also } K_{MnS} = \frac{(a_{CaS})(a_{MnO})}{[\%\ S]\ [\%\ Mn]} \qquad (A.3.18)$$

Using the factors given in A.III.1 for conversion of K_{FeS} to the molar form, Ω_S, (A.3.18) becomes

$$K_{MnS} = \frac{\gamma_{CaS}\ \gamma_{MnO}}{32 \times 54.9} \left(\frac{7.2}{2.6 \times 1.381} \right)^2 \frac{(S^{2-})(Mn^{2+})}{[S][Mn]} \qquad (A.3.19)$$

$$\text{if} \quad \Omega_M = \frac{(S^{2-})_i (Mn^{2+})_i}{[S]_i\ [Mn]_i} \qquad (A.3.20)$$

= molar equil const for Reaction (A.3.16)

then solving A.3.19 for Ω_M and substituting (A.3.17)

$$\Omega_{MnS} = \frac{438 \times \exp(17160/T - 10.86)}{\gamma_{CaS}\ \ \gamma_{MnO}} \qquad (A.3.21)$$

In order to demonstrate that this reaction of manganese and sulphur is really the reaction we must consider we perform the following operations. Combining the expressions (A.3.20) and (A.3.21) we can solve for a desulphurization constant $(S^{2-})(Mn^{2+})$ with the result

$$(S^{2-})(Mn^{2+}) = \frac{[S][Mn]\ 438\ \exp(17160/T-10.86)}{\gamma_{CaS}\ \ \gamma_{MnO}}$$

Similarly for (A.3.8) and (A.3.15), we obtain

$$(S^{2-})(Fe^{2+}) = \frac{[S]\ 1.22 \times 2.6 \times \exp(2330/T-4.07)}{\gamma_{CaS}\ \ \gamma_{FeO}} \qquad (A.2.23)$$

Taking the following values of the parameters

$$[S] = .13\%;\ [Mn] = 1.3\%;\ \gamma_{CaS} = 3;\ \gamma_{FeO} = 3.0;\ \gamma_{MnO} = 7$$

we find that for 1525°C and 1675°C, the desulphurization constant (A.3.22) has values of $2.78(10^{-6})$ and $1.33(10^{-6})$ respectively compared with $7.43(10^{-7})$ and $6.72(10^{-7})$ respectively for (A.3.23). Therefore we are, indeed, looking at the Mn + S desulphurization reaction for a typical resulphurized steel melted through a CaF_2 - 20%CaO slag. The development of the mathematical model is done exactly as in the two previous cases, but with the additional complication of an extra flux term.

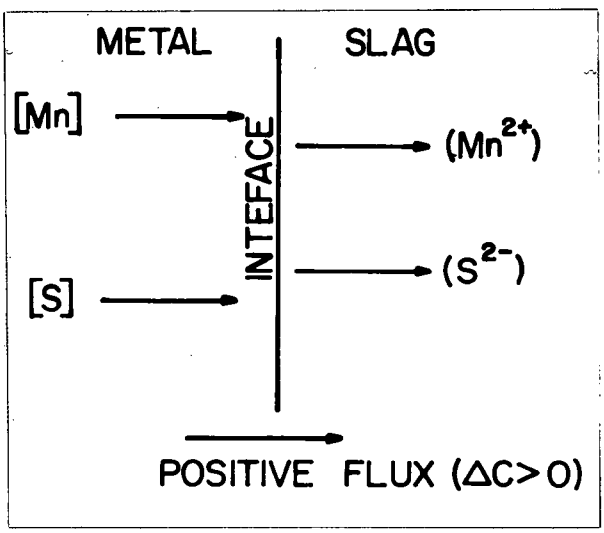

Figure A.3.2 Schematic Representation of Mass Fluxes in Manganese Desulphurization Reaction (A.3.16)

The phenomenological flux equations are

$$\frac{\dot{n}_S}{A} = k_S \{ [S]_b - [S]_i \} \quad \text{(A.3.24)}$$

$$\frac{\dot{n}_{Mn}}{A} = k_{Mn} \{ [Mn]_b - [Mn]_i \} \quad \text{(A.3.25)}$$

$$\frac{\dot{n}_{S^{2-}}}{A} = k_{S^{2-}} \{ (S^{2-})_i - (S^{2-})_b \} \quad \text{(A.3.26)}$$

$$\frac{\dot{n}_{Mn^{2+}}}{A} = k_{Mn^{2+}} \{ (Mn^{2+})_i - (Mn^{2+})_b \} \quad \text{(A.3.27)}$$

at steady state, we have:

$$\dot{n}_S = \dot{n}_{Mn} = \dot{n}_{Mn^{2+}} = \dot{n}_{S^{2-}} = \dot{n} \quad \text{(A.3.28)}$$

by conservation of mass, we also have

$$-V_m \, d[S] = -V_m d[Mn] = V_S d(S^{2-}) = V_S d(Fe^{2+}) \quad \text{(A.3.28(a))}$$

Also, we have the condition of interfacial equilibrium

$$\Omega_M = \frac{(Mn^{2+})_i (S^{2-})_i}{[Mn]_i \, [S]_i} \quad \text{(A.3.20)}$$

Eliminating the interfacial concentration $[Mn]_i$ from equation (A.3.25)

$$\frac{\dot{n}_{Mn}}{A} = k_{Mn} \{ [Mn]_b - [Mn]_i \}$$

$$= k_{Mn} \{ [Mn]_b - \frac{(Mn^{2+})_i (S^{2-})_i}{\Omega_M [S]_i} \}$$

Rearranging this expression

$$\frac{\dot{n}_{Mn}}{A} \frac{\Omega_M [S]_i}{k_{Mn} (Mn^{2+})_i} = \frac{[Mn]_b \Omega_M [S]_i}{(Mn^{2+})_i} - (S^{2-})_i \qquad (A.3.29)$$

From A.3.24, we have

$$\frac{\dot{n}_{S^{2-}}}{A} \frac{1}{k_{S^{2-}}} = (S^{2-})_i - (S^{2-})_b$$

Upon adding this relation to A.3.29 and solving for $\frac{\dot{n}}{A}$

$$\frac{\dot{n}}{A} = \frac{\Omega_M [Mn]_b [S]_i - (S^{2-})_b (Mn^{2+})_i}{\frac{(Mn^{2+})_i}{k_{S^{2-}}} + \frac{\Omega_M [S]_i}{k_{Mn}}}$$

Also

$$\frac{\dot{n}}{A} = \frac{\dot{n}_S}{A} = k_S \{[S]_b - [S]_i\} \quad \text{from A.3.24}$$

Equating the above expressions for $\frac{\dot{n}}{A}$

$$\frac{k_S[S]_b(Mn^{2+})_i}{k_S^{2-}} - \frac{k_S\Omega_M[S]_i^2}{k_{Mn}} + \frac{\Omega_M[S]_b[S]_i k_S}{k_{Mn}}$$

$$- \frac{k_S[S]_i(Mn^{2+})_i}{k_S^{2-}} = \Omega_M[Mn]_b[S]_i - (S^{2-})_b(Mn^{2+})_i$$

Collecting terms and multiplying by $k_{Mn}/k_S\Omega_M$

$$[S]_i^2 + [S]_i \left\{ \frac{k_{Mn}}{k_S}[Mn]_b + \frac{k_{Mn}}{\Omega_M k_S^{2-}}(Mn^{2+})_i - [S]_b \right\}$$

$$- \frac{(Mn^{2+})_i\, k_{Mn}}{\Omega_M} \left\{ \frac{(S^{2-})_b}{k_S} + \frac{[S]_b}{k_S^{2-}} \right\} = 0 \qquad \text{(A.3.30)}$$

Equation A.3.30 still contains two interfacial concentrations and thus one of them must be eliminated.

At steady state

$$\frac{\dot{n}_{Mn^{2+}}}{A} = \frac{\dot{n}_S}{A}$$

Therefore $k_{Mn^{2+}}[(Mn^{2+})_i - (Mn^{2+})_b] = k_S([S]_b - [S]_i)$

Solving for $(Mn^{2+})_i$

$$(Mn^{2+})_i = \frac{k_S}{k_{Mn^{2+}}} ([S]_b - [S]_i) + (Mn^{2+})_b \qquad (A.3.31)$$

On substituting A.3.31 into A.3.30 and simplifying by collecting terms in $[S]_i$ and dividing by $\{ 1 - \frac{k_{Mn}\, k_S}{\Omega_M k_S{}^{2-}\, k_{Mn^{2+}}} \}$ we obtain a quadratic equation in $[S]_i$ of the form

$$\alpha[S]_i^2 + \beta[S]_i + \gamma = 0$$

where

$$\alpha = 1$$

$$\beta = \frac{\Omega_M k_S{}^{2-} k_{Mn^{2+}} (k_{Mn}[Mn]_b - k_S[S]_b) + k_{Mn} k_S (2k_S[S]_b + k_{Mn^{2+}}(Mn^{2+})_b + k_S{}^{2-}(S^{2-})_b)}{k_S\, (\Omega_M k_S{}^{2-} k_{Mn^{2+}} - k_{Mn} k_S)}$$

$$\gamma = \frac{k_{Mn}[k_S[S]_b + k_{Mn^{2+}}(Mn^{2+})_b][k_S[S]_b + k_S{}^{2-}(S^{2-})_b]}{k_S(\Omega_M k_S{}^{2-} k_{Mn^{2+}} - k_{Mn} k_S)}$$

Subsequently

$$[S]_i = \frac{\beta \pm (\beta^2 - 4\gamma)^{1/2}}{2} \qquad (A.3.32)$$

Substituting (A.3.32) back into (A.3.24) and employing (A.3.28(a)) we obtain the differential equation for mass transfer of sulphur from metal to slag when reacting with Mn in the metal

$$\frac{d(S^{2-})}{dt} = \frac{A}{V_S} k_{S^{2-}} \{ [S]_b - [\frac{-\beta \pm (\beta^2 - 4\gamma)^{1/2}}{2}] \} \qquad (A.3.33)$$

This relation is used in Chapter 5 in the modelling of slag and ingot sulphur profiles for the AC ESR melting of C1117 in CaF_2 - 20%CaO slags.

A.III.3 Derivation of Expressions for $(Mn^{2+})_i$, $(Fe^{2+})_i$

This section is a continuation of Section II.2 and is concerned with the formulation of expressions for the interfacial concentrations of the slag species (Fe^{2+}), (Mn^{2+}). The method is entirely analogous to that used in II.2 and begins with the flux equations (2.2)-(2.4), the interfacial equilibrium of (2.5) and the steady state assumption (2.6).

Combining (2.4) with (2.5) and eliminating the interfacial concentration $(Fe^{2+})_i$ we obtain

$$-\frac{\dot{n}_{Fe^{2+}}}{A} \left(\frac{[Mn]_i}{k_{Fe^{2+}}(Fe^{2+})_b} \right) = [Mn]_i - \frac{(Mn^{2+})_i}{\Omega(Fe^{2+})_b}$$

From (2.2), we have

$$\frac{\dot{n}_{Mn}}{A} \left(\frac{1}{k_{Mn}}\right) = [Mn]_b - [Mn]_i$$

Upon adding and invoking the steady state assumption

$$\frac{\dot{n}}{A} = \frac{[Mn]_b - \frac{(Mn^{2+})_i}{\Omega(Fe^{2+})_b}}{\frac{[Mn]_i}{k_{Fe^{2+}}(Fe^{2+})_b} + \frac{1}{k_{Mn}}} \qquad (A.3.34)$$

Setting (2.2) = (2.3) and solving for $[Mn]_i$

$$[Mn]_i = [Mn]_b - \frac{k_{Mn^{2+}}}{k_{Mn}} \{ (Mn^{2+})_i - (Mn^{2+})_b \} \qquad (A.3.35)$$

Setting, now, (A.3.34) = (2.3) and substituting (A.3.35) for $[Mn]_i$, we obtain the following expression in $(Mn^{2+})_i$

$$[Mn]_b - \frac{(Mn^{2+})_i}{\Omega(Fe^{2+})_b} = \{ k_{Mn^{2+}}((Mn^{2+})_i - (Mn^{2+})_b) \} \times$$

$$\{ \frac{1}{k_{Mn}} + \frac{[Mn]_b}{k_{Fe^{2+}}(Fe^{2+})_b} - \frac{k_{Mn^{2+}}}{k_{Fe^{2+}}k_{Mn}(Fe^{2+})_b}((Mn^{2+})_i - (Mn^{2+})_b)\}$$

This expression is readily reduced to the quadratic of (A.3.36)

$$(Mn^{2+})_i^2 - (Mn^{2+})_i \{ \frac{k_{Fe^{2+}}\, k_{Mn}}{\Omega(k_{Mn^{2+}})^2} + \frac{[Mn]_b\, k_{Mn}}{k_{Mn^{2+}}}$$

$$+ \frac{k_{Fe^{2+}}(Fe^{2+})_b}{k_{Mn^{2+}}} + 2(Mn^{2+})_b \} + (Mn^{2+})_b^2$$

(continued overleaf)

$$+ \frac{k_{Mn}\ k_{Fe^{2+}}[Mn]_b(Fe^{2+})_b}{(k_{Mn^{2+}})^2} + \frac{(Mn^{2+})_b\ k_{Fe^{2+}}(Fe^{2+})_b}{k_{Mn^{2+}}}$$

$$+ \frac{k_{Mn}[Mn]_b(Mn^{2+})_b}{k_{Mn^{2+}}} = 0 \qquad \text{(A.3.36)}$$

It is easily shown that (A.3.36) is the correct expression for $(Mn^{2+})_i$ under the conditions where Ω is large and $[Mn]_b$ is small. (A.3.36) becomes

$$(Mn^{2+})_i^2 - (Mn^{2+})_i \{2(Mn^{2+})_b + \frac{k_{Fe^{2+}}(Fe^{2+})_b}{k_{Mn^{2+}}}\} + (Mn^{2+})_b^2$$

$$+ \frac{(Mn^{2+})_b k_{Fe^{2+}}(Fe^{2+})_b}{k_{Mn^{2+}}} = 0$$

It is readily shown that under the conditions stated (large Ω and $[Mn]_b << (Mn^{2+})_b$) that $(Mn^{2+})_i = (Mn^{2+})_b$. The expression for (Fe^{2+}) is obtained likewise. From a combination of (2.2) and (2.4) we find that

$$\frac{\dot{n}_{Mn}}{A}\left(\frac{\Omega(Fe^{2+})_i}{k_{Mn}}\right) = \Omega(Fe^{2+})_i[Mn]_b - (Mn^{2+})_i$$

from (2.3)

$$\frac{\dot{n}_{Mn^{2+}}}{A}\left(\frac{1}{k_{Mn^{2+}}}\right) = (Mn^{2+})_i - (Mn^{2+})_b$$

Upon adding these two expressions

$$\frac{\dot{n}}{A} = \frac{\Omega(Fe^{2+})_i[Mn]_b - (Mn^{2+})_b}{\frac{\Omega(Fe^{2+})_i}{k_{Mn}} + \frac{1}{k_{Mn^{2+}}}} \qquad (A.3.37)$$

Setting (A.3.37) equal to (2.4) we obtain

$$\Omega(Fe^{2+})_i[Mn]_b-(Mn^{2+})_b = k_{Fe^{2+}}((Fe^{2+})_b-(Fe^{2+})_i)\left(\frac{\Omega(Fe^{2+})}{k_{Mn}} + \frac{1}{k_{Mn^{2+}}}\right)$$

This equation reduces to the quadratic (A.3.38):

$$(Fe^{2+})_i^2 + (Fe^{2+})_i\left\{\frac{k_{Mn}}{k_{Mn^{2+}\Omega}} + \frac{k_{Mn}[Mn]_b}{k_{Fe^{2+}}} - (Fe^{2+})_b\right\}$$

$$- \frac{k_{Mn}}{\Omega}\left\{\frac{(Fe^{2+})_b}{k_{Mn^{2+}}} + \frac{(Mn^{2+})_b}{k_{Fe^{2+}}}\right\} = 0$$

If $(Fe^{2+})_b >> \frac{k_{Mn^{2+}}}{k_{Fe^{2+}}}(Mn^{2+})_b$

it is easily shown that $(Fe^{2+})_i = (Fe^{2+})_b$ and thus that (A.3.38) is correct.

Since the value of all the interfacial concentrations may be found independently, we may use these as a check on the value of Ω that is used in each step of the computer computation. This is the purpose of the subroutine OMT in Appendix IV. By using this routine, we are able to establish the internal consistency of the fitted values of γ_{MnO} vs % MnO which are given in Figure 18.

APPENDIX IV

COMPUTER PROGRAM FOR SOLVING MASS TRANSFER MODEL

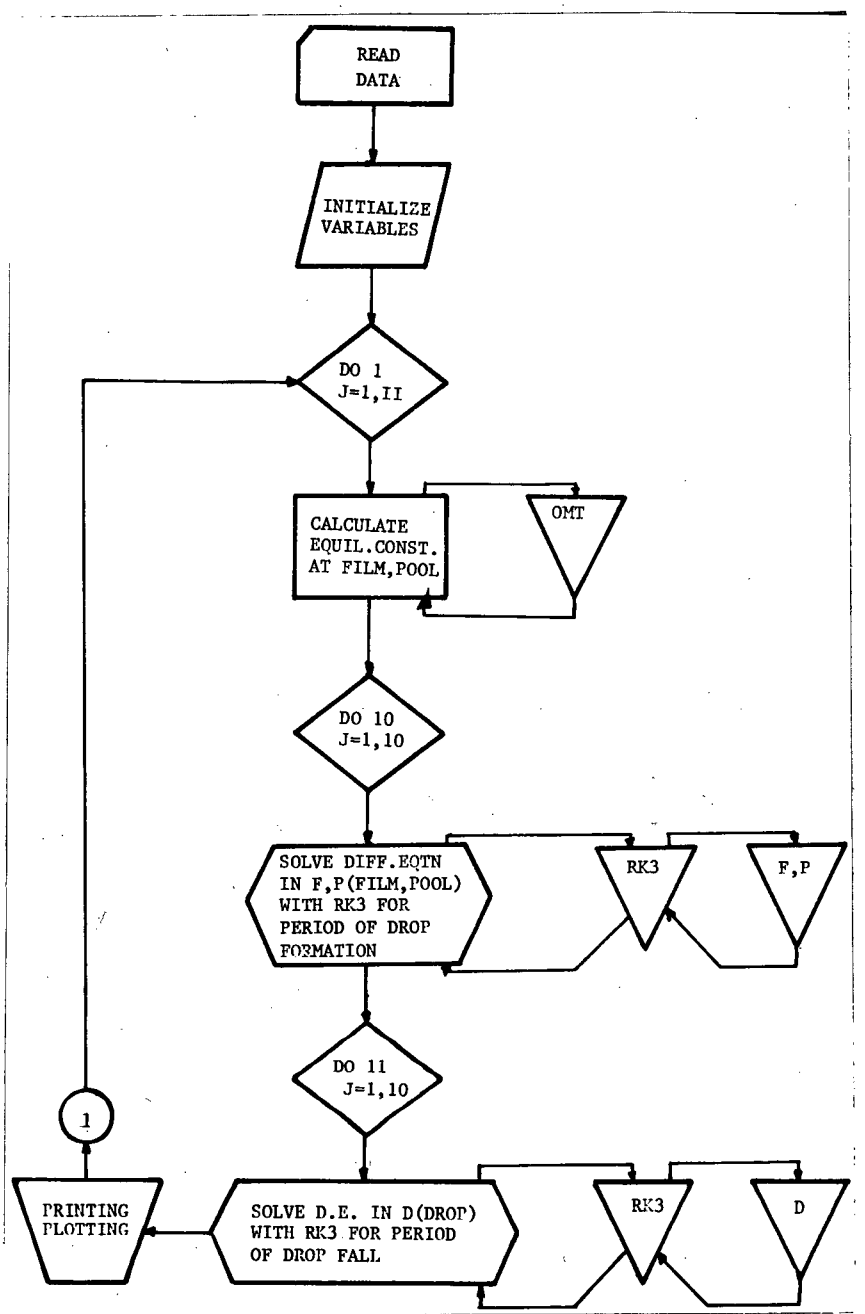

Figure A.IV.1 Algorithm Outlining Computer Program on Following Pages

```
C    COMBINED MASS TRANSFER
       DIMENSION S(1000),WT(1000),WF(1000),WD(1000),WP(1000),WFE(1000)
       COMMON OMEGF,OMEGP,AVF,AVD,AVP
       COMMON KFMN,KDMN,KPMN,KFFE,KDFE,KPFE,KFMI,KDMI,KPMI
       REAL KFMN,KDMN,KPMN,KFFE,KDFE,KPFE,KFMI,KDMI,KPMI,ITER
       EXTERNAL SQRT,F,D,P
       COMMON/DEBUG/FLAG
       LOGICAL FLAG
C
C   EC(A) IS STATEMENT FUNCTION THAT CALCULATES EQUILIBRIUM CONSTANT AS F(TEMP)
C
       EC(A)=EXP(2.303*(6440./A-2.95))
       FLAG=.TRUE.
       CALL PLOTS
C
C   TF = TEMP OF FILM
C   TP = TEMP OF POOL
C   AVF,AVD,AVP ARE AREA/VOLUME RATIOS OF FILM,DROP,POOL
C   RUN IS RUN NUMBER//ITER  IS # OF ITERATIONS
C   KFMN,KFFE,KFMI ARE MASS TRANSFER COEFF. OF MN(IRON),FE(SLAG),MN(SLAG) AT FILM
C   SIMILARLY KDMN ETC ARE DROP MT COEFF. / KPMN ARE POOL MT COEFF.
C   CM IS INITIAL CONC. OF METAL(WT%) IN ELECTRODE
C   VF,VD,VP ARE VOLUMES OF FILM,DROP,POOL
C   H IS STEP SIZE FOR INTEGRATION AT FILM ,POOL INTERFACES/HD FOR DROP FALL TIME
C   CS INITIAL CONC. MN IN SLAG(WT%)/CFE INITIAL CONC. FE IN SLAG (WT%)
C   VS IS VOLUME OF SLAG/VL IS RATE OF CHANGE OF VS/YP = INIT. CONC. MN IN POOL
C   XMF,XMD,XMP - CHANGE IN SLAG COMP DUE TO SITE F,D,P IN CURRENT ITER
C   TOL LIMIT OF ACC OF GAMMA MNO
C   XTF,XTD,XTP - CUMULATIVE CHANGE IN SLAG COMP DUE TO SITE F,D,P
C
       READ (7,101) TF,TP,AVF,AVD,AVP,GAMF,GAMP,GMXF,GMXP,RUN,ITER
       READ (7,200) KFMN,KFFE,KFMI,KDMN,KDFE,KDMI,KPMN,KPFE
       READ (7,200) KPMI,CM,VF,VD,VP,H,CS,CFE,HD,VL,VS,YP,GFEO
       CALL AXIS (0.,0.,'TIME IN SECONDS',-15,14.,0.,0.,100.)
       CALL AXIS (0.,0.,'WEIGHT PERCENT',14,10.,90.,0.,.1)
       CALL SYMBOL (1.,9.6,.28,'THEORETICAL MODEL ',0.,17)
       CALL NUMBER (5.5,9.6,.28,RUN,0.,0)
       YL=CM*1.31E-3
       XM=CS*4.74E-4
       XMI=XM
       XMF=0.
       XMD=0.
       XMP=0.
       XTF=0.
       XTD=0.
       XTP=0.
       FE=CFE*4.65E-4
       FF=FE
       TIME=0.
       MM=20
       II=ITER/(H*10.)
       S(1)=TIME
       WT(1)=XM
       WF(1)=XMF
       WD(1)=XMD
       WP(1)=XMP
       WFE(1)=FE*2.15E+4
       L=2
       M=10
C   GF = CURRENT VALUE OF GAMMA 0 FILM
C   GP = CURRENT VALUE OF GAMMA 0 POOL
C   USE SAME GAMMA 0 FOR DROP AS FOR POOL
       YP=YP*1.31E-3
C
       T=TF+273.
       CALL OMT(KFMN,KFFE,GAMF,YL,XM,FE,T,TOL)
       GF=GAMF
       OMEGF=764.77*GFEO*EC(T)/GF
       T=TP+273.
       CALL OMT(KPMN,KPFE,GAMP,YP,XM,FE,T,TOL)
       GP=GAMP
       OMEGP=764.77*GFEO*EC(T)/GP
       WRITE (6,40) RUN,OMEGP,TF,GF,OMEGP,TP,GP,GMXF,GMXP,GFEO
       WRITE (6,300) KFMN,KFFE,KFMI,AVF,KDMN,KDFE,KDMI,AVD,KPMN,KPFE,KPMI
      1,AVP
       WRITE (6,333) CM,YP,CS,VF,VD,VP,VS,VL,H,HD
       WRITE (6,3)
       WRITE (6,2) XM,TIME,XMF,XMD,XMP,YF,YD,YP
```

```
C  BEGIN ITERATIONS
C
      DO 1 I=1,II
      T=TF+273.
      GF=GAMF
      CALL OMT(KFMN,KFFE,GAMF,YL,XM,FE,T,TOL)
      OMEGF=764.77*GFEO*EC(T)/GF
      T=TP+273.
      GP=GAMP
      CALL OMT(KPMN,KPFE,GAMP,YP,XM,FE,T,TOL)
      OMEGP=764.77*GFEO*EC(T)/GP
      YF=YL
C
C  FUNCTIONS F,P,D, CONTAIN DIFFERENTIAL EQUATIONS TO BE INTEGRATED BY SOLVMN
C  SOLVMN USES THIRD ORDER RUNGE KUTTA
C
C  DROP FORMATION
      DO 10 J=1,10
      CALL RK3 (F,H,YF,XM,FE,XMF,VF,XTF,VS,TIME)
      FE=FF
      CALL RK3 (P,H,YP,XM,FE,XMP,VP,XTP,VS,TIME)
C  ADD DROP TO POOL
      IF(J.EQ.2.AND.I.NE.1) YP=YP+(YD-YP)*VD/VP
      VS=VS-VL*H
10    FF=FE
C     DROP FALL
      YD=YF
      DO 11 J=1,10
11    CALL RK3 (D,HD,YD,XM,FE,XMD,VD,XTD,VS,TIME)
      FE=FF
      TIME=TIME+10.*H
      IF(I.GT.1.AND.I.LT.II) GO TO 6
      WRITE (6,2) XM,TIME,XMF,XMD,XMP,YF,YD,YP
      GO TO 12
6     IF(I.LT.M) GO TO 1
      WRITE (6,2) XM,TIME,XMF,XMD,XMP,YF,YD,YP
      M=M+MM
12    S(L)=TIME/100.
      WT(L)=XM*2.11E+4
      WF(L)=XTF*2.11E+4
      WD(L)=XTD*2.11E+4
      WP(L)=XTP*2.11E+4
      WFE(L)=FE*2.15E+4
      L=L+1
1     CONTINUE
      L=L-1
      LM=L
      CALL LINE (S,WT,L,1)
      CALL LINE (S,WFE,L,1)
      CALL LINE (S,WF,L,1)
      CALL LINE (S,WD,L,1)
      CALL LINE (S,WP,L,1)
      CALL SYMBOL (S(LM),WFE(LM),.14,'IRON',0.,4 )
      CALL SYMBOL (S(LM),WT (LM),.14,'MN TOTAL',0.,8)
      CALL SYMBOL (S(LM),WP(LM),.14,'POOL',0.,4)
      CALL SYMBOL (S(LM),WF(LM),.14,'FILM',0.,4)
      CALL SYMBOL (S(LM),WD(LM),.14,'DROP',0.,4)
      CALL PLOTND
2     FORMAT (1X,8(1PE12.5,3X)/)
3     FORMAT (1X,'(MN2+) SLAG',6X,'TIME',27X,'SLAG',41X,'METAL'/22X,
     12(11X,'FILM',11X,'DROP',11X,'POOL')/)
40    FORMAT (1H1,1X,'MODEL # ',F5.0//10X,'MOLAR EQUIL CONSTANT(FILM) ='
     1,F5.0,     2X,'GAMMA   MNO(',F5.0,') =',F6.2/10X,'MOLAR EQUIL CONS
     2TANT(POOL,DROP,) =',F5.0,2X,'GAMMA   MNO(',F5.0,') =',F6.2//,
     31X,'GAMMA- -F FNL =',F5.1,/1X,,'GAMMA- -P FNL =',F5.1//,1X,'GAMMA
     4FEO =',F5.1//)
101   FORMAT (2F5.0,5F10.3,4F5.0)
200   FORMAT (8F10.6)
300   FORMAT (1X,'FILM TRANSFER DATA'/1X,'KMN =',F10.6,'; KFE2+ =',F10.6
     1,'; KMN2+ =',F10.6,'; AREA/VOLUME RATIO =',F10.3//
     2        1X,'DROP TRANSFER DATA'/1X,'KMN =',F10.6,'; KFE2+ =',F10.6
     3,'; KMN2+ =',F10.6,'; AREA/VOLUME RATIO =',F10.3//
     4        1X,'POOL TRANSFER DATA'/1X,'KMN =',F10.6,'; KFE2+ =',F10.6
     5,'; KMN2+ =',F10.6,'; AREA/VOLUME RATIO =',F10.3)
333   FORMAT (////1X,'INITIAL CONDITIONS'///1X,'WT % MN IN ELECTRODE =',
     1F10.6/1X,'WT % MN IN POOL =',F10.6/1X,'WT % MN IN SLAG =',F10.6///
     2/1X,'FILM VOLUME =',F10.6/1X,'DROP VOLUME =',F10.6/1X,'POOL VOLUME
     3 =',F10.6//// 1X,'INITIAL SLAG VOLUME =',F10.6/1X,'RATE OF SLAG LO
     4SS =',F10.6///1X,'STEP SIZE(SECS) FOR POOL,FILM INTEGRATIONS =',F1
     50.6/1X,'STEP SIZE(SECS) FOR DROP INTEGRATION =',F10.6/1H1)
      STOP
      END
```

```
      SUBROUTINE OMT(XM,XS,G,CM,CMS,CF,T,TOL)
      ROOT(A,B)=(-B+SQRT(B*B-4.*A))/2.
      EC(X)=EXP(2.303*(6440./X-2.95))
      T=T+273.
      CM=CM*1.31E-3
      CMS=CMS*4.74E-4
      GG=G
      CF=CF*4.65E-4
10    G=GG
      EQ=2753.*EC(T)/G
      BF=XM/(EQ*XS)+XM*CMS/XS-CF
      AF=-(XM/EQ)*(CF/XS+CMS/XS)
      FI=ROOT(AF,BF)
      BM=1./EQ+XS*CF/XM-CM
      AM=-(XS/EQ)*(CM/XS+CMS/XM)
      XMI=ROOT(AM,BM)
      BMS=-(XM/EQ+CM*XM/XS+CF+2.*CMS)
      AMS=CMS*CMS+XM*CM*CF/XS+CMS*CF+XM*CM*CMS/XS
      XMSI=ROOT(AMS,BMS)
      GN=XMSI/(XMI*FI)
      GG=(EQ/GN)*G
      IF(ABS(GG-G).GT.TOL) GO TO 10
      RETURN
      END
```

```
      SUBROUTINE RK3 (AUX,H,Y,XM,FE,XMM,V,XTM,VS,TIME)
      XK1=AUX(Y,XM,FE)
      XK2=AUX(Y+H*XK1/2.,XM+H/2.,FE)
      XK3=AUX(Y+2.*H*XK2-H*XK1,XM+H,FE)
      YN=Y+(H/6.)*(XK1+4.*XK2+XK3)
      XMM=(Y-YN)*V/VS
      XTM=XTM+XMM
      XM=XM+XMM
      Y=YN
      RETURN
      END
```

```
      FUNCTION F(Y,XM,FE)
      REAL KFMN,KDMN,KPMN,KFFE,KDFE,KPFE,KFMI,KDMI,KPMI
      COMMON OMEGF,OMEGP,AVF,AVD,AVP
      COMMON KFMN,KDMN,KPMN,KFFE,KDFE,KPFE,KFMI,KDMI,KPMI
      A=KFFE/(KFMI*OMEGF)
      E=KFFE/KFMN
      B=A+E*FE-Y
      C=A*Y+E*XM/OMEGF
      G=-B+SQRT(B*B+4.*C)
      F=-AVF*KFMN*(Y-G/2.)
      RETURN
      END


      FUNCTION D(Y,XM,FE)
      REAL KFMN,KDMN,KPMN,KFFE,KDFE,KPFE,KFMI,KDMI,KPMI
      COMMON OMEGF,OMEGP,AVF,AVD,AVP
      COMMON KFMN,KDMN,KPMN,KFFE,KDFE,KPFE,KFMI,KDMI,KPMI
      A=KDFE/(KDMI*OMEGP)
      E=KDFE/KDMN
      B=A+E*FE-Y
      C=A*Y+E*XM/OMEGP
      G=-B+SQRT(B*B+4.*C)
      D=-AVD*KDMN*(Y-G/2.)
      RETURN
      END


      FUNCTION P(Y,XM,FE)
      REAL KFMN,KDMN,KPMN,KFFE,KDFE,KPFE,KFMI,KDMI,KPMI
      COMMON OMEGF,OMEGP,AVF,AVD,AVP
      COMMON KFMN,KDMN,KPMN,KFFE,KDFE,KPFE,KFMI,KDMI,KPMI
      A=KPFE/(KPMI*OMEGP)
      E=KPFE/KPMN
      B=A+E*FE-Y
      C=A*Y+E*XM/OMEGP
      G=-B+SQRT(B*B+4.*C)
      P=-AVP*KPMN*(Y-G/2.)
      RETURN
      END
```

APPENDIX V

THERMOCHEMICAL AND HEAT TRANSFER CALCULATIONS

A.V.1 Oxidation Potentials of Mn, Si in 1018 Steel Melting in CaF_2-20% CaO Slag

$$\log h_x = \log F_x^x + \sum_1^N e_x^y (wt\%y) + \log (wt\%x)^{32}$$

where h_x is the Henrian activity of species x in solution of iron with other solutes,(y). The major solutes in 1018 are C, S, Si at 0.15, 0.105, 0.04 wt % respectively in addition to manganese at ≃ .57% (the lowest observed value). From Tables in Bodsworth[32]

$$e_{Mn}^{Mn} = 0; \quad e_{Mn}^{C} = -0.009; \quad e_{Mn}^{S} = -0.045; \quad e_{Mn}^{Si} = 0$$

$$e_{Si}^{Si} = 0.32; \quad e_{Si}^{Mn} = 0; \quad e_{Si}^{C} = 0.20; \quad e_{Si}^{S} = 0.057$$

Therefore, $\log h_{Mn} = (0 \times .57) - (.009 \times .15) - .045 \times .04 + 0 \times .04 + \log .57.$

$$= -.0014 - 0.0018 - .2441$$

$$h_{Mn} = .57$$

also $\log h_{Si} = .105 \times .32 + .15 \times 2 + .04 \times .057 + \log .04$

$$h_{Si} = \text{antilog } (\bar{1}.0871) = .122$$

The Raoultian activity, a_x, is given by

$$a_x = h_x \gamma_x^\circ .5585/MW_x$$

$$\gamma_{Si}^\circ = \text{antilog } (1.21 - 6100/T)$$

at 1525°C $\gamma_{Si}^\circ = 6.56\ (10^{-3})$

at 1675°C $\gamma_{Si}^\circ = 1.2\ (10^{-2})$

$$a_{Si,1525} = .122 \times 6.56(10^{-3}) \times .5585/28.09 = 1.59(10^{-5})$$

$$a_{Si,1675} = .122 \times 1.2(10^{-2}) \times .5585/28.09 = 2.9(10^{-5})$$

The standard free energies for the reactions A, B are given by:

(A) $Si(\ell) + O_{2(g)} \overset{\rightarrow}{\leftarrow} (SiO_2)_\ell \quad \Delta F^\circ = -223,800 + 46.08\ T^{82}$ cal mole^{-1}

(B) $2\underline{Mn} + O_{2(g)} \overset{\rightarrow}{\leftarrow} 2(MnO)_S \quad \Delta F^\circ = -195,100 + 51.33\ T^{82}$ cal mole^{-1}

$$\Delta F_{Si}^\circ = RT\ \ell n\ P_{O_2} - RT\ \ell n\ \left(\frac{a_{SiO_2}}{a_{Si}}\right)$$

$$\Delta F_{Mn}^\circ = RT\ \ell n\ P_{O_2} - RT\ \ell n\ \left(\frac{a_{MnO}}{h_{Mn}}\right)$$

$a_{MnO} = 5(10^{-3})$ - typical value from experimental results (Chapter 4 and (37))

$a_{SiO_2} = 5(10^{-4})$ - minimum expected value in CaF_2-CaO slag[83] at 1550°C(1823°K).

Solving for RT ℓn P_{O_2} for Mn/MnO, we have

$$RT\ \ell n\ P_{O_2} = -195100 + 51.557 + 2\ RT\ \ell n\ (\frac{5(10^{-3})}{.57}$$

Solving for P_{O_2} at 1525°C and 1675°C.

$$(P_{O_2})_{Mn/MnO,1525°C} = 2.7(10^{-17})\ \text{atm}$$

$$(P_{O_2})_{Mn/MnO,1675°C} = 1.8(10^{-15})\ \text{atm}$$

for Si/SiO_2, we have

$$RT\ \ell n\ P_{O_2} = -223800 + 46.08\ T + RT\ \ell n\ (\frac{5(10^{-4})}{a_{Si,T}})$$

Therefore,

$$(P_{O_2})_{Si/SiO_2,1525°C} = 2.3(10^{-16})\ \text{atm}$$

$$(P_{O_2})_{Si/SiO_2,1675°C} = 1.6(10^{-14})\ \text{atm.}$$

The activity effects are clearly shown in Figure A.V.1. The Si/SiO_2 line does not move due to low activities of Si and SiO_2. However, the low level and thus, low activity, of MnO in the slag produces a clockwise rotation of the Mn/MnO line. This shows that at both 1525°C and 1675°C that Mn will oxidize preferentially to Si.

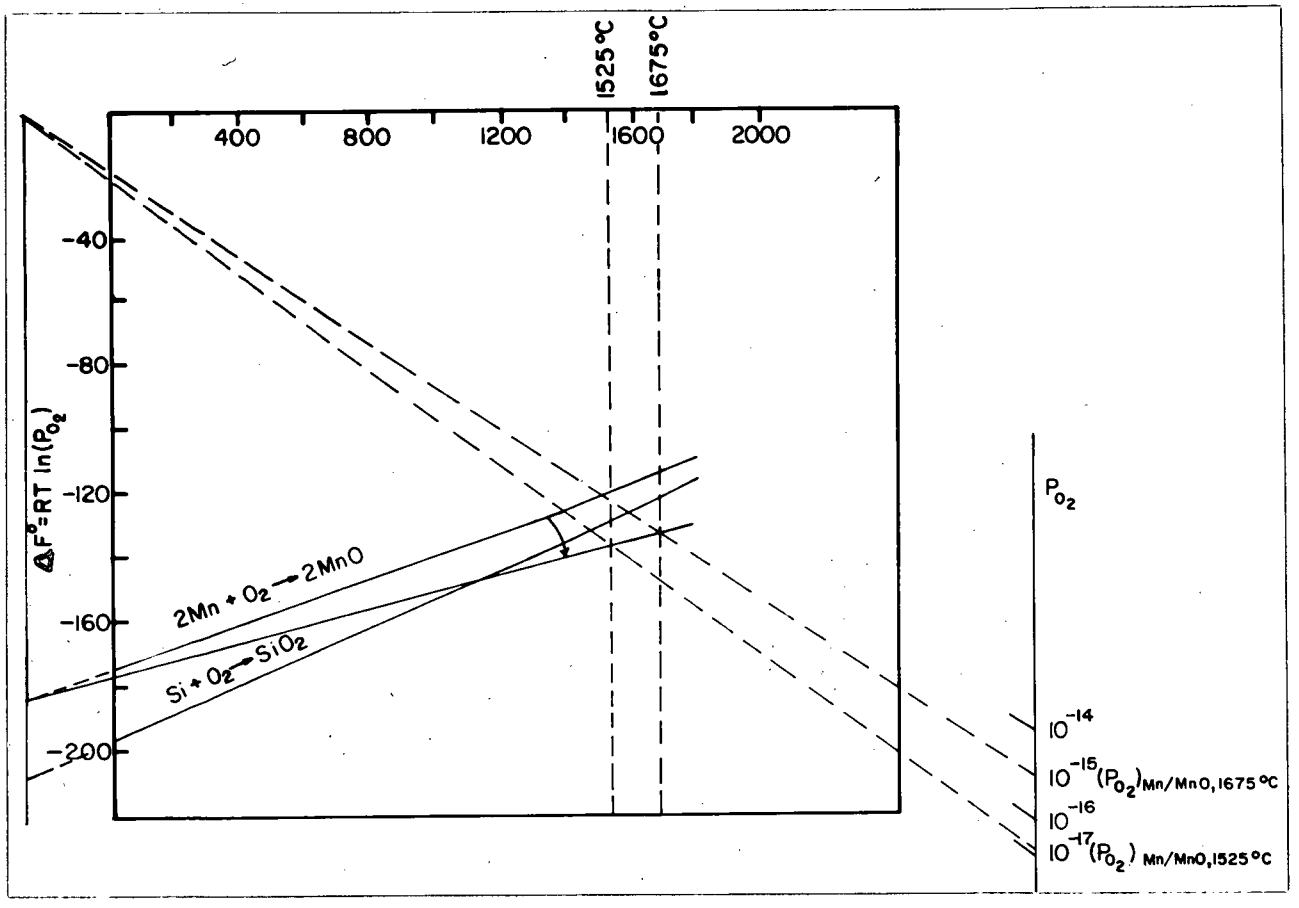

Figure A.V.1. Free Energy - Temperature Plot Showing Rotation of Mn/MnO Line

A.V.2. Calculation of Temperature of Electrode Film Using Derived Heat Transfer Coefficient at Slag/Film Interface

At steady state, a simple heat balance at the electrode tip is made up of three parts.[24]

Rate of heat in at slag/metal boundary = Rate of heat loss by conduction up the electrode + Rate of heat loss by melting.

The net heat flow into the electrode tip, $\dot{q}$, is given by

$$A_F\, h_S\, (T_S - T_M) = Q \times \dot{W}_M + A_{XS}\, k\left(\frac{dT}{dz}\right)_{z=0} \qquad \text{(A.V.2.1)}$$

or

$$\dot{q}\left(\frac{cal}{sec}\right) = A_F\, h_S\, (T_S - T_M) - Q \times \dot{W}_M - A_{XS}\, k\left(\frac{dT}{dz}\right)_{z=0}$$

$z = 0$ = electrode tip melting surface

$$h_S = .18 \text{ cal cm}^{-2} \text{ sec}^{-1} {}^\circ\text{K}^{-1} \quad \text{(V.1.1)}$$

T_S = slag temp = 1675°C

T_M = melting point ≃ 1520°C

Q = 65.65 cal gm^{-1}

$\dot{W}_M$ = 2.63 gm sec^{-1}

k = 0.074 cal cm^{-1} sec^{-1} °K^{-1}

A_F = 16.2

$A_{XS} = \pi(1.91)^2$

$\left(\frac{dT}{dz}\right)_{z=0}$ = 260°C cm^{-1} [24]

= temp grad at electrode tip in electrode

at steady state $\dot{q} = 0$, and solving for T_M .

$$T_M = T_S - \frac{L \times \dot{W}_M}{A_F\, h_S} - \frac{A_{XS}}{A_F h_S}\, k \left(\frac{dT}{dz}\right)_{z=0} \qquad \text{(A.V.2.2)}$$

Substituting in the above values.

$$T_M = 1675 - \frac{65.65 \times 2.6}{.18 \times 16.2} - \frac{\pi(1.91)^2 \times .074 \times 260}{.18 \times 16.2}$$

$$= 1540°C\ .$$

We have assumed only a small degree of superheating of the electrode film in our analysis and the value obtained using the derived heat transfer coefficient from V.1.1 seems to confirm this. It is possible that T_{Siag} may be lower that 1675°C since the slag in contact with the electrode tip is coming from the surface of the slag bath (see Figure 12). Thus the value of 1525°C used for the metal film temp in calculating the equilibrium constant in the mass transfer model is entirely reasonable. This conclusion has also been shown to be valid for the unsteady state case where metal is flowing on the electrode tip and the electrode and ingot pool surface are moving.[38]

A.V.3 Calculation of Temperature of Drop after Fall through Slag

Heat input to drop is given by

$$\dot{q}\ \left(\frac{cal}{sec}\right) = A\, h_S\, (T_S - T_M)$$

$$\frac{dq}{dt}\frac{1}{C_p} \times W = \frac{Ah_S\ W\ (T_S-T_M)}{C_p} = dT_M \qquad \text{(A.V.3.1)}$$

$A = 8.4\ cm^2$ (II.4)

$W \simeq 2.5\ gm$ (Appendix I.6)

$C_p = .2\ cal\ gm^{-1}\ {}^\circ K^{-1}$

$h_S = .23$ (Table XIV)

$T_S = 1675°C,\ T_M = 1520°C$

Rearranging (A.V.3.1) and integrating we have

$$\int_{T_M1}^{T_M2} \frac{dT_M}{(T_S-T_M)} = \int_0^t \frac{A\ h_S\ W}{C_p}\ dt$$

$$\ell n\ \left(\frac{T_S-T_M2}{T_S-T_M1}\right) = -\frac{A\ h_S\ W}{C_p}\ t$$

or $$T_M2 = T_S - (T_S-T_M2)\ \exp\ \left(-\frac{Ah_S\ W}{C_p}\ t\right) \qquad \text{(A.V.3.2)}$$

If the drop fall time is .12 sec (Table 1)

then $$T_M2 = 1675 - (155)\ \exp\ \left(-\frac{8.4 \times .23 \times 2.5 \times .12}{.2}\right)$$

$$= 1675 - (155 \times .055)$$

$$= 1666°C$$

Therefore, the drop is very nearly thermally equilibrated with the slag by the time it reaches the ingot pool surface.